Pulsed Laser Deposition of 2D Materials and Complex Perovskites

by

Dhanvini Gudi

A thesis submitted in partial fulfillment of the requirements for the degree of

Master of Science

in

Microsystems and Nanodevices

Electrical and Computer Engineering

University of Alberta

Abstract

Pulsed laser deposition is a physical vapor deposition technique used for the growth of single crystal epitaxial thin films on a variety of substrates. Due to the high energy of the ablated particles from the target, the plasma plume consists of atoms, molecules, ions and electrons, PLD allows for high efficiency in the deposition of materials with complex stoichiometry.

Two very different materials are grown using PLD in this study, namely, a 2D material called Molybdenum sulphide (MoS_2) for electronic device applications and a novel perovskite material called for $La_{0.3}M_{0.7}Fe_{0.7}Cr_{0.3}O_{3-\delta}$ (M = Ca, Sr) (LCFCr and LSFCr) for solid oxide fuel cell applications. This thesis consists of a study of the effect of the variation of PLD parameters on the film quality, and thus, an optimization of these parameters to obtain thin films with desirable properties.

The thin films of MoS_2 grown in different conditions have been analyzed using material and electronic characterization techniques to study the film properties. Single crystal epitaxial growth was obtained with a crystal phase corresponding to (002) orientation of MoS_2. A high uniformity with a film RMS roughness of around 0.17 nm was obtained for 5 monolayers of MoS_2. XPS analysis was used to observe a presence of small amounts of MoO_3 and semimetallic 1T-MoS_2 in the semiconducting 2H-MoS_2 thin films. Transmission and absorption studies over different thicknesses of the deposited films showed the presence of B and C excitonic transitions in the film.

Hall measurement has also been performed for the thin films over different thicknesses to study electrical properties. With Van der Pauw measurements over an area of around 25 mm^2, an increasing trend was observed from 5 to 13 monolayers of MoS_2 and a decreasing trend from 13 to 56 monolayers of MoS_2, with the highest electron mobility of 76.92 cm^2/Vs observed in our studies for 13 monolayers of MoS_2. This trend matched the studies of FET mobility measured over devices with different thicknesses observed in literature. These promising studies suggest potentially higher mobilities on PLD grown MoS_2 thin film based FET devices. These studies serve as a starting point for several future applications of PLD deposited MoS_2 thin films in scaled electronic devices and sensors and flexible electronic devices and sensors.

Thin films of LMFCr (LCFCr and LSFCr) were deposited under different conditions and analyzed using using material characterization techniques to study the film properties. Under optimized growth conditions, epitaxial single crystal thin films of LCFCr with a (002) crystal phase was observed. A high film uniformity with the lowest RMS roughness of 0.15 nm obtained for LCFCr. XPS analysis helped study and confirm the elemental states present in the thin films. These optimized thin films can be used for solid oxide fuel cell applications in the future.

Acknowledgments

I would like to acknowledge and thank my supervisor Dr. Manisha Gupta for all the skills and knowledge I have gained in these last two years. These last two years have helped me grow both personally and professionally, and made me a better researcher. I would like to thank her for teaching me how to approach and solve problems, and work on seeing the bigger picture whenever I got stuck.

I would like to thank Prof. Ying Tsui for access to his lab and the pulsed laser deposition tool that was used for a large portion of this thesis work. I would also like to thank Prof. Sandipan Pramanik and his student Seyedamin Firouzeh for access to their lab and their tool for Hall measurements. I would like to thank NanoFAB staff for training me on several fabrication and characterization tools and providing me with valuable assistance to solve experimental challenges. I would also like to thank CMC Microsystems for their MNT Award, which covered a large portion of my fabrication costs, and provided me with access to the Synopsys TCAD tool for my simulation work. I would also like to thank FES, University of Alberta, and Prof. Viola Birss and Dr. Haris Ansari, University of Calgary for the collaborative work on PLD growth of LCFCr for solid oxide fuel cell applications.

I would like to thank all of my lab members, Jiaxin Fan, Payel Sen, Junsen Gao, Dipanjan Nandi, Michael Facchini-Rakovich, Seongdae Kang and Andres Forero Pico for their support and valuable discussions that helped me with my work. I would like to thank my friends (especially Rohit, Anjana, Deepa and Shruthi) and my family for their support.

Contents

List of Tables

List of Figures

Chapter 1

Introduction

1.1 Materials Research in Electronic Applications

Research in material science and engineering is a very important factor that has contributed to the accelerated growth of technical innovations in electronics. This is due to the incredible diversity of applications that has risen from a fundamental understanding of novel materials, their properties and studies to manipulate them for these different applications. This can be seen in current research in areas ranging from electronic devices [1], sensors [2], interfaces [3], energy [4], mechanical systems [5], chemicals [6], and construction [7], over the last 50 years.

Materials research involves an amalgamation of chemistry, physics, engineering and minerology to understand and apply the behavior of different materials and their observed properties in order to design and create new materials and applications. Material science and engineering, therefore, has emerged as a truly interdisciplinary field which brings together a variety of diverse disciplines to create novel solutions to engineering problems.

Since the formalization of the field material science and engineering in the 1950s, this area has emerged at the forefront of solutions to some of the most pressing scientific problems faced by humans [8]. Over just the last 20 years, there has been a highly rapid pace of inventions such as smartphones and smart-devices, flexible

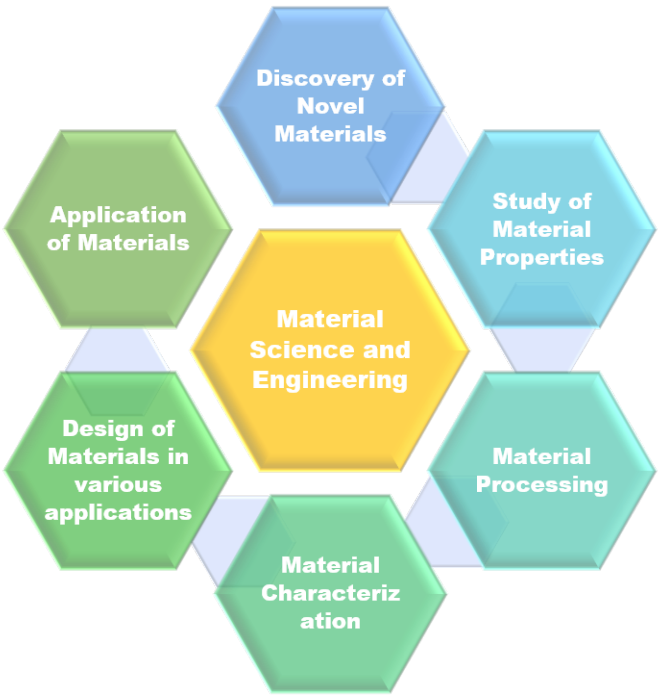

Figure 1.1: Stages of research in material science and engineering

sensors, integrated platforms and novel energy and transportation solutions that have enabled the world to change at a scale never seen before. In the micro and nanoscale research in particular, it has become imperative to study the fundamental properties of the materials which form the extensive range of devices and sensors of today. Thin film research, therefore, ends up forming the backbone of the study, to help apply this knowledge of these materials for these applications [9]. With more of the application of material research in micro and nanotechnological areas, material science and engineering is looking to become one of the most important disciplines to fuel the future of technology [10].

1.2 Thin films and their applications

Thin films are defined as a layer of material with thicknesses ranging from sub nanometer (monolayer) to a few micrometers (multi-layer). The process of synthesis of these thin films is referred to as thin film deposition, which is a crucial step in any processing involving thin films [11].

Some of the earliest examples of thin film processing would be metal coatings to form protective layers around bodies [12], decorative coating of gold and aluminum on paintings and sculptures and metallic thin film coatings of mirrors to form the reflective surface [13].

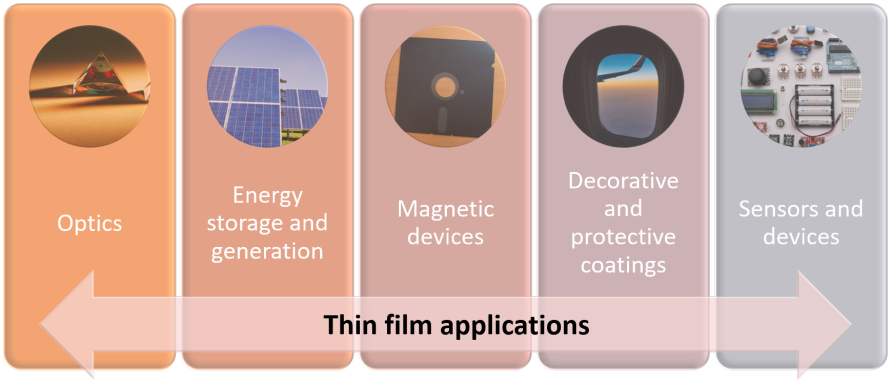

Figure 1.2: A representation of some of the various applications of thin films

Thin film research over the years has developed from simplistic applications such as decorative coatings and protective layering to more complex systems such as electrical and electronic sensors and devices, biomedical applications, energy storage, and generation and metallurgical applications [14]. Over the last year, some of the latest innovations such as smart material coatings for glass surfaces that change their transparency with temperature and light, highly durable and strong biodegradable materials as alternatives to plastics, and meta-materials capable of changing surface properties and optical cloaking at different wavelength ranges have shown promising results for a wide range of future applications [15].

A deeper understanding of thin film deposition techniques, material processing and characterization techniques and research into the latest innovations would be useful to pave the way for several more such innovations [16].Fundamental properties of thin films such as crystallinity, morphology and optical and electronic properties are crucial for this purpose. Some common deposition techniques have been listed in Figure 1.3.

This thesis focuses on two main applications of thin films, namely, electronic devices and electrode materials for solid fuel cells, with a focus on one main kind of

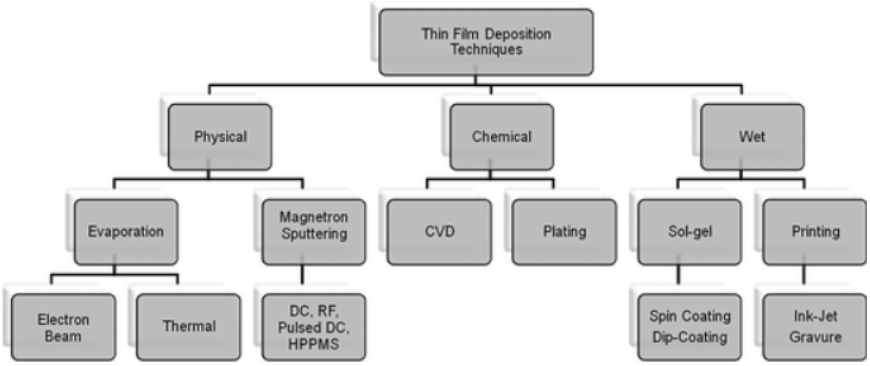

Figure 1.3: Common techniques of thin film deposition [17]

deposition technique used for this study, which is pulsed laser deposition (PLD). The material and electrical properties of novel materials that have been grown using PLD have been studied, and the potential for their usage in different applications has been explored.

1.2.1 Electronic devices

The contribution of thin film technology in the area of electronic and optoelectronic devices and sensors has been immense. Some of the applications include simple devices such as capacitive and resistive elements and solid state devices such as transistors, magnetic devices, integrated sensors, circuit elements and opto-electronic, magnetic and bio-electronic devices and sensors [18].

One class of materials that has caught attention in the recent years is 2D materials. The structure of these materials consists of conducting sheets of atoms or molecules which are stacked, layer by layer and held together by weak Van der Waal's forces. As 2D materials, there is also a reduced dimensionality that leads to enhanced quantum effects, and therefore, the possibility of the tuning of electronic, magnetic and optical properties with the number of layers. Due to the structure of these materials, there has also been great excitement in the potential for 2D material based transistors to be scaled down beyond the sizes achieved by silicon based devices, and achieve sub 5 nm size electronic devices.

Since the discovery of monolayer graphene, its unique properties such as pos-

session of the highest known thermal and electrical conductivity, high mechanical strength and change in electronic, optical and magnetic properties due to a reduced dimensionality of the film has excited the world. The discovery of 2D transition metal dichalcogenides (TMDCs) in particular, has lead to a further interest in this class. Graphene possesses a zero band gap, and so 2D TMDCs that possess finite bandgaps along with a layer dependent change in electrical, optical and magnetic properties, show potential in semiconductor device applications [19; 20; 21]. One such 2D TMDC material, MoS_2 is explored in this thesis. Due to the structure of MoS_2, combined with its unique properties that change with the number of layers, it has seen applications in flexible electronic sensors, One of the examples of a MoS_2 based device application is shown in Figure 1.4. A background into MoS_2 and its properties is presented in Chapter 2.

1.2.2 Electrode materials in electrolytic cells

Thin films also form a major component in energy storage and generation elements such as batteries and cells [22]. In the recent years, due to the focus on sustainable energy, there has been increasing interest in different methods for carbon capture and utilization. One of the most popular devices for this has been the solid oxide fuel cell, which can harness fuel byproducts and convert them to usable electrical energy. Several innovations to improve the performance of these cells has been made possible with different material being developed and used as catalytic and electrode material layers.

Some of the common techniques of deposition of these materials include sputtering for the contact and insulating material layers, and wet processing techniques such as spin coating or other sol-gel methods for the electrode and catalyst material layers. In this thesis, the growth of $La_{0.3}M_{0.7}Cr_{0.3}Fe_{0.7}O_{3-\delta}$ (LMFCr) where M = Ca or Sr, is explored for applications as a catalytic electrode in solid oxide fuel cells. A more detailed insight into the background and applications of these materials is provided in Chapter 2.

1.3 Overview of the thesis

This thsis is divided into 6 chapters.

Chapter 1 explores the motivation behind the study, and an overview of this thesis.

Chapter 2 presents a literature review and background of pulsed laser deposition, the materials being explored, namely MoS_2 and LMFCr and the different material and electronic characterization techniques used for analysis.

Chapter 3 talks about the growth and optimization of MoS_2 thin films using pulsed laser deposition and its material and electrical characterization. In the studies, 90% of the growths were performed by the author, and 10% of the growths were performed by Dipanjan Nandi from our research group. Material characterization using XRD, AFM, profilometer and 4 point probe were performed by the author. The TEM and HIM imaging have been performed by Payel Sen from our research group. The Raman spectroscopy have been performed by Dipanjan Nandi. The XPS measurements have been performed at the NanoFAB, University of Alberta by Dr. Shihong Xu and analyzed by the author.

Chapter 4 presents the electrical characterization of MoS_2 thin films by Hall measurements to calculate the mobility. The measurements were performed by me in Dr. Sandipan Pramanik's lab with the assistance of Seyedamin Firouzeh.

Chapter 5 presents a theoretical simulation based study performed by me on MoS_2 based Schottky junctions carried using Synopsys TCAD softwares respectively. A preliminary study on p-Si - MoS_2 based diode fabrication and electrical characterization using Keithley 4200 probe station performed by the author is also presented.

Chapter 6 talks about the growth and optimization of LMFCr (LCFCr and LSFCr) and its material characterization. 90% of the growths were performed by the author, and 10% of the growths were performed by Dipanjan Nandi. Material characterization using XRD (on NanoFAB Bruker D8 and Rigaku Ultima IV tools) and AFM were performed by the author. Additional XRD studies on NRC Discover D8 2D tool were performed in the National Institute for Nanotechnology (NINT)

with the assistance of Steve Launspach. The TEM studies were performed by Dr. Hui Yuan and Prof. Gianluigi from the Canadian Centre for Electron Microscopy (CCEM), McMaster University. The XPS measurements have been performed at the NanoFAB, University of Alberta by Dr. Shihong Xu and analyzed by the author.

Chapter 7 presents the summary and a few concluding statements from the study performed, and explores the directions for future work to carry forward this work.

Chapter 2

Literature Survey and Background

2.1 Introduction

This thesis is mainly a growth and a characterization study of thin films deposited by pulsed laser deposition (PLD). PLD is an established technique for a layer by layer deposition of two kinds of materials, namely 2 dimensional transition metal dichalcogenides (2D TMDCs), for electronic devices, and catalytic electrode materials, for solid oxide fuel cells. The materials studied in particular are MoS_2, a 2D TMDC material, and $La_{0.3}M_{0.7}Cr_{0.3}Fe_{0.7}O_{3-\delta}$ (LMFCr) where M = Ca or Sr (LCFCr and LSFCr). Preliminary studies into the theoretical simulation and fabrication of MoS_2 based devices have also been performed and presented.

The two kinds of materials were grown using PLD and their growths were optimized by the variation of PLD parameters. Based on the material and its applications, the growths were optimized for the most desirable properties as required for their respective applications. These thin films were characterized using material, electrical and optical characterization methods. This chapter presents a background on the process of PLD, a study of the materials being investigated as well as the techniques used to analyze the properties of these materials.

2.2 Pulsed laser deposition (PLD): a thin film deposition technique

There are several established thin film deposition techniques of different forms such as chemical, physical and wet methods with their own sets of advantages and disadvantages. Pulsed laser deposition is a physical vapor deposition technique, which is well established for the deposition of a variety of materials, especially those with complex stoichiometry [23]. Due to the relatively simple physical setup and the ability to tune the properties of the thin films by varying the deposition parameters, this technique has been used over the years for thin film depositions of several materials.

In this study, for the MoS_2 growth, PLD enables growth of relatively large area epitaxial thin films (when compared to exfoliation techniques) with the advantages of large and controllable area of thin film, and the ability to grow without the use of precursor gases or generation of toxic by-products as opposed to traditional fabrication techniques such as exfoliation and chemical vapor deposition (CVD) respectively. For LMFCr, PLD is used to reproduce the complex stoichiometry of the perovskite crystal, in addition to making it uniform and smooth, when compared with porous, non uniform and discontinuous films formed by tradition sol-gel techniques.

The technique in PLD involves the ablation of a target material using a high energy laser beam in pulsed intervals [24]. Ablation of material from the target causes a plasma plume consisting of material particles of ions, molecules and atoms to be kicked off from the target. These particles are then deposited onto the heated substrate material. The process of ablation involves thermal excitation of a small area on the target. This causes the generation of high energy target material cluster particles, atoms, molecules, electrons and ions which are ejected from the target. The presence of these high energy particles enables stoichiometric epitaxial growth at temperatures lower than several other growth techniques such as thermal evaporation, especially in cases where the melting points of targets are too high to be thermally evaporated [25].

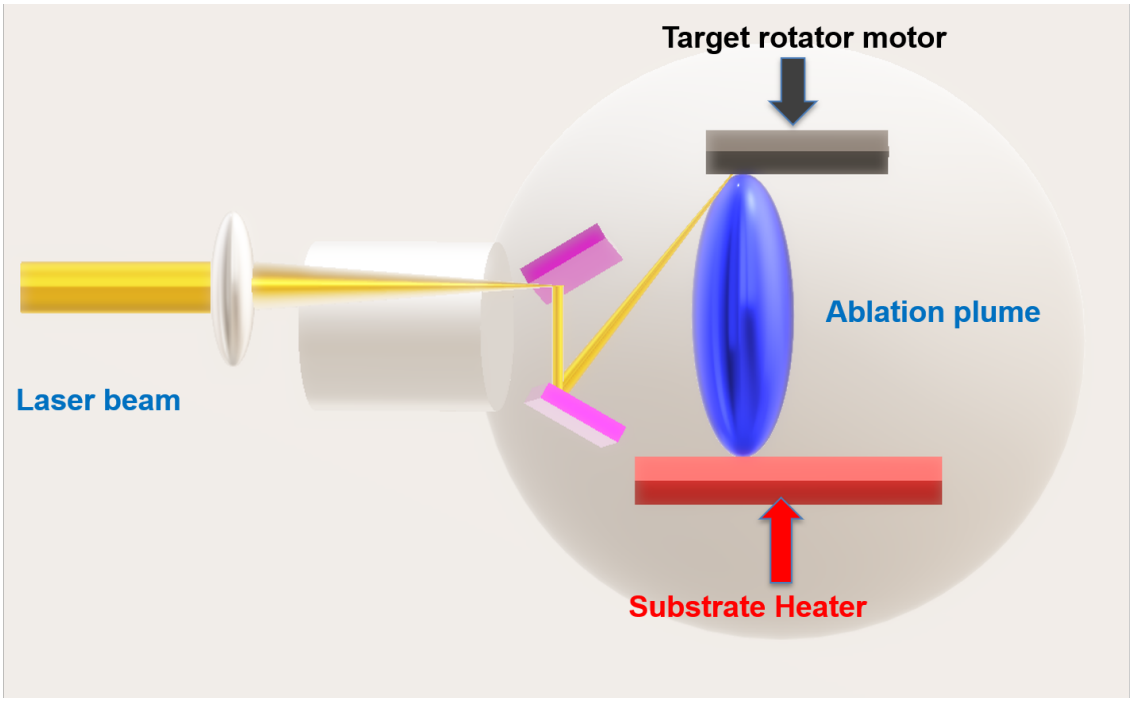

Figure 2.1: Schematic of the working of a PLD

Figure 2.1 is a schematic describing the working of a PLD process. A high energy 15 ns laser pulse is focused on a rotating target as shown using a lens with a focal length of 50 cm. This laser pulse causes ablation of the target material, which forms a high density plume as shown. Highly energetic particles from the target are then deposited onto a heated substrate. The target is rotated to ablate a different spot for each pulse, so as to reduce re-ablation of the same spot position on the target. The laser used in this study was a UV-248 nm KrF laser with 15 ns pulses.

The growth process in PLD can be split in four stages:

- Laser ablation of the target material
- Plasma formation and propagation
- Material deposition on the substrate
- Nucleation and thin film growth

Laser ablation from the target involves a localized heating, melting and evaporation of the target material. Ablation occurs when incident laser energy penetrates the surface of the target and removes some material from the target [25; 26]. The ablation produces a high density plasma. This high density - high energy plasma produces a plume of energy which propagates from the target towards the substrate in a conical plume. The laser energy density, or the laser fluence is measured as the laser energy on the target divided by the spot size of the ablation area on the target.

The ablation plume is formed at the point of ablation. The particles that are ejected include atoms, molecules, ions and electrons which continue to absorb energy from the laser, gaining high energy. Controlling the laser fluence can control the energy of the ablated particles, and hence, the quality and deposition rate of the thin films [27].

As the plasma propagates across from the target to the substrate, the ambient gas (such as Argon (Ar) for MoS_2 and oxygen for LCFCr) and the impurities present in the chamber at vacuum can act as retardants, and slow the particles down. Depending on the substrate target distance (varied from 3 - 5 cm in our studies),the formation of debris on the thin films can be controlled, thereby influencing the crystallinity. The density of the plume propagation follows a $\cos^{n}(x)$ relation from the target to the substrate, and therefore, variation of the substrate-target distance can influence the growth rate and the uniformity of the thin films.

Once the plasma particles arrive at the substrate, these adatoms deposit on the film in a few different modes of growth to form the thin film. The control of various PLD parameters can help influence this deposition for suitable applications [25].

As the film growth on the substrates, it can be characterized by different modes of growths illustrated in the Figure 2.2.

There are three main thin film growth modes [26]. In figure 2.2 (a), the Frank-Van der Merwe mode is illustrated, where there is a layer by layer arrangement of adatoms with the second layer forming carefully on top of the first. Due to the epitaxial nature of growth, these films tend to be very uniform and possess a higher degree of crystallinity. The second mode of growth is called the Volmer-Weber

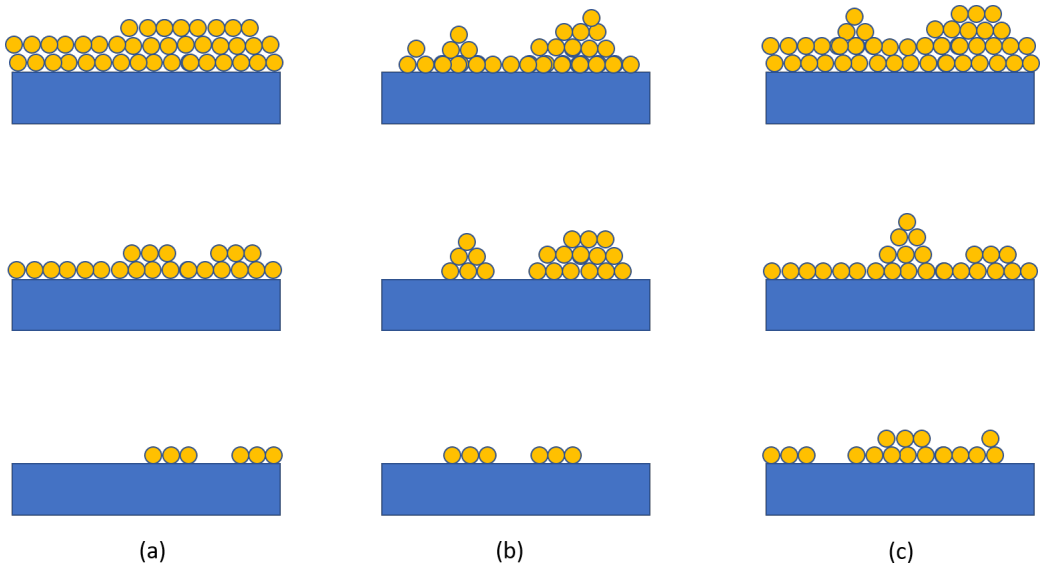

Figure 2.2: Schematic of the three different modes of growth with (a) Frank-Vender Merwe, (b) Volmer-Weber and (c) Stranski-Krastanov modes

growth mode, which is illustrated in Figure 2.2 (b). Here, there are nucleated sites that attract adatoms to form island like formations. The growth is more non-uniform than the previous case. The third mode of growth is illustrated in Figure 2.2 (c), which is the Stranski-Krastanov (S-K) mode. This is a combination of the first two modes, where the thin film initially begins by forming epitaxial layers and then forms nucleating sites which develop into form islands on the film.

In order to control the quality of the thin film grown, some of the key PLD growth parameters listed below can be varied to influence the nature of the thin film.

- Substrate: The orientation of the substrate surface can play an important role in the preferred orientation of the thin film grown by PLD.
- Laser fluence: Above the laser threshold of the target, the laser fluence with which the laser ablates the target can influence the film uniformity. With higher fluences, the energy of the particles kicked off from the target have higher energy, and therefore, can lead to more particulates and adatom clusters on the thin film being grown. Lower fluences can typically lead to more uniform layer by layer growth.

- Target - substrate distance: Due to the cosine law of distribution of particles from the ablated spot on the target, smaller substrate - target distance leads to faster growth due to the smaller mean free path. Higher target- substrate distances lead to larger areas of uniform growth, slower growth rates and lesser particulates.

- Post growth anneal: Post growth anneal periods at high enough temperatures can lead to higher crystallinity due to there being enough energy for larger crystals to form. However, at too high a temperature, due to the availability of excess energy, there can be changes in the crystal phase.

- Ambient growth conditions: The chamber pressure at vacuum in the growths was around $1x10^{-5}$ mTorr, with roughly $2.3x10^{17}$ molecules of oxygen in the chamber. Depending on the requirement of the thin film, presence of ambient gases can help improve the stoichiometry of the thin film, control the growth rate by influencing the energy of the ablated particles from the target, and avoid contamination of the compounds by providing inert environments of growth.

The parameters listed above were varied and the resulting effects on the film quality were measured and analyzed using material characterization techniques to extract crystal orientation and crystallinity, thickness, material grain roughness, size and other properties. The variation of these parameters and the characterization of the films have been explained in detail in Chapters 3 and 6 for MoS_2 and LMFCr respectively.

2.2.1 Advantages and Challenges of PLD

There are several advantages of PLD as a deposition technique for thin films. Some of the advantages include the nature of deposition which is a relatively conceptually simple process, with the ability to tune the properties of the thin films by varying the deposition parameters. There is no requirement of any process gas, or removal of any toxic byproducts unlike chemical deposition based techniques. Due to the high energy of the ablated particles from the target, the plasma plume consists of atoms, molecules, ions and electrons, leading to a higher efficiency in the deposition of complex stoichiometry of materials such as complex oxides and

other such materials [26]. As one laser can serve many vacuum systems, and high quality thin films can be grown repeatably over fairly short deposition time periods, this technique is also scalable, once the parameters are optimized.

While this technique has several advantages, there are also some disadvantages of this process. One of the main ones being the high scale of debris and droplet formation commonly found on the thin films as a result of the high energy of ablated particles. This can be resolved by working with lower laser fluence, increasing the ambient gas pressure or increasing the substrate-target distance. There can also be some level of inhomogeneity in the thin film due to the limited area of uniform plume coverage. This can be mitigated by substrate rotation and by increasing the substrate-target distance to increase the area of uniform coverage. Due to the nature of the process, it is also critical to ensure a high degree of smoothness of the target to allow for repeatable and efficient target ablation at different spots over the target [26].

2.2.2 Fabrication techniques of MoS_2 and LCFCr thin films

In order to obtain uniform large area thin films of MoS2 for these applications, several methods of synthesis have been explored. Some of the conventional techniques such mechanical exfoliation [28] and chemical exfoliation [29], are being used to achieve mono or few layers of MoS2 flakes size of 10 µm to hundreds of microns. While these techniques provide high quality thin films, some of the challenges include difficulty in the precise control of the size and the thickness of these films. These challenges can be overcome by methods such as chemical vapour deposition (CVD) [30] and sputtering [31], however, they require a high temperature of operation of up to 1000^0C along with the need for precursor gases, safe removal of volatile byproducts as well as additional post growth sulfurization steps for stoichiometric balance [32]. Therefore, conventional techniques such as mechanical exfoliation and chemical vapor deposition have downsides corresponding to the ease of fabrication of controlled size and thickness and the requirement of toxic process gases such as sulphur in this case, and safe removal of these toxins.

Pulsed laser deposition (PLD) has been studied over the recent years as an alterna-

tive approach to overcome these challenges [33]. It has been a well established laser plasma based material synthesis technique to grow complex compound materials with good stoichiometry along advantages such as in-situ control of thickness by variation of laser repetition rate, controlled area of deposition and repeatability of growth. It offers a precise control over the properties of the thin films by the variation of the growth parameters such as substrate lattice, substrate temperature, laser fluence, laser pulse repetition rate, substrate to target distance, deposition gas ambient pressure and post growth anneal period.

In the case of LMFCr, traditional techniques includes methods like sol-gel based spin coating methods and screen printing [34; 35]. There are several problems in the film quality such as regional inconsistencies in the elemental composition and morphology, high porosity and non-uniformity in the film along with a high roughness obtained on the surface [36]. This makes it difficult to study the material properties and characteristics of the catalytic materials, aside from issues with reproducibility.PLD is explored as an alternative method to deposit uniform thin films with a higher control over the stoichiometry, with a higher degree of uniformity enabled by variation of the PLD parameters.

As a result, there has been a great interest in the study of PLD techniques for large controllable area MoS_2 thin films and stoichiometric and dense and smooth LMFCr thin films.

2.3 Moore's Law

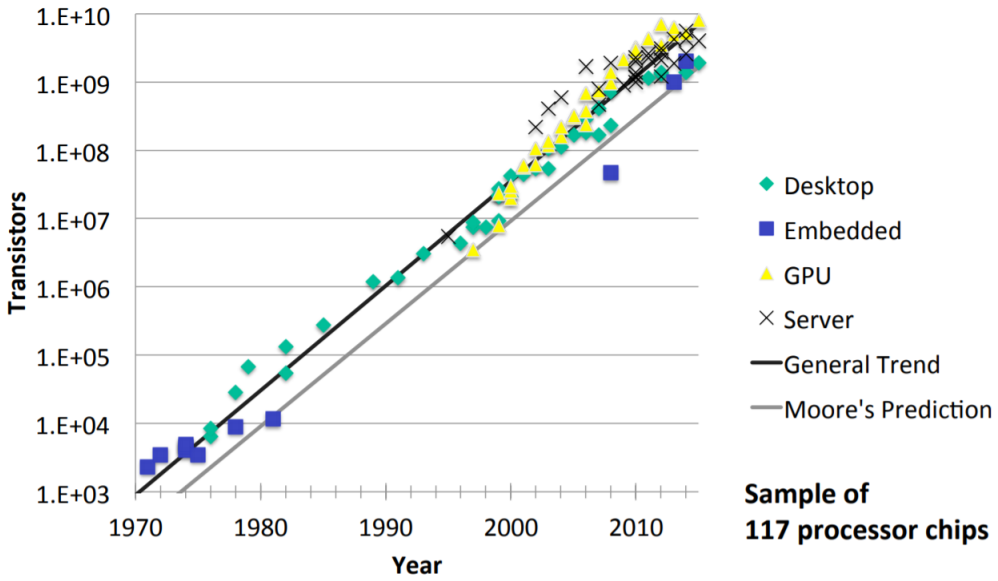

Figure 2.3: Schematic showing the Moore's law with the state of art over the years [37]

The history of electronic devices and circuits have been guided by Moore's law for over 50 years now. Transistor devices were first invented by John Bardeen, Walter Brattain and William Shockley in 1947, and soon, these devices gained popularity, as they began to be explored for a wide range of applications. In 1975, Gordon Moore predicted that the innovations in transistor technologies would increase at a high rate, with the number of transistors on a microchip roughly doubles every two years. Since then, research and development in the semiconductor industry has been driven by this law. The size of the transistors and components fabricated each year is growing smaller and smaller over time[38].

Conventional transistors involve a silicon based device with innovations in the design of the device structure and materials for the different components of transistors to keep up with Moore's Law. As the transistors get smaller, there are noticeable quantum effects, leakage currents and overheating issues. It has become harder and harder to keep up with Moore's law, which is desirable to keep up with the predicted pace of advancements in the industry over the years dictated by this law [39]. Novel materials and device designs are therefore, being explored to minimize

these effects and allow for scaling down to sub- 5 nm channel length devices, while providing comparable performance and resolving some of the issues posed by convention silicon devices [40].

2.4 2D Transitional metal dichalcogenides: MoS_2

Research in 2D semiconductor materials such as graphene has shown a large demand for scaled down electronic, magnetic and opto-electronic devices. This is due to the structure of the materials, which consists of multilayered 2 dimensional sheets of honeycomb structured layers stacked one on top of another connected by weak Van der Waal's forces. This class of materials has been posed to take over the future of transistor devices, as not only does it enable the scaling down of device size to keep up with Moore's law, it also presents unique properties with varying number of layers[41; 42] arising due to broken inversion symmetry and reduced dimensionality. Owing to a two dimensional sheet like structure with high mobility values at atomic layer thicknesses, they can be designed to allow for minimizing of leakage currents and defects due the absence of dangling bonds. These materials have been explored for several electronic device and sensor applications. Some of these applications have been shown in Figure 2.4.

The discovery of graphene in 2004 led to a new direction of semiconductor device research, as it is being explored for its potential use electronic devices owing to its 2D layered structure and unique electronic and mechanical properties [43]. With an extremely high mobility of 200,000 cm^2/Vs and a high thermal conductivity ranging from 3000 - 5000 W/mK, it is very desirable for electronic, opto-electronic and spintronic device applications [44; 45]. However, due to its zero bandgap, it is almost semimetallic in nature, and therefore it is difficult to use in switching applications such as in transistors [46]. In summary, due to certain limitations such as the lack of a finite bandgap, and in order to explore applications with different properties and behavior, other 2D materials such 2D Transition Metal Dichalcogenides (TMDCs) are being viewed as viable options for electronic devices, which have shown mobilities in the ranges of 100-1000 cm^2/Vs [47].

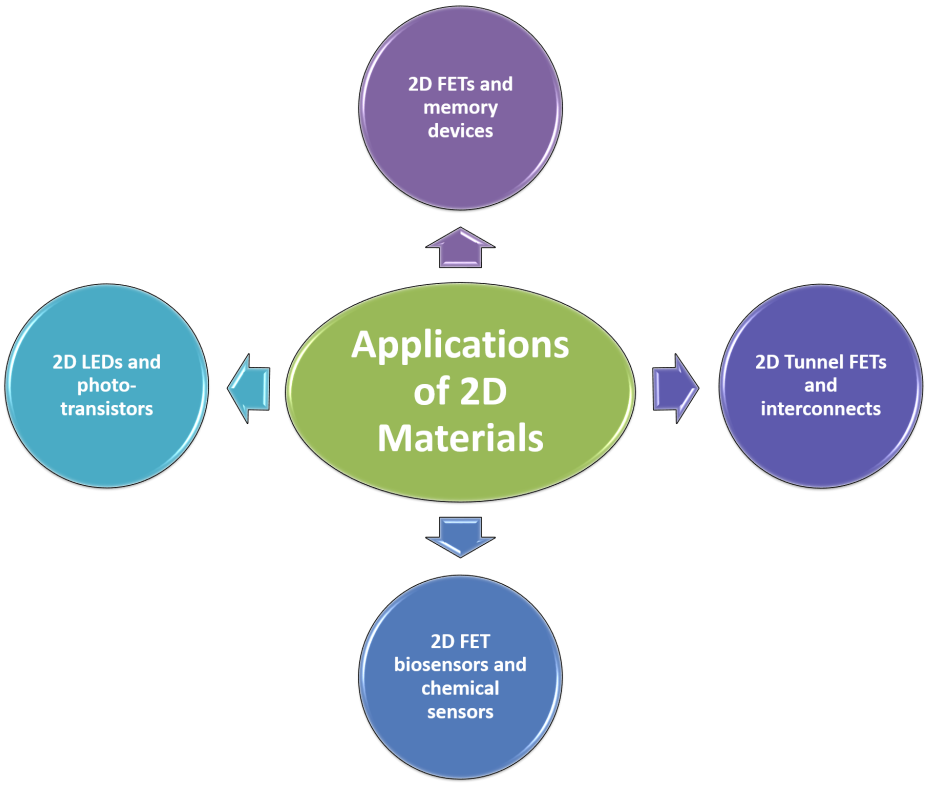

Figure 2.4: Some common applications of 2D materials in devices

The structure of a TMDC involves a transition metal 'M' such as Mo and W and a chalcogen 'X' such as S and Te to form MX_2, a transition metal dichalcogenide compound. Multilayer TMDCs consist of 2D monolayers which are simply stacked upon each other, connected by weak van der Walls force. Some of these semiconducting materials such as MoS_2, $MoSe_2$, WS_2, WSe_2 and $MoTe_2$ possess a direct band gap as monolayers, leading to applications in optical devices [48]. As the number of layers increase, there is change from direct to indirect band gaps. Coupled with increased quantum effects as the number of layers reduce from a few layers to monolayer limits, varying electronic [49], optical [50] and mechanical properties[51] can be observed in the thin films, paving way for several new exciting opto-electronic and nanoelectronic device applications [52].

An illustration of the structure of 2D materials has been shown in the Figure 2.5. The structures have been extracted from Quantumwise software by Junsen Gao.

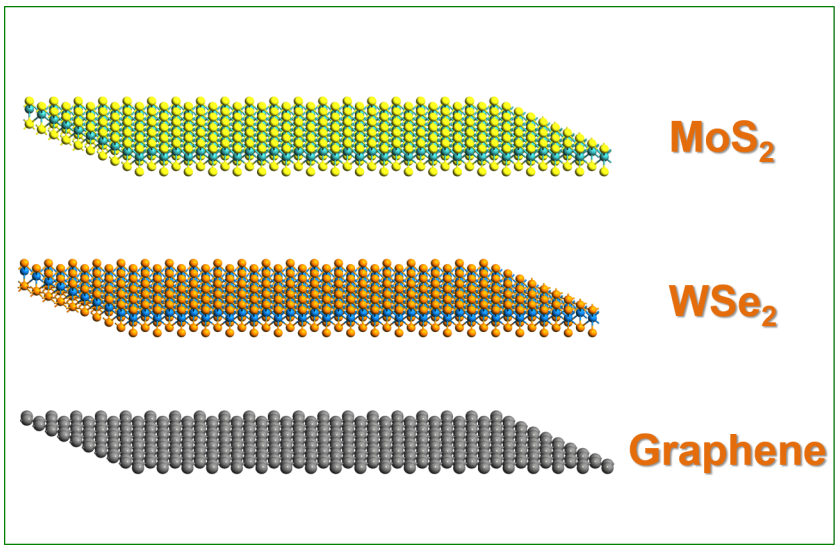

Figure 2.5: Illustration of the structure of 2D materials

2.4.1 MoS_2

Molybdenum disulfide (MoS_2) is one of the novel TMDC materials. In nature, MoS_2 is present in 2 phases, 2H (hexagonal symmetry) and 3R (rhombohedral symmetry). Both these phases of MoS_2 are semiconducting. The structure of semiconducting 2H-MoS_2 as shown in Figure 2.5 consists of closely packed hexagonal structure of S-Mo-S atoms connected over a 2D sheet. Each sheet forms a single monolayer of MoS_2 of around 0.65 nm in height, which can then be stacked up, one on top of another bound by weak Van der Waals forces to form multilayer thin films. While the 3R phase is also semiconducting, it is difficult to distinguish between the monolayers in this structure of MoS_2 and hence, predominantly, 2H-MoS_2 is studied for 2D TMDC material based electronic device applications[53]. A third meta-stable semi metallic phase with tetragonal symmetry can also be synthesized to form the 1T phase of MoS_2.

2H-MoS_2 possesses a direct bandgap (E_G = 1.8 eV) as a monolayer and an indirect bandgap (Eg = 1.2 eV) as a multilayer (bulk) thin film (> 8 ML), as a semiconducting phase [54]. As a 2D TMDC material, MoS_2 exhibits a change in optical, electronic and mechanical properties with the change in the number of monolayers, there have been several applications of MoS_2 thin films such as in flexible thin film transistors [55], gas sensors [56], phototransistors [57] and electrodes for Li-ion

batteries [58].

MoS_2 has shown promise as a 2D TMDC material for electronic transistor device purposes due to the potential for scaling down of these devices and for flexible device applications. The electronic mobility of MoS_2 has been observed to vary from around 10 cm^2/Vs as a monolayer to around 400 cm^2/Vs as a multilayer film [59; 60]. Experimentally demonstrated monolayer thin film transistors has shown an ON/OFF current ratio of as high as 10^8 with a subthreshold swing of 7.4 mV/decade, which is considerably lower than that of scaled silicon based MOSFETs which is around 70 mV/decade. This allows for a better device sensitivity and a better channel control, leading to lower current leakages and better performances and efficiency [61]. Due to the absence of surface dangling bonds also, MoS_2 based transistors can be scaled down substantially without an increase in leakage current, leading to sub 5 nm transistors demonstrated in the recent years [62]. Due to the stability of its properties under mechanical strain, and a Young's modulus of 0.33 +/- 0.07 TPa [63], which is comparable to graphene, it has also shown to be a promising candidate for large area flexible thin film devices.

2.5 Electrode materials: LMFCr

In recent years carbon capture and utilization (CCU) has drawn great attentions to researchers as an alternate approach to counter climate change by the emission of carbon dioxide and other fossil fuels[64; 65; 66]. Current research focuses on methods to utilize the excess CO_2 for energy utilization. Reversible fuel cells, specifically reversible solid oxide fuel cells (RSOFCs) are being actively explored for this purpose. The process in an electrochemical cell is governed by two electrochemical half reactions where electrons are generated at the anode of the cell during oxidation, and then passed through an external circuit to the cathode where the reduction reaction occurs. These two cell halves can be used reversibly to either generate fuel or store energy. Solid oxide fuel cells and electrolysis cells consist of thin film layers forming the anode, cathode, catalytic materials on both ends, contact materials and isolation layers for all of these components [67].

RSOFCs typically work in high temperature 800-1000^{0}C environments under two modes of operation as solid oxide fuel cells(SOFCs) to generate electricity and as solid oxide electrolysis cells (SOEC) to store energy [68]. They are currently being explored as alternatives to conventional energy storage and carbon capture methods. These advanced electrochemical systems comprise of electrode material catalysts that can help improve the efficiency of carbon capture and energy conversion.

Existing materials for fuel cell electrodes are Ni-YSZ (yttria stabilized zirconia) or LSM (lanthanum strontium manganite), both of which face issues with oxidation at high temperature environment, sulfur poisoning and delamination from the electrode and thereby lowering the fuel cell performance [69]. Due to these disadvantages, alternative materials are being explored. Mixed ionic electronic materials (MIECs) are one such class of materials that have been used to develop catalytic electrode materials to improve the carbon-dioxide conversion efficiency while overcoming these challenges [70]. MIECs such as perovskites have been studied to replace these materials to perform as both fuel and oxygen electrodes. One of the major advantages of these materials is that they have both ionic and electronic conductivity in one phase. When these materials are deposited on an electrolyte, due to the mixed ionic and electronic conductivity exhibited by these materials, a larger surface area is available for oxygen interaction. This is opposed to just the junction areas between the electrode material and the electrolyte being present for this interaction in purely electronic materials such as LSM [71].

As Perovskite materials have shown to perform well as both as fuel and oxygen electrodes in RSOFCs, The Birss group has worked with a novel perovskite material ($La_{0.3}M_{0.7}Fe_{0.7}Cr_{0.3}O_{3-\delta}$ (M = Ca, Sr),) to use as a reversible oxygen electrode both operating modes (SOFC/SOEC) of RSOFCs. Improved carbon dioxide conversion efficiency has been shown using this material in SOFCs [72].

2.6 Material characterization techniques

Both MoS_2 and LMFCr were grown using PLD and the growth parameters were varied to obtain thin films suitable for electronic device and electrochemical cell applications respectively. The background for some of the most important techniques used for the material and electrical characterization of these materials have been explored in this section.

2.6.1 X-Ray Diffraction

X-Ray diffraction (XRD) is a material characterization technique that can be used to study the crystal orientation of the deposited thin films [73]. The basic mechanism of XRD involves constructive and destructive interference of monochromatic X-ray beams and the sample being measured. The X-rays are produced by a cathode ray tube (called the X-ray tube in a XRD tool) which are first filtered and collimated to produce a concentrated monochromatic source which is directed towards the sample placed on the sample holder at a specified angle of incidence. When the rays produce constructive interference with the crystal sample, diffracted X-rays are produced. This occurs when the conditions of Bragg's law are satisfied, which is given below.

$$n\lambda = 2dsin\theta \tag{2.1}$$

Where λ is the wavelength of the beam, θ is the angle made by the diffracted ray with the horizontal plane and d is the lattice spacing within the crystalline sample. This law is illustrated in the Figure 2.6.
These diffracted X-rays are collected by the X-ray detector over a range of 2θ values to obtain all the orientations that correspond to the different diffraction angles. Based on the 2θ peaks position and full width to half maximum (FWHM), the crystal orientation and crystallinity of the sample can be predicted.

2.6.2 Atomic Force Microscopy

Atomic force microscopy (AFM) is a scanning probe microscope that uses piezoelectric feedback for the imaging. AFM consists of a small piezoelectric cantilever attached to a small and sharp tip [74]. There are two modes of operation based

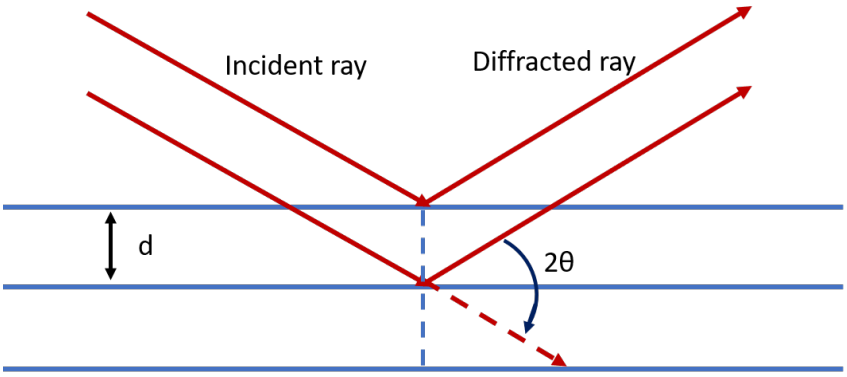

Figure 2.6: A schematic of the working of XRD, where λ is the wavelength of the incident X-ray, d and 2θ are as shown.

on whether the sharp tip is oscillated up and down on the surface, or is in contact with the surface throughout, which are called tapping mode and contact mode respectively. This AFM was used in the tapping mode for all the imaging performed in this study so as to not damage the soft surface of some of the samples that were being imaged. The tapping mode involves an oscillatory movement of

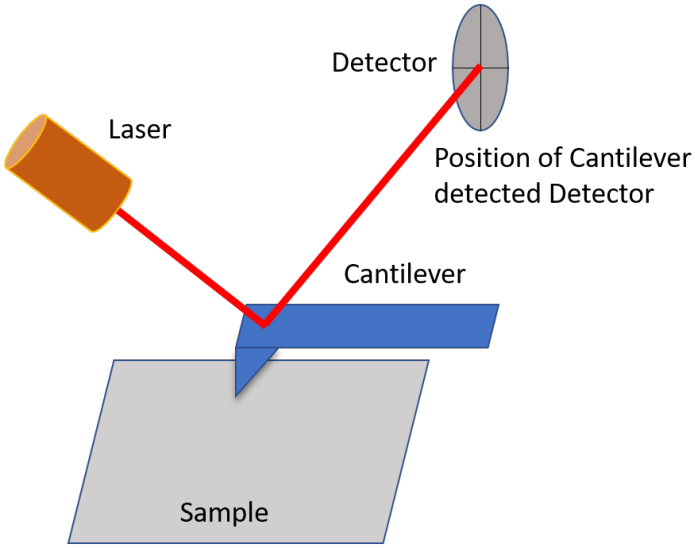

Figure 2.7: A schematic illustrating the working of AFM in tapping mode

the piezoelectric cantilever across the surface being scanned. As it scans across the morphology of the films, there is a variation in the height position of the cantilever. A laser source is aligned with the cantilever to detect these changes by the detected reflected laser beam, which allows an efficient imaging of the surface morphology

across the scan area. The working of the AFM is illustrated in Figure 2.7.

2.6.3 Helium Ion Microscopy and Field Effect Scanning Electron Microscopy

Helium ion microscopy (HiM) and field effect scanning electron microscopy (FESEM) are two techniques that utilize focused ion and electron beams to image the film surface morphology. The basic working principle of the FESEM has been illustrated below in Figure 2.8. Here, due to the small wavelength of electrons, the resolution of SEM tools is improved beyond that of optical microscopes [75]. The mode of focusing of electrons using a field emission gun improves this resolution much further in FESEM. This tool works on the principle of concentrating and exciting electron beams down onto a sample as shown below. When the electrons interact with the atoms on the surface, they generate secondary electrons which are collected by the secondary electron detector to provide an image of the surface topology and morphology.
HiM works by a similar principle where instead of excited and focused electron beams, helium ion beams are used. These have a higher rate of secondary electron generation when compared to FESEM and SEM along with having a smaller probe size, creating a better signal with a higher contrast, therefore, giving a much better resolution than SEM. This makes it more suitable for thinner and softer samples like MoS_2. HiM was mainly used to image the surface morphology of the materials grown using the PLD.

2.6.4 X-Ray Photoelectron Spectroscopy

X-Ray photoelectron spectroscopy (XPS) allows for a unique identification of elements and their states present in a particular sample based on the photoelectrons emitted from the atoms present in the sample, and is a surface technique [76]. High energy X-Rays are irradiated on the sample surface being measured. The energy of the X-Rays causes photoelectrons to be ejected from the atoms constituting the material in the sample, which are collected and and analyzed to find the binding energy corresponding to the transistion of that photoelectron. This helps identify the different states of the elements present in the sample and therefore,

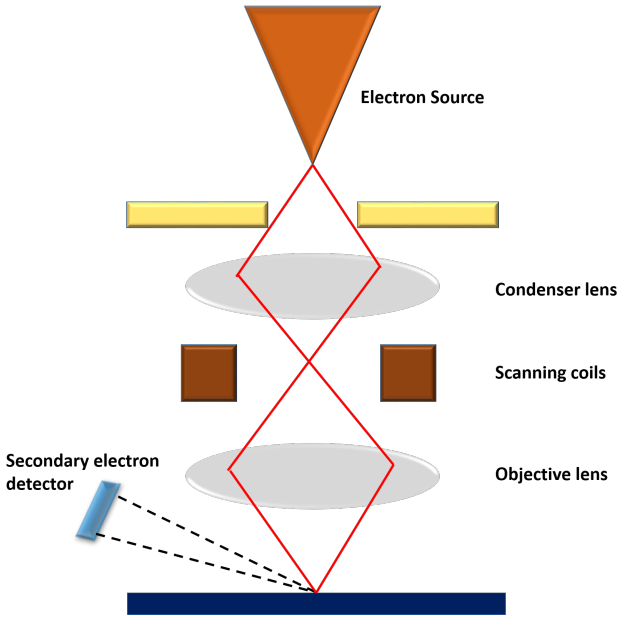

Figure 2.8: Schematic of the working of SEM

the probable compounds present in the sample corresponding to these states.

2.6.5 Raman Spectroscopy

Raman Spectroscopy has been used in this study to analyze the vibrational modes of the crystals of MoS_2 deposited by PLD. In this technique, the properties of the material crystals such as inter and intra molecular vibrations which in turn provides information about the crystal lattice and the molecular structure within the material [77].

The Raman effect, or Raman scattering refers to the phenomenon of inelastic scattering of incident photons due to an exchange of energy between the photons and the matter it is incident on. This change in the energy corresponds to a unique signature vibrational energy of the molecular vibrations within that matter, which can be recorded to analyze the properties of the crystal lattice and the vibrational modes of the molecules within that lattice.

2.6.6 Profilometry

Profilometry is a standardized technique for profile and thickness measurements of thin films. In this study, a stylus profilometer was adopted. Here, a stylus tip is used to physically scan across the Z profile of the surface. The stylus tip requires the force feedback from the changing topology of the surface while it scans across a specific direction. The lateral resolution of this technique is limited by the size of the stylus tip, which in this case was 5 μm.

2.7 Electrical characterization techniques

Material characterization provides information about the thin film morphology, crystal structure and composition but for device applications electrical properties like sheet resistance and mobility of the material are required to be measured and studied. Here, we utilize four point probe and Hall measurement for electrical characterization of the films.

2.7.1 Four point probe

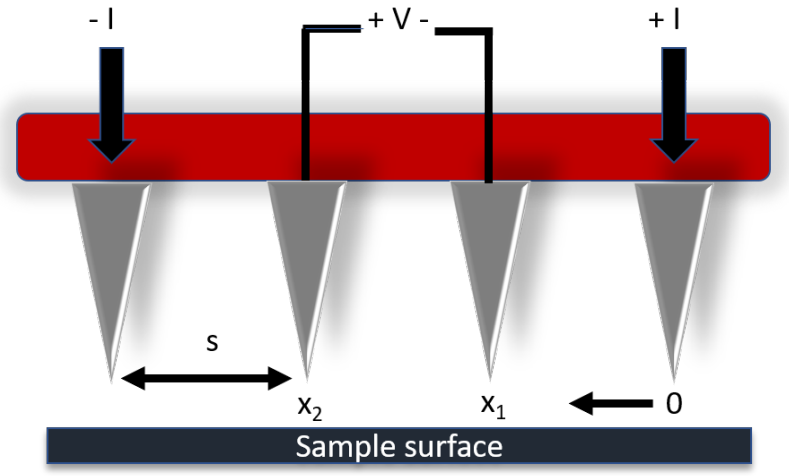

Figure 2.9: Schematic of a four point probe measurement

The four point probe measurement is a technique used to measure the sheet resistivity (conductivity) of a thin film sample, when the sample thickness 't' is much

smaller than the spacing of the probes 's' as shown in Figure 2.9. As the current and voltage electrodes are separated in this technique, it eliminates the lead and contact resistances from this measurement, which is especially useful in the measurement of low values of resistances, and is therefore, superior to two wire measurement setups. In this technique, a current is passed through the outer two probes as shown, while the voltage is recorded by the inner two probes [78]. When the thickness of the thin film is approximated as t, it is possible to extract the resistivity of the thin film sample from the equation 2.2.

$$\rho = \frac{\pi t}{ln2} * \frac{V}{I} \tag{2.2}$$

Here, ρ is the resistivity, and V and I are the measured voltage and passed current respectively. The reciprocal of the resistivity of the thin film is calculated as the conductance of the thin film sample. This method was used for the calculation of conductivity of multilayer MoS_2.

2.7.2 Hall measurement and mobility extraction

Mobility of a thin film is a very important parameter when it comes to studying the potential for its applications in transistor and other electronic device applications. Carrier mobility is an intrinsic property of a thin film which gives a measure of the extent of the ability to maximize currents in a particular electronic device, thereby, improving the performance of the device. This becomes particularly important in transistor devices where a high turn on current is desirable.

One of the most well-established techniques of thin film mobility measurements is the Hall measurement using Van der Pauw method. In this technique, Hall voltages corresponding to applied magnetic fields can be used to calculate the mobility, given information about resistivity and thickness of the thin film.

The Hall effect occurs in a conductor (or semiconductor) when mutually perpendicular current and magnetic field are applied to the conductor (or semiconductor) and a Hall voltage is observed in a direction perpendicular to both the current and the magnetic field. This effect is used in Hall measurements in thin films, where a current is passed through two opposite corners of a Van der Pauw structure,

magnetic fields are applied in a direction away and towards the plane of the thin film, and the voltage obtained across the other two corners of the structure are recorded. Hall measurements for thin films are performed using a standard Van der Pauw method of Hall voltage measurements, which can be used for the measurement of Hall voltage of irregularly shaped thin films [79]. The ideal contacts for the thin films should be ohmic, and placed either in a clover leaf formation or a square formation as shown in the Figure 2.10.

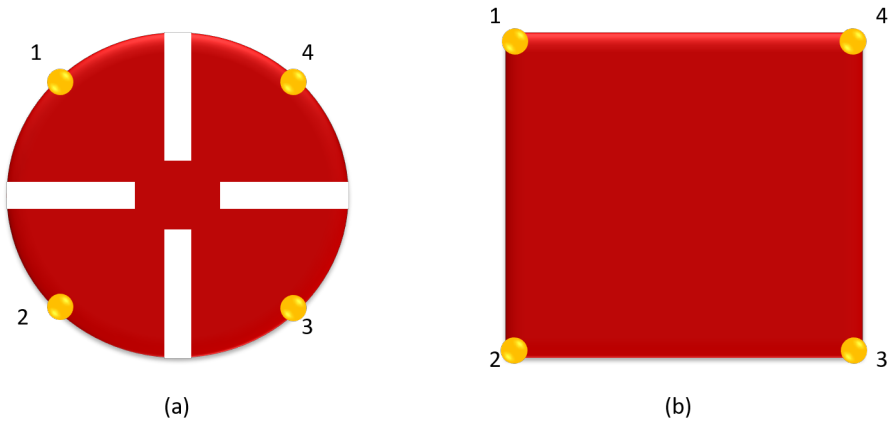

Figure 2.10: Schematic of contact placement for Van der Pauw measurement

The Van der Pauw method and the calculations performed to measure the Hall voltage, and from it, electrical properties such as mobility, resistivity and carrier concentration has been explained in detail in Chapter 4.

2.8 Device fabrication methods adopted

Once material and electrical characterization of PLD grown MoS_2 were performed, based on the film properties, devices were fabricated by using PLD grown MoS_2 thin films. On the experimental front, heterojunction P-N diodes were fabricated with Si as the p-type layer and MoS_2 as the n-type layer with Au contacts.
In order to fabricate the P-N diode, two kinds of p-type Si wafers were employed, one with a high doping of $5x10^{19}/cm^3$ and with a lower doping of $5x10^{15}/cm^3$. These wafers were diced and cleaned with piranha cleaning to remove the contaminants and buffer oxide etching to remove the native oxide layer on top of the

wafer. The details of the experimental parameters will be explained in Chapter 4. After this, 15 nm of MoS_2 was deposited onto these substrates using PLD with a shadow mask to avoid MoS_2 deposition on some regions on the substrate. Optical lithography was employed after this step to pattern the Au electrode region on top of the thin film and the Si region, and the metal was deposited using Electron beam evaporation. After metal deposition, liftoff was performed to form the electrode contacts on MoS_2 and Si. Some of the devices were isolated by scratching rectangular regions as shown in Chapter 4 to form the devices.
Some of the experimental techniques used for the fabrication have been described below.

2.8.1 Optical Photolithography

A schematic for the process of optical photolithography is presented below in Figure 2.11.

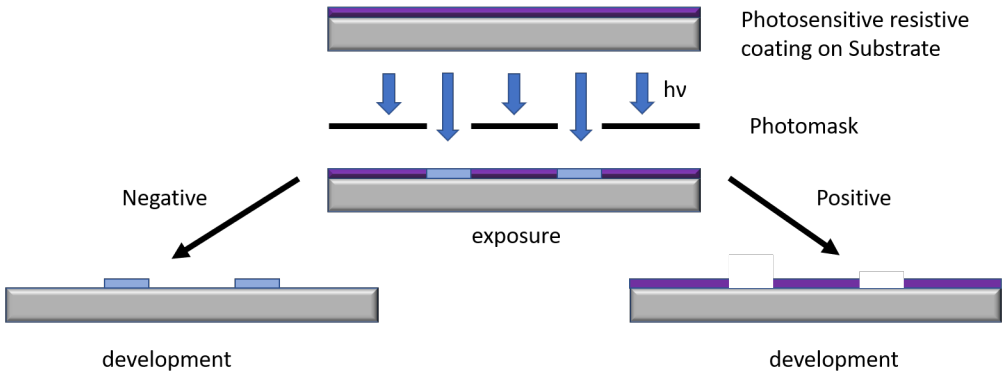

Figure 2.11: Schematic of optical photolithography process

While the process flow of the fabricated device has been explained in Chapter 5, the general process flow of optical photolithography begins with the coating of a substrate or a thin film on a substrate with a photosensitive resist using techniques such as spin-coating. The resist is then exposed to UV light with a mask on top of it. Depending on the nature of the resist, either the regions exposed or the regions covered by the mask remain on the substrate after washing with a developer as shown in the figure. Further steps after patterning would include either etching or further deposition and lift off depending on the process and design of the device to be fabricated.

2.8.2 Electron beam evaporation

The technique used for Au deposition on patterned MoS_2 thin film on Si substrate was Electron beam evaporation. This process involved the use of a high voltage electron beam used to thermally energize the target material stored in a crucible at high vacuum. The energy allows for the target material to be turned into gaseous state, which then proceeds to deposit and coat the surfaces directly within the line of sight of the target. The thickness of the target material being coated is measured by a crystal monitor.

2.9 Device simulation methods adopted

Simulation of MoS2 devices were conducted using two different packages like NanoTCAD ViDES and Synopsys TCAD. The simulation of Schottky contacts and transistors were conducted to optimize the device design using thin films of MoS_2. There are some limitations in terms of conducting simulations due to the lack of simulation packages for 2D semiconductors in most of the packages. Broadly, metal - bulk MoS_2 interfaces were sought to be studied to understand the nature of the contact formed between them. In addition, transistor characteristics with monolayer MoS_2 were simulated with different channel lengths to study the effect of dimensions on the device behavior.

In Synopsys TCAD, a preliminary material parameter file for MoS_2 was generated using the properties of the materials known from literature. Using this material parameter file, Metal-MoS_2 interfaces of three different metals with MoS_2 were simulated and their characteristics were extracted and analyzed. Transistor simulation for monolayer MoS_2 based transistor devices was performed using NanoTCAD ViDES to study the effect of channel length on transistor properties. A brief background about the two different simulation software used has been discussed below.

2.9.1 NanoTCAD ViDES

This open source software has been developed by Dr. Gianluca Fiori [80]. This is a python based module with routines built in C and Fortran and integrated into

these modules. Self consistent Poisson equations, Schroedinger equations by using Non Equilibrium Green's Function (NEGF). Transport computation in several 2D materials such as 2d TMDCs, Silicene and graphene and other such materials can be performed using this software. In addition, modules for the simulation of MoS_2 and graphene based thin film FETs can be performed. Further information of the simulation can be found in Chapter 4.

2.9.2 Synopsys TCAD

This software is an industrial standard for the simulation of complex bulk 2D and 3D devices [81]. Unfortunately, this software does not yet have transport models for MoS_2 and other such 2D materials, and therefore, a material parameter file had to be created for the simulation of Schottky devices using known parameters and approximations. This software contains many inbuilt functions and modules for device geometry creation, device physics optimization and visualization, which were all used for the simulations. Further information on the simulations can be found in Chapter 4.

Chapter 3

Pulsed laser deposition of MoS_2 thin films

Pulsed laser deposition as a growth technique was explored for large area growth of MoS_2 thin films with control over a monolayer thickness of growth in order to make layer by layer growth possible. Controlled large area deposition of MoS_2 made possible by the PLD technique would allow for large area scalable fabrication of electronic devices.

This chapter focuses on the growth of MoS_2 by the optimization of PLD growth parameters such as substrate, substrate temperature, post growth anneal period and deposition gas ambient pressure to achieve highly crystalline large area thin films of MoS_2. These films have been analyzed using material characterization techniques such as X-ray diffraction spectroscopy (XRD) to study the crystallinity, atomic force microscopy (AFM) to study the surface morphology and roughness, helium ion microscopy (HiM) to image the surface morphology and X-ray photoelectron spectroscopy (XPS) to study the elemental states present in the thin film. Transmission electron microscopy (TEM) was used to study the lattice structure of the deposited MoS_2 thin films.

Optical characterization using Raman spectroscopy has been performed to approximate the number of monolayers of the deposited films. Transmission and absorption studies have been performed for different thicknesses of the deposited

films to study the excitonic transitions in the samples. Electrical characterization of the bulk thin films using four-point probe has been performed to study the conductivity of these thin films. Preliminary Hall measurement has also been performed for the thin films to study electrical properties such as mobility, resistivity and doping concentration, which has been discussed in detail in the next chapter.

Films ranging from a thickness of 2 nm (3 monolayers) to around 60 nm (92 monolayers) have been deposited and characterized for their material, optical and electrical properties.

3.1 Experimental setup of the PLD system

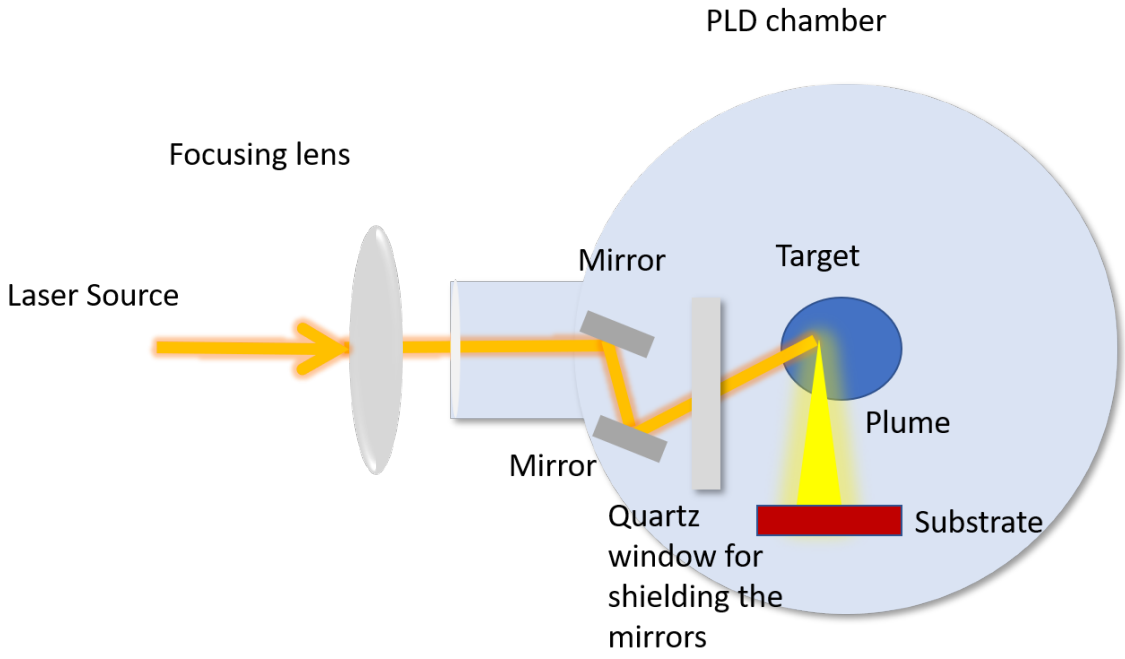

Figure 3.1: The setup of the PLD system used for all the depositions

The PLD setup used for the growths has been presented in Figure 3.1. In all of our experiments, a LambdaPhysik KrF laser was used for 248 nm pulsed laser shots for target ablation. Due to the position of the laser, three mirrors were used to direct the laser beam towards a focusing lens with a focal length of 50 cm. This

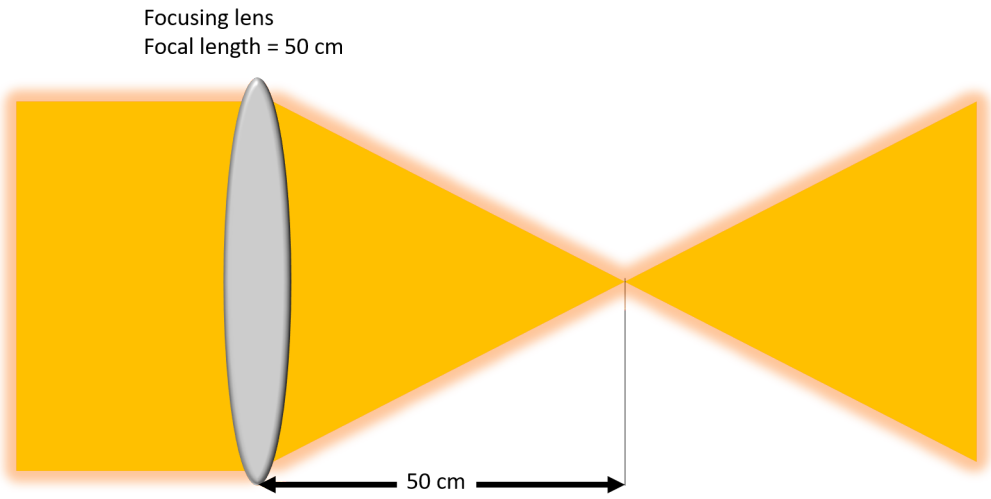

Figure 3.2: Schematic of a laser beam's path as it converges through a focusing lens. Spot formation on a thermal paper at different focal distances from the focusing lens is also shown.

beam was then focused onto the target at an angle of 45^0 by adjusting the mirrors inside the PLD chamber to change the focal distance of beam between the focusing lens and the target to change the spot size of the focused beam.

Figure 3.2 shows a schematic of the laser beam travelling from infinity as it converges after passing through the focusing lens. A desired fluence was achieved by adjusting the mirrors inside the PLD chamber as well as the position of the focusing lens, both in order to vary the focal distance from the lens to the target, thereby changing the spot size of the focused beam. The target was positioned at a desired distance from the substrate for the depositions.

The laser energy was measured by using a setup as shown in Figure 3.3. Here, the collimated laser beam was reflected onto a PY5 optical calorimeter by placing a wedge before the focusing lens. This reflected 4% of the laser energy onto the calorimeter. The calorimeter was connected to a Tektronix digital oscilloscope, where the voltage corresponding to the laser energy incident on the calorimeter was measured and recorded as V. The conversion factor of the calorimeter was 2.11 V/J. Therefore, the energy of a laser pulse was calculated by the formula shown

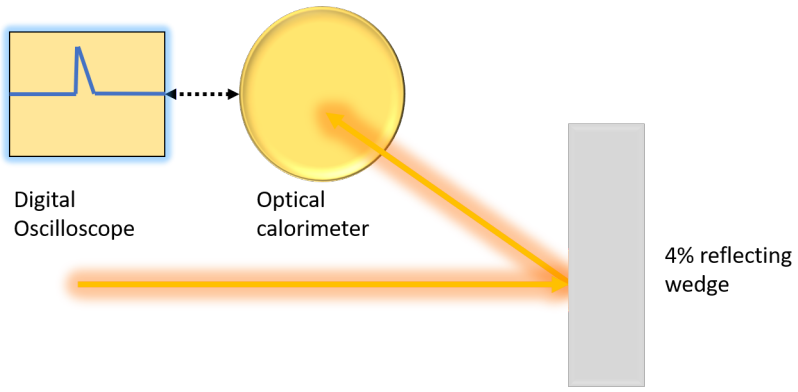

Figure 3.3: Optical set up for laser energy measurement

below.

$$E = \frac{V}{0.04 * 2.11} \tag{3.1}$$

The fluence F was calculated by the formula shown below.

$$F = \frac{E}{s} \tag{3.2}$$

Where 's' was the area of the spot measured on the thermal burn paper and on the target. The fluence used for all of the growths in this chapter, was around 2.2 J/cm^2.

Figure 3.4 shows a labeled diagram of the components of the PLD setup used for the growths. After measurements of fluence, substrates were mounted onto a 2 inch Neocera conductive substrate heater using custom made clamps and the chamber was shut for pumpdown. The Neocera substrate heater has the capability of heating substrates to a temperature of up to 950^{0}C. First, a roughing vacuum pump was used to bring down the pressure in the chamber to around 200 mTorr. After this, the foreline valve from the roughing pump to the diffusion pump was opened to pump the backing line. The diffusion pump heater was then turned on for an hour to heat the oil. After an hour, the roughing line to the chamber was closed and the cold trap was filled with liquid nitrogen. The gate valve from the diffusion pump to the chamber was then opened. The cold trap was used to condense the vapors in the chamber, allowing for a faster and more efficient pumpdown diffusion pump. In about 15 minutes, a base pressure of 1x10^{-5} to 7x10^{-6} T was obtained. Chamber pressures of upto 10 mTorr were measured using a Low Vacuum Pirani

gauge and higher vacuum pressures upto 10^{-6} T ranges were measured by Cold cathode high vacuum gauge.

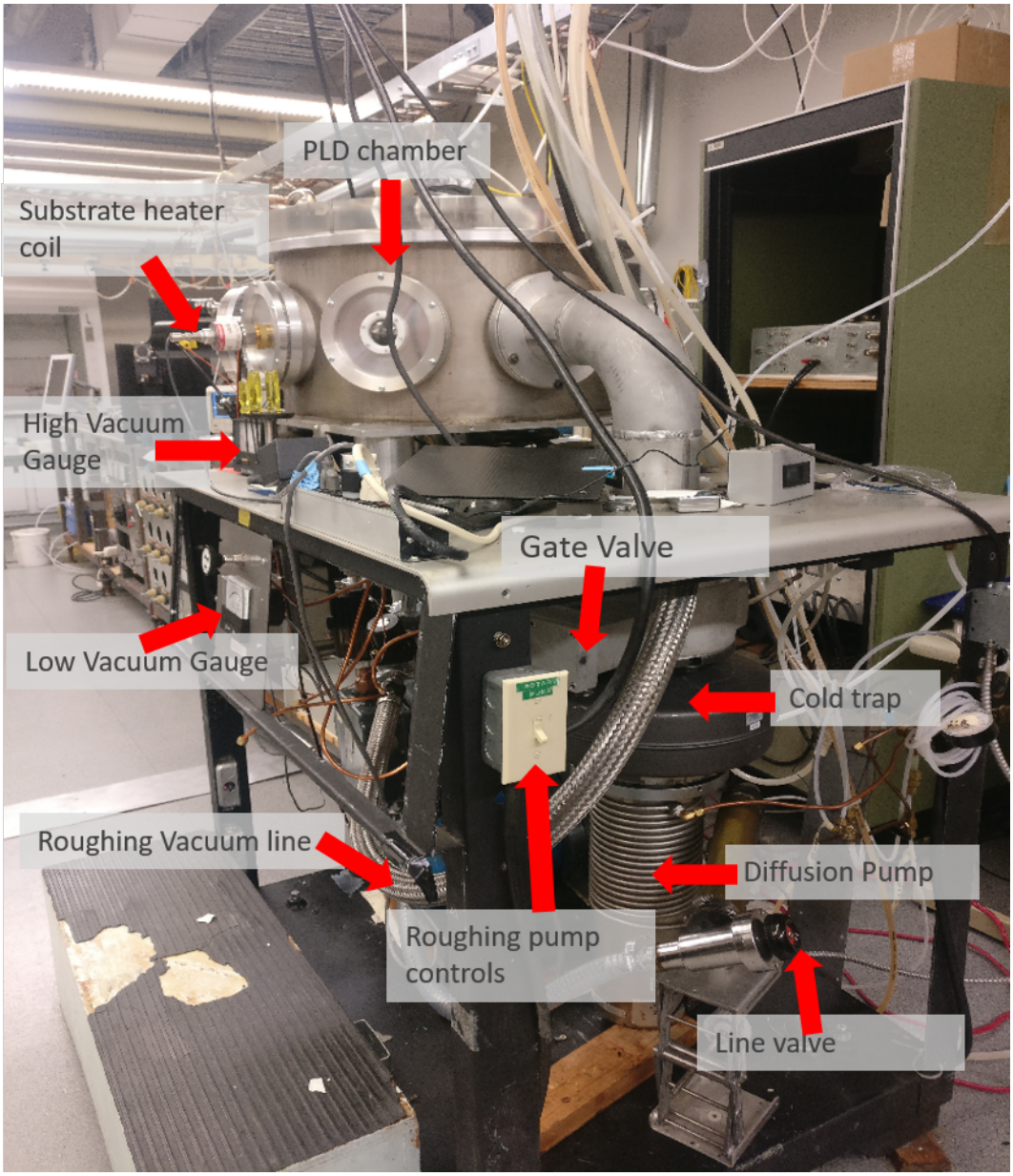

Figure 3.4: A labeled diagram of the components present in the PLD setup used for the growth experiments

Argon (Ar), an inert gas was introduced into the chamber from a gas inlet during the growths to minimize oxidation of the thin film. The temperature of the

substrate holder was controlled by a Eurotherm PID controller, and the required temperature was set by increasing it at a rate of 20^0C per minute. The laser shot frequency was set, and the target rotation was enabled to perform the growth. After performing the growth and a post growth anneal, the substrate temperature was reduced, the ambient gas inlet valve was closed and the gate valve to the diffusion pump was closed once the substrate temperature was reduced to less than 50^0C. Nitrogen gas was used to vent the chamber to atmospheric pressure in order to remove the substrates after growth.

The pulsed laser deposition of MoS_2 was performed by using a commercially available MoS_2 target from Kurt Lesker with a 99.9% purity. The laser used for the ablation was a KrF excimer laser (248 nm, 15 ns, 5 Hz) at a laser fluence of 2.2 J/cm^2. A chamber base pressure of 1x10^{-5} to 7x10^{-6} T was obtained for all of the growths.The different substrates used for the growth included (001) sapphire (Al_2O_3), (001) quartz, silicon dioxide on silicon (SiO_2/Si) and silicon ((100) Si). The substrate temperature was varied from 450^0C, 700^0C, 800^0C and 850^0C. Argon as an inert gas was used as the ambient gas during depositions to reduce interactions of impurities with the film and to minimize oxide formation (MoO_3) in the film. The Argon gas pressure was varied from 0 to 10 mTorr. The post growth anneal period was maintained at around 30 minutes at the temperature of growth in vacuum. The different thicknesses of thin films grown range from 3 nm to 60 nm.

3.2 XRD and 4 point probe studies

XRD and 4 point probe were used to study the crystallinity and the electrical conductivity of the thin films respectively, with change in PLD parameters such as substrate, substrate temperature and ambient pressure of Ar gas during deposition. Measurements on bulk MoS_2 thin films with change in these parameters were carried out as it easier to measure thicker films on XRD and the four-point probe. This was because thinner films are more difficult to align for thin film XRD measurements, and thinner films pierce easily with the probes of the four point probe leading to difficulty in measurements. The films were optimized for the smallest full width half max (FWHM) of the (002) peak of MoS_2 for a higher

crystallinity in a crystal orientation parallel to the plane of the substrate surface, and a higher conductivity which could correlate to higher mobility in the thin films for electronic device applications.

Glancing angle X-ray diffraction spectroscopy (XRD) was used on the Rigaku Ultima IV to study the crystallinity of the thin films. A glancing angle of 0.50^{0} with a 2θ sweep from 10 to 25^{0} was used for these measurements. Electrical characterization of the bulk thin films using the Keithley four-point probe was performed to study the conductivity of these thin films.

The dependence of substrate temperature on the thin film quality was explored by growing bulk MoS_2 thin films of a thickness of around 60 nm on quartz at 250^{0}C, 450^{0}C, 700^{0}C, 800^{0}C and 850^{0}C. The thickness of these films was measured by Alphastep profilometer. The films were grown in vacuum at a base pressure of $1x10^{-5}$T, with a fluence of around 2.2 J/cm^2 at a substrate- target distance of 3 cm. After growth, all these samples were annealed for 30 minutes at their respective growth temperatures. The XRD peak positions, FWHM and conductivity corresponding to these growths have been summarized in Table 3.2.

The XRD scans of these samples have been presented in the Figure 3.6 (a). From the figure, the MoS_2 (002) peak can be clearly observed in the samples grown at temperatures ranging from 450^{0}C to 850^{0}C. From 450^{0}C to 850^{0}C, the peak position shifts from 13.04^{0} to 13.92^{0}, which shifts closer to the expected position of (002) orientation of MoS_2 of 14.17^{0} according to JCPDS card No. 37-1492 [82]. The full width at half maximum (FWHM) of the peak also decreases from 2.50^{0} to 1.22^{0} with increase in growth temperatures from 450^{0}C to 850^{0}C as shown in Table 3.2.

This implies that as the temperature of growth increases, the crystallinity of the thin film improves, as seen from the peak position shifting and the reduction in FWHM. It is also observed that the conductivity measured from the four point probe increases from 17.45 S/m to 381.68 S/m with an increase in growth temperatures from 700^{0}C to 850^{0}C, as seen from Table 3.2.

A second trend in XRD was also plotted for 60 nm thick samples grown at a

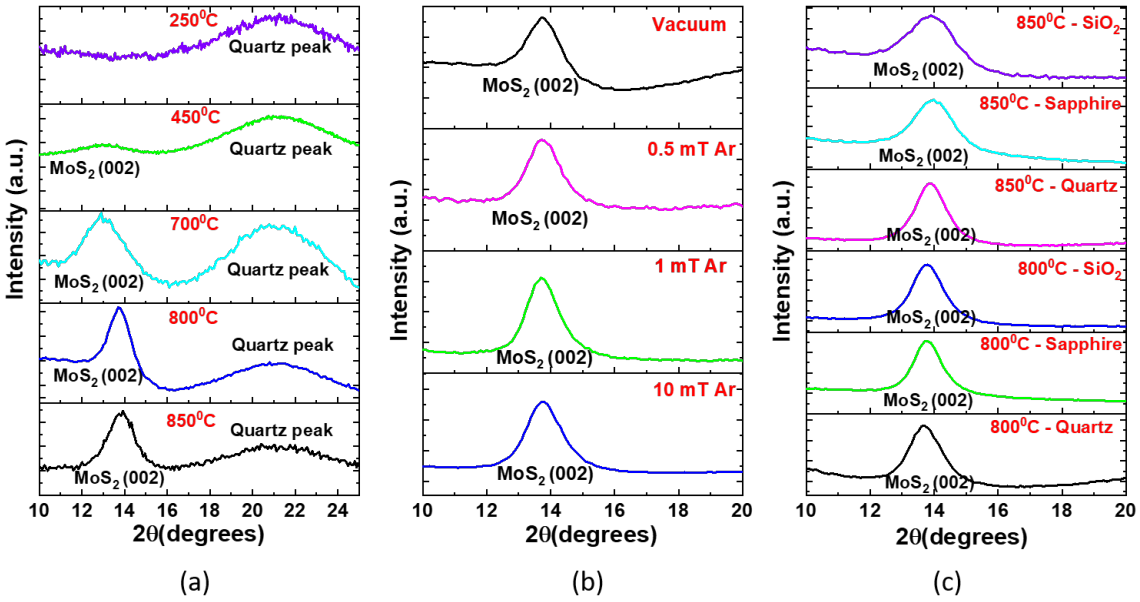

Figure 3.5: XRD plots of samples grown (a) at different temperatures, (b) with different gas ambient pressures and (c) on different substrates

fixed temperature of 800^0C on quartz in different ambient conditions within the chamber as shown in Figure 3.3 (b). The films were grown with a fluence of 2.2 J/cm^2 at a substrate- target distance of 3 cm. After growth, all these samples were annealed for 30 minutes in vacuum at 800^0C. Ar, an inert gas, was used to minimize impurities in the film during growth, along with reducing MoO_3 formation by oxidation in the chamber. Samples were grown in vacuum and at different Ar gas pressures ranging from 0.5 mTorr, 1 mTorr and 10 mTorr. It was observed that while the XRD peak position stayed around 13.8^0, the FWHM of the peak reduced from 1.32^0 to 1.07^0 as the gas ambient pressure reduced from 10 mTorr to 0.5 mTorr, however, the FWHM increases sharply for the sample set grown in vacuum to 1.29^0. This suggests that some amounts of inert ambient gas like Argon would help improve the crystallinity by minimizing the oxide formation. However, too much of the gas could reduce the energy of the plume particles moving towards the substrate, thereby reducing the quality of the thin films. This trend in film crystallinity matched with the conductivity measurements as well, as the four point measurements showed the same trend as observed as that from the XRD. Conductivity improved from 574.71 S/m to 4166.67 S/m from samples grown at 10 mTorr

to 0.5 mTorr of Ar. The sample grown in vacuum had a conductivity of 348.43 S/m.

A third comparison was performed between samples grown at 800 ^{0}C and 850 ^{0}C on three different substrates, namely, quartz, SiO_2/Si and c-axis oriented Al_2O_3 (sapphire). The films were grown with a fluence of 2.2 J/cm^2, ambient gas pressure of 0.5 mTorr of Ar and at a substrate- target distance of 3 cm. After growth, all these samples were annealed for 30 minutes in vacuum at the growth temperature.

The peak position of the samples grown at 800^{0}C ranged around 13.8^0 and those grown at 850^{0}C ranged around 13.9^0. For the samples grown at 800 ^{0}C, the lowest FWHM of 0.95^0 was obtained for sapphire, followed by 1.06^0 obtained for SiO_2/Si and 1.07^0 obtained for quartz. Among the samples grown at 850 ^{0}C, the lowest FWHM was again, obtained for sapphire at 1.11^0, followed by 1.15^0 obtained for quartz and 1.61^0 obtained for SiO_2/Si. A lower FWHM implies a higher crystallinity, and so in general, samples grown at 800$_0$C exhibited higher crystallinity. Among the three substrates, thin films grown on sapphire exhibited the highest crystallinity. This was expected due to the (001) orientation of the sapphire substrates. However, there wasn't a significantly drastic difference between these FWHM values or peak positions for these three substrates, indicating that the thin films may be growing fairly independent of the substrate at these growth conditions.

Conductivity for quartz was the highest among the three substrates for both temperatures as measured by the four point probe in Table 3.2, with values of 4166.67 S/m and 1851.85 S/m obtained for growth temperatures of 800^{0}C and 850 ^{0}C respectively. The other two samples grown at 850 ^{0}C had conductivities of 294.12 S/m for SiO_2/Si and 1612.90 S/m for sapphire substrates. Their counterparts grown at 800 ^{0}C showed conductivities of 469.48 S/m and 2857.14 S/m for SiO_2/Si and sapphire substrates respectively. Here, a higher conductivity in general was observed for samples grown at 800^{0}C when compared to those grown at 850 ^{0}C, suggesting better electrical properties at 800 ^{0}C growths. The higher conductivity of samples grown on quartz when compared to those grown on sapphire despite the latter possessing higher crystallinity suggests the presence of semimetallic 1-T phase of MoS_2 which can be verified using XPS to study the elemental states of

the compound.

A summary of the growth conditions of the thin films grown for these studies have been listed in the Table 3.1. A summary of the material properties, namely, the XRD 2θ peak position, Full width at half maximum (FWHM) of the peak, RMS roughness of the sample surface and the conductivity of the sample measured using a 4 point probe which have all been measured for the samples described in Table 3.1 has been presented in Table 3.2.

The samples have been named according to the format as mentioned in Appendix A.

Sample	**Substrate**	**Substrate temperature (^{0}C)**	**Ambient conditions**	**Thickness (nm)**
3L700CV-Quartz	Quartz	700	Vacuum	2
3L700CV-SiO_2/Si	SiO_2/Si	700	Vacuum	2
3L800C-0.5-Quartz	Quartz	800	0.5 mTorr Ar	2
3L800C-0.5-SiO_2/Si	SiO_2/Si	800	0.5 mTorr Ar	2
5L800C0.5-Quartz	Quartz	800	0.5 mTorr Ar	3
5L800C0.5-SiO_2/Si	SiO_2/Si	800	0.5 mTorr Ar	3
8L800C0.5-Quartz	Quartz	800	0.5 mTorr Ar	5.7
8L800C0.5-SiO_2/Si	SiO_2/Si	800	0.5 mTorr Ar	5.7
13L800C0.5-Quartz	Quartz	800	0.5 mTorr Ar	9.5
13L800C0.5-SiO_2/Si	SiO_2/Si	800	0.5 mTorr Ar	9.5
20L800C0.5-Quartz	Quartz	800	0.5 mTorr Ar	14
20L800C0.5-SiO_2/Si	SiO_2/Si	800	0.5 mTorr Ar	14
27L800C0.5-Quartz	Quartz	800	0.5 mTorr Ar	19
27L800C0.5-SiO_2/Si	SiO_2/Si	800	0.5 mTorr Ar	19
27L800C0.5-Si	Si	800	0.5 mTorr Ar	19
92L450CV-Quartz	Quartz	450	Vacuum	60
92L450CV-SiO_2/Si	SiO_2/Si	450	Vacuum	60
92L700CV-Quartz	Quartz	700	Vacuum	60
92L700CV-SiO_2/Si	SiO_2/Si	700	Vacuum	60
92L800CV-Quartz	Quartz	800	Vacuum	60
92L800CV-SiO_2/Si	SiO_2/Si	800	Vacuum	60
92L850CV-Quartz	Quartz	850	Vacuum	60
92L850CV-SiO_2/Si	SiO_2/Si	850	Vacuum	60
92L800C10-Quartz	Quartz	800	10 mTorr Ar	60
92L800C1-Quartz	Quartz	800	1 mTorr Ar	60
92L800C0.5-Quartz	Quartz	800	0.5 mTorr Ar	60
92L800C0.5-SiO_2/Si	SiO_2/Si	800	0.5 mTorr Ar	60
92L800C0.5-Al_2O_3	Sapphire	800	0.5 mTorr Ar	60
92L850C0.5-Quartz	Q	850	0.5 mTorr Ar	60
92L850C0.5-SiO_2/Si	SiO_2/Si	850	0.5 mTorr Ar	60
92L850C0.5-Al_2O_3	Sapphire	850	0.5 mTorr Ar	60

Table 3.1: Growth parameters of thin films analyzed by XRD, XPS, AFM, Raman spectroscopy, UV-ViS optical transmission, four point probe measurements and Hall measurements studies to measure material, optical and electrical properties of the thin films

Sample	**2θ peak position(^{0})**	**FWHM of peak(^{0})**	**RMS roughness (nm)**	**Conductivity (S/m)**
92L450CV-Quartz	13.04	2.50	0.48	-
92L700CV-Quartz	13.08	1.89	1.50	17.45
92L800CV-Quartz	13.81	1.29	1.07	348.43
92L850CV-Quartz	13.92	1.22	0.69	381.68
92L800C10-Quartz	13.80	1.32	>1.50	574.71
92L800C1-Quartz	13.75	1.13	>1.50	2702.70
92L800C0.5-Quartz	13.80	1.07	0.75	4166.67
92L800C0.5-SiO_2/Si	13.81	1.06	1.07	469.48
92L800C0.5-Al_2O_3	13.82	0.95	0.84	2857.14
92L850C0.5-Quartz	13.90	1.15	>1.50	1851.85
92L850C0.5-SiO_2/Si	13.90	1.61	>1.50	294.12
92L850C0.5-Al_2O_3	13.91	1.11	>1.50	1612.90

Table 3.2: Material properties including XRD peak position, XRD FWHM, RMS roughness of thin film and conductivity as analyzed for the samples stated in Table 3.1

From the observed XRD and 4 point measurements, It was observed that among the temperatures of 450^0C, 700^0C, 800^0C and 850^0C, 800^0C or 850^0C were growth temperatures that gave reasonably high crystallinity and conductivity. Between Ar gas pressures of 0.5 mTorr to 10 mTorr, a pressure of 0.5 mTorr showed the highest conductivity as well as crystallinity. Among the different substrates of quartz, sapphire and SiO_2/Si studied at 800^0C and 850^0C, samples grown at 800^0C in general, exhibited the highest crystallinity and conductivity. Therefore, to optimize future growths for the highest crystallinity and conductivity, based on these studies, it was thought to maintain a growth temperature of 800^0C in a gas ambient of 0.5 mTorr of Ar with a laser fluence of 2.2 J/cm^2. The substrate- target distance was varied from 3 to 5 cm, with higher distances employed for thinner growths. This was due to the cosine variation of the plume, and therefore, the growth rate would be lowered as it is proportional to the squared inverse of the distance. This would allow for a lower growth rate for a more precise thickness control. A table with the optimized conditions of growth has been presented in Table 3.3.

PLD Parameters	Optimized conditions—
Laser fluence	2.2 J/cm^2
Target-substrate distance	5 cm
Substrate temperature	800^{0}C
Post growth anneal	30 min at 800^{0}C
Ambient conditions of growth	0.5 mTorr Ar

Table 3.3: Optimized growth conditions for future PLD growths of MoS_2 samples

3.3 X-Ray photoelectron spectroscopy studies

Room-temperature XPS experiments were performed at nanoFAB using Kratos Axis spectrometer which was calibrated by the binding energy (84.0 eV) of Au 4f $^{7/2}$ with reference to Fermi level. The analysis chamber had ultra high vacuum within the chamber with a pressure of around 5x10^{-10} Torr. Charge effects were corrected by using C 1s peak at 284.8 eV. Thin films grown at 800^{0}C on quartz (with thickness of 60 nm), 800^{0}C on sapphire (with thickness of 60 nm), 800^{0}C on silicon (with thickness of 19 nm) and 850^{0}C on quartz (with thickness of 60 nm) with a 30 min post growth anneal at the growth temperature were analyzed using XPS to study the elemental states and the composition of the thin films deposited. The films were grown with a fluence of 2.2 J/cm^2, ambient gas pressure of 0.5 mTorr of Ar and at a substrate- target distance of 3 cm.

For the thin films grown at 800^{0}C on sapphire, it can be observed that prominent 2H Mo^{4+} $3d^{5/2}$ and $3d^{3/2}$ peaks at 229.82 and 233.02 eV respectively are present, which can be correlated very closely with the values present in literature [83; 84]. 2H Mo^{6+} peaks were observed at 233.72 and 236.32 eV corresponding to the states $3d^{5/2}$ and $3d^{3/2}$ respectively, as shown in the Figure 3.6 (a). The peak at 226.17 eV in the figure corresponds to the 1s state of sulfur. The $2p^{1/2}$ and $2p^{3/2}$ peaks of sulphur can be found at 163.70 and 162.55 eV as seen in Figure 3.6 (b). The states of Mo^{4+} correspond to MoS_2 formation while the states of Mo^{6+} correspond to MoO_3 formation in the thin film. The ratio of Mo^{4+} to Mo^{6+} was taken as the ratio of the percentage area obtained for the peak for the fitting performed on the CasaXPS software. In this sample, the ratio was nearly 3.7:1, which indicates a significantly high amount of MoS_2 present as compared to MoO_3. The XPS plots obtained for S and Mo are shown in Figure 3.6.

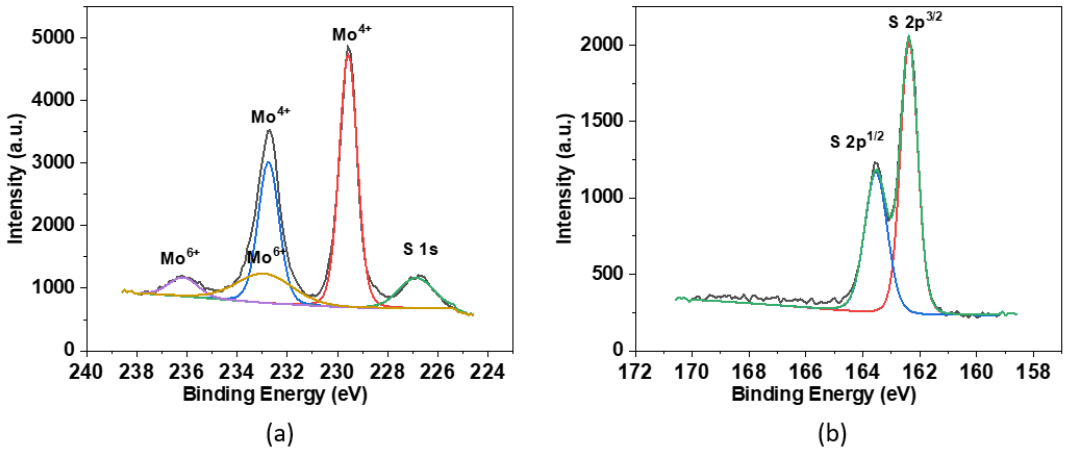

Figure 3.6: XPS spectra of (a) Mo (showing 2H Mo^{4+}, 2H Mo^{6+} and 1s S states) and (b) S (showing 2p states) for MoS_2 grown on sapphire at 800^0C

In the sample grown at 800^0C on quartz, from Figure 3.7 (a), 2H Mo^{4+} $3d^{5/2}$ and $3d^{3/2}$ (at 229.32 and 232.52 eV respectively) peaks and 1T Mo^{4+} $3d^{5/2}$ and $3d^{3/2}$ (at 227.92 and 231.03 eV respectively) peaks of Mo^{4+} were observed. 2H Mo^{6+} $3d^{5/2}$ and $3d^{3/2}$ (peak positions at 233.05 and 235.84 eV respectively) states were obtained, as shown in figure 3.7[84]. This sample clearly shows the presence of 1T semimetallic phase of Mo4+ along with semiconducting 2H Mo4+ phase. The ratio of 2H to 1T phase of Mo^{4+} was found to be 5.2:1, indicating a relatively small amount of 1T MoS_2 present in the sample. Here, the ratio of MoS_2 (2H and 1T phases) to MoO_3 was obtained to be around 7.8:1, which implies that the composition of the film is mainly that of MoS_2. The presence of semimetallic 1T phase of MoS_2 could explain the higher conductivity of the quartz samples over sapphire samples despite the sapphire samples having a higher crystallinity as seen from the XRD and conductivity studies in the previous section. The $2p^{1/2}$ and $2p^{3/2}$ peaks of sulphur can be found at 163.55 and 162.43 eV in Figure 3.7 (b), which also matches literature.

In the sample grown at 800^0C on Si, from Figure 3.8 (a), both 2H Mo^{4+} $3d^{5/2}$ and $3d^{3/2}$ (at 229.35 and 232.71 eV respectively) peaks were observed, along with prominent peaks for 2H Mo^{6+} $3d^{5/2}$ and $3d^{3/2}$ (at 230.57 and 235.85 eV respec-

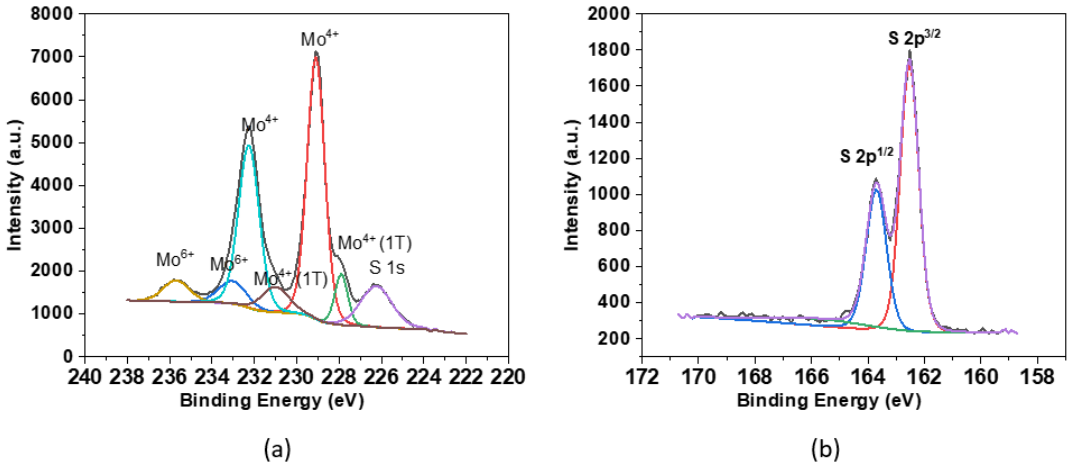

Figure 3.7: XPS spectra of (a) Mo (showing 2H Mo^{4+}, 1T Mo^{4+}, 2H Mo^{6+} and 1s S states) and (b) S (showing 2p states) for MoS_2 grown on quartz at 800^0C

tively) peaks as shown in the figure [84]. There is a slight shift in the peak position of the 2H $3d^{5/2}$ Mo^{6+} from around 232.5 eV to around 230.57 eV when compared with literature [85]. In this sample, the ratio of 2H MoS_2 to MoO_3 is around 1.8:1, which implies a significantly high presence of MoO_3 in the thin film when compared to the previous two samples. The $2p^{1/2}$ and $2p^{3/2}$ peaks of sulphur can be found at 163.38 and 162.13 eV in Figure 3.8 (b), which matches literature, however, satellite peaks at 165.46 and 168.04 eV along with a tilt of the XPS spectra suggests the presence of impurities in the thin film grown. It is possible that the tilt in the spectra could be formed due to these films being much thinner (19 nm compared to 60 nm) when compared to other films tested using XPS.

850^0C grown MoS_2 on quartz had a much higher amount of MoO_3 as compared to MoS_2 when compared to the sample grown on quartz at 800^0C. The Mo^{4+} $3d^{5/2}$ and $3d^{3/2}$ peaks are present at 229.64 and 232.97 eV respectively and Mo^{6+} $3d^{5/2}$ and $3d^{3/2}$ peaks are present at 232.74 and 236.15 eV respectively. Here, a large amount of Mo^{6+} is observed, with a ratio of 2.25:1 for MoS_2: MoO_3. This indicates that at a higher temperature, more MoO_3 may have formed due to the presence of a larger amount of energy because of the higher temperature of growth. This can be observed in the plots below in Figure 3.9 (a). Figure 3.9 (b) shows the presence of $2p^{1/2}$ and $2p^{3/2}$ peaks of sulphur at 163.44 and 162.29 eV in Figure 3.9(b), which matches literature.

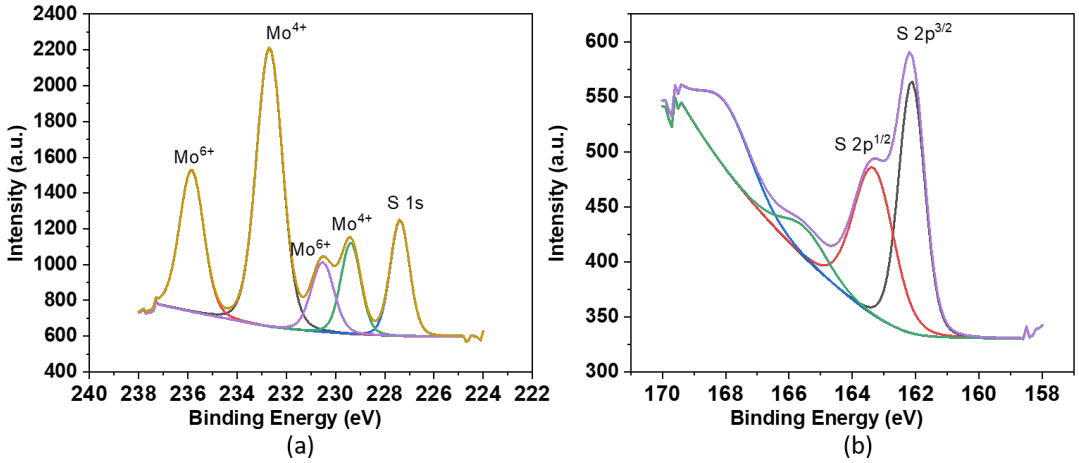

Figure 3.8: XPS spectra of (a) Mo (showing 2H Mo^{4+}, 2H Mo^{6+} and 1s S states) and (b) S (showing 2p states) for MoS_2 grown on silicon at 800^0C

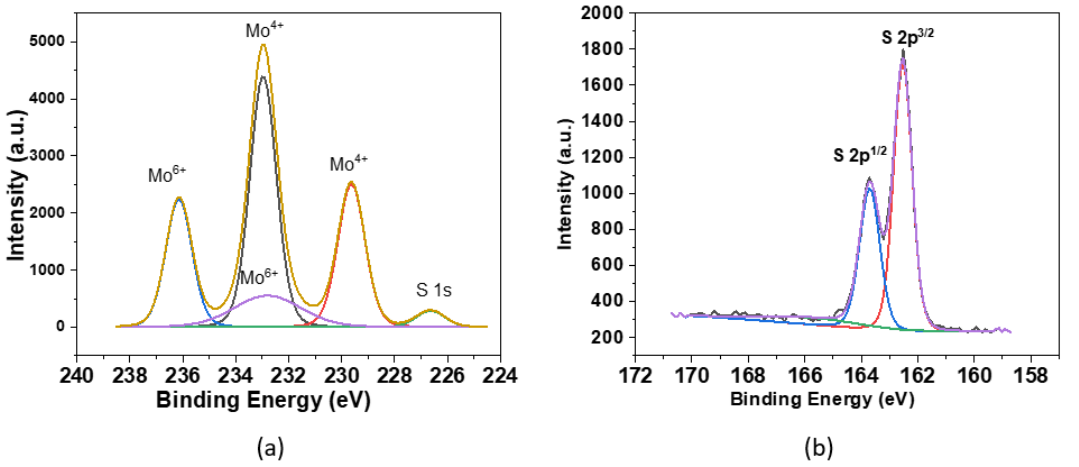

Figure 3.9: XPS spectra of(a) Mo (showing 2H Mo^{4+}, 2H Mo^{6+} and 1s S states) and (b) S (showing 2p states) for MoS_2 grown on quartz at 850^0C

A summary of the peak positions, elemental states and the ratio of Mo^{4+} to Mo^{6+}, which corresponds to the ratio of MoS_2: MoO_3 can be observed below in Table 3.4. From the table, it can be observed that growths on quartz and sapphire at 800^0C (samples 92L800C0.5-Quartz and 92L800C0.5-Al_2O_3) show the least amount of oxide formation in the films, compared to those grown at 800^0C on Si and 850^0C on quartz. 800^0C growth at sapphire showed a single phase of MoS_2 whereas that

grown on quartz showed both 2H and 1T phases of MoS_2. Due to the 850^0C growth forming more oxides than those at 800^0C, 800^0C was considered optimum for future growths.

Sample	**Elemental states present**	**Peak position (eV)**	**Ratio of Mo^{4+} to Mo^{6+}**
92L800C0.5-Al_2O_3	2H Mo^{4+} 2H Mo^{6+}	229.82 ($3d^{5/2}$) and 233.02 ($3d^{3/2}$) 233.72 ($3d^{5/2}$) and 236.32 ($3d^{3/2}$)	3.7:1
92L800C0.5-Quartz	2H Mo^{4+} 1T Mo^{4+} 2H Mo^{6+}	229.32 ($3d^{5/2}$) and 232.52 ($3d^{3/2}$) 227.92 ($3d^{5/2}$) and 231.03 ($3d^{3/2}$) 233.05 ($3d^{5/2}$) and 235.84 ($3d^{3/2}$)	7.8: 1 (Ratio of 2H- Mo^{4+} to 1T- Mo^{4+}- 5.2: 1)
27L800C0.5-Si	2H Mo^{4+} 2H Mo^{6+}	229.35 ($3d^{5/2}$) and 232.71 ($3d^{3/2}$) 230.57 ($3d^{5/2}$) and 235.85 ($3d^{3/2}$)	1.8:1
92L850C0.5-Quartz	2H Mo^{4+} 2H Mo^{6+}	229.64 ($3d^{5/2}$) and 233.97 ($3d^{3/2}$) 232.74 ($3d^{5/2}$) and 236.15 ($3d^{3/2}$)	2.25:1

Table 3.4: Table of extracted elemental states of Mo present in the samples measured by XPS with peak positions corresponding to the elemental states and ratio of MoS_2 to MoO_3

3.4 Atomic force Microscopy and Helium Ion Microscopy studies

Atomic force microscopy (AFM) was performed by Bruker Dimension Edge tool over a 1 µm area surface to study surface morphology and RMS roughness. Atomic force microscopy was first performed on around 60 nm thick thin films grown on SiO_2/Si at a fluence of around 2.2 J/cm^2, ambient gas pressure of 0.5 mTorr of Ar and at a substrate- target distance of 3 cm at different substrate temperatures, namely 450^0C, 700^0, 800^0C and 850^0C (samples 92L450C-0.5-SiO_2/Si, 92L700C-0.5-SiO_2/Si, 92L800C-0.5-SiO_2/Si and 92L850C-0.5-SiO_2/Si) with a 30 min post growth anneal at the growth temperature to study the effect of substrate temperature on surface morphology and RMS roughness.

AFM images of the 60 nm thick MoS_2 thin film samples (with around 92 L) grown were imaged using AFM as seen below in Figure 3.10.

Here, the RMS roughness of the grains of the sample grown at 450^0C was around 1.23 nm with an average particle diameter of 38.12 nm with a large standard devi-

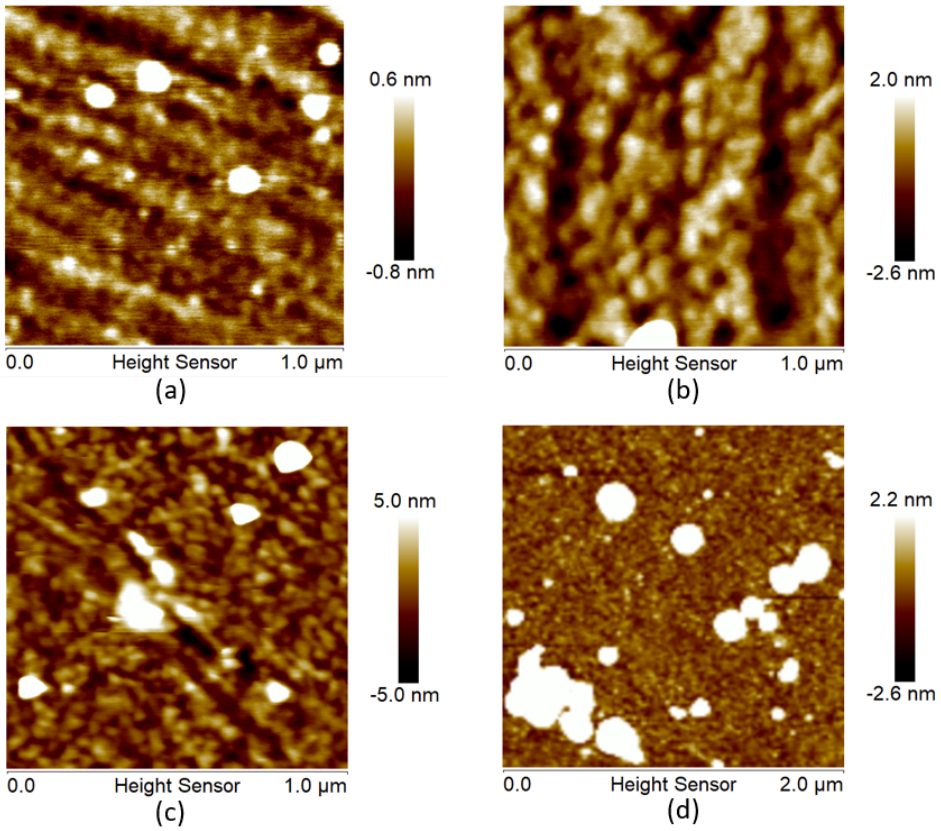

Figure 3.10: AFM scans of 60 nm thin films grown at a fluence of around 2.2 J/cm^2, ambient gas pressure of 0.5 mTorr of Ar and at a substrate- target distance of 3 cm at substrate temperatures of (a) 450^{0}C (RMS roughness of 0.48 nm), (b) 700^{0}C, (c) 800^{0}C and (d) 850^{0}C with a 30 min post growth anneal at the growth temperature

ation of 31 nm. The large particulates observed were 107 nm in diameter. As the growth temperature was increased to 700^{0}C, an average RMS roughness of around 1.08 nm was observed for the grains, with an average particle size of 29.23 nm and a standard deviation of 22 nm. The large particulate observed in the figure was around 122 nm in diameter. For the sample grown at 800^{0}C, the RMS roughness of the grains was observed to be 0.75 nm with an average particle size of 25.82 nm and a standard deviation of 6.54 nm with particulates of size 102 nm. The sample grown at 850^{0}C showed an RMS roughness of 0.59 nm with an average particle size of 33.21 nm with standard deviation of 8.79 nm and large particulates of 220 nm diameters.

From these measurements, it can be observed that as the temperature of growth increases, there is an decrease in RMS roughness of the grains due to a higher energy being available for the particles to form the crystal grains. This can be correlated with the increase in crystallinity with growth temperature as observed in XRD studies. The grains formed are also more uniform with increase in growth temperature as seen from the decrease in standard deviation of particle sizes. Visually, it can be seen that the grain regions appear to be more well defined as the growth temperature increases from 450^0C to 850^0C. Between 800^0C and 850^0C growths, it can be observed that a higher number of particulates is observed in the 850^0C growths, possibly due to the higher energy of the adatoms at that temperature when compared to the growth at 800^0C. A summary of the measured properties along with the sample information has been presented in the Table 3.5.

Sample	**RMS roughness (nm)**	**Average particle size (nm)**	**Standard dev. of particle size (nm)**	**Size of largest particulates (nm)**
92L450C-0.5-SiO_2/Si	1.23	38.12	31	107
92L700C-0.5-SiO_2/Si	1.08	29.23	22	122
92L800C-0.5-SiO_2/Si	0.75	25.81	6.54	102
92L850C-0.5-SiO_2/Si	0.59	33.21	8.79	220

Table 3.5: Table of extracted properties from AFM scans of MoS_2 thin films grown at different substrate temperatures.

Due to this large variations in particulate sizes, it was difficult to image a clear morphology of the thin film samples, as the AFM tip was constantly being blunted by the sharp variations in particulate sizes. The large particulates may also have been formed as a result of the substrate target distance being 3 cm, which caused a larger growth rate and a higher possibility of debris and splashing occurring on the substrate. While all of these measurements were performed on samples with a thickness of approximately 60 nm, change in surface morphology and roughness over thicknesses lower than 60 nm was sought to be measured to study if the reduction in thickness would be able to reduce the RMS roughness of the thin film. An increase in substrate - target distance to 5 cm was also done to reduce the amount of particulates formed on the thin films.

Following the optimization of substrate temperature and and other growth parameters as established from the XRD, 4 point and XPS measurements, films with thicknesses lower than 60 nm was attempted to obtain monolayer level control

over the thin film growth. The films were all grown on SiO_2/Si substrates at 800^0C with a 30 min post growth anneal at the growth temperature at a fluence of around 2.2 J/cm^2, ambient gas pressure of 0.5 mTorr of Ar,and at a substrate-target distance of 5 cm in order to get a better control of the number of layers during deposition by a slower growth rate. Films of thicknesses of around 19 nm, 14 nm, 9 nm, 3 nm and 1.2 nm (samples 27L800C-0.5-SiO_2/Si, 20L800C-0.5-SiO_2/Si, 13L800C-0.5-SiO_2/Si, 5L800C-0.5-SiO_2/Si and 3L800C-0.5-SiO_2/Si) were measured and analyzed. They were compared with the AFM scan of the 60 nm thick thin film (sample 92L800C-0.5-SiO_2/Si) grown at a fluence of around 2.2 J/cm^2, ambient gas pressure of 0.5 mTorr of Ar and at a substrate- target distance of 3 cm at 800^0C with a 30 min post growth anneal at the growth temperature as shown in Figure 3.10 (c) and Figure 3.11 (a), to study the change in surface morphology and RMS roughness with thickness.

AFM images of samples with these six different thicknesses have been shown in Figure 3.12 (a) - (f). All the scans were performed over a scan area of 1 μm^2 in tapping mode AFM configuration.
A very clear trend of reduced RMS roughness and increasing uniformity was observed for samples with decreasing thickness. The AFM and HiM images shown in the Figure 3.11 and 3.12 denote a comparison of the samples grown with different thicknesses on SiO_2/Si substrate. This substrate was chosen despite a higher crystallinity obtained by samples grown on sapphire/quartz so as to enable comparison of the same sample on both AFM and HiM. This was due to the issue of a non conductive substrate such as quartz/ sapphire leading to severe charging when imaged by HiM, and thereby reducing image quality.

The highest RMS roughness of 0.75 nm was observed for the 60 nm thin film as stated earlier in Table 3.5. On performing particle analysis, it was observed that the mean diameter of the particles of this sample was around 26 nm with a variation of grain sizes from 11 to 60 nm and a standard deviation of 6.54 nm with a few 88-102 nm sized particulates. The height variation across the scan area was from 32.9 to 1.6 nm.

The 19 nm thin film showed a lower roughness, with an RMS roughness value of 0.47 nm. The mean diameter of the grains was around 24 nm with a variation

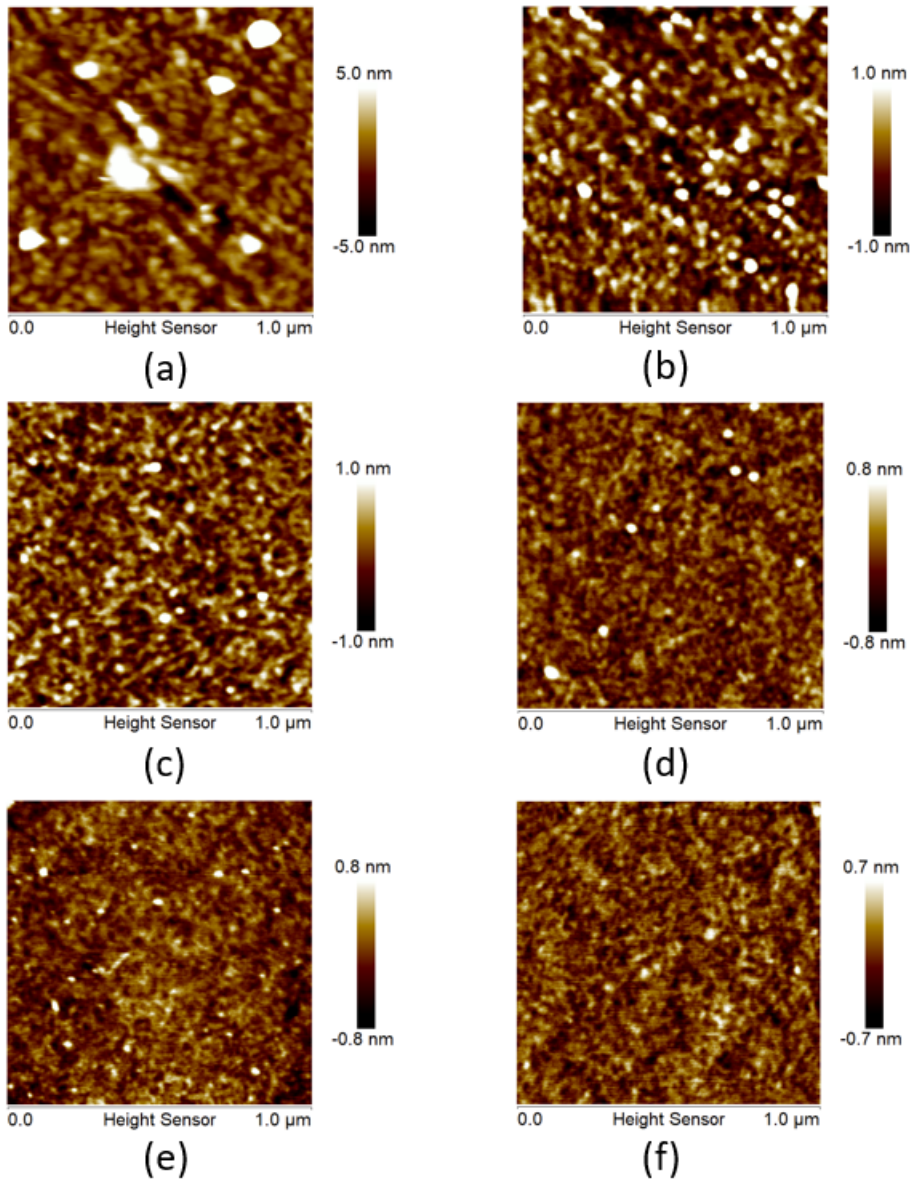

Figure 3.11: AFM scans of thin films grown at 800^0C with a 30 min post growth anneal at the growth temperature at a fluence of around 2.2 J/cm^2, ambient gas pressure of 0.5 mTorr of Ar at a substrate - target distance of (a) 3 cm and (b-f) 5 cm with thicknesses of (a) 60 nm (RMS roughness of 0.75 nm), (b) 19 nm (RMS roughness of 0.47 nm), (c) 14 nm (RMS roughness of 0.23 nm), (d) 9 nm (RMS roughness of 0.21 nm), (e) 3 nm (RMS roughness of 0.17 nm) and (f) 1.2nm (RMS roughness of 0.17 nm)

of 11 – 61 nm and a standard deviation of 7.21 nm. The height variation across the sample scan area was from 1.32 to 0.86 nm, which clearly shows a significant improvement in surface uniformity. There were also fewer particulate chunks observed on the surface. On scanning the 14 nm thin film, a further reduction in RMS roughness to 0.23 nm was observed. The mean diameter of the particles was 24 nm, like the previous case with a similar particle size variation between 11 and 64 nm and a standard deviation of 5.23 nm, but the height variation of the sample was even smaller with a range of 1.04 nm to 0.70 nm.

The 9 nm thin film had a surface RMS roughness of 0.21 nm with a similar range of particle size variation and height variation as that of the 14 nm thin film. The thinnest samples of 3 nm and 1.2 nm thickness were found to have a surface RMS roughness as low as around 0.17 nm. The mean diameter of the particles was found to be 18 nm with a range of sizes from 9 to 47 nm and a standard deviation of 4.89 nm. The uniformity of this sample was much higher, with a height variation between 0.60 nm to 0.38 nm.

A table with a summary of the variation of RMS roughness, average particle size and height variation corresponding to different thicknesses has been presented as Table 3.6.

Sample	**RMS roughness (nm)**	**Average particle size (nm)**	**Standard dev. of particle size (nm)**	**Height variation of particles (nm)**
92L800C-0.5-SiO_2/Si	0.75	26	6.54	32.9-1.6
27L800C-0.5-SiO_2/Si	0.47	24	7.21	1.3-0.9
20L800C-0.5-SiO_2/Si	0.23	24	5.23	1.0-0.7
13L800C-0.5-SiO_2/Si	0.21	24	5.25	1.0-0.7
5L800C-0.5-SiO_2/Si	0.17	18	4.89	0.6-0.4
3L800C-0.5-SiO_2/Si	0.17	18	4.89	0.6-0.4

Table 3.6: Table of extracted properties from AFM scans of MoS_2 thin films grown at different thicknesses.

The AFM measurements suggest that with increase in thickness of the films, there are more structural and surface defects, which, as the number of layers builds up, leads to surface strain and cracks that result in these surface irregularities. This can be observed especially clearly in the HiM images shown in Figure 3.12 for scans of samples of different thicknesses.

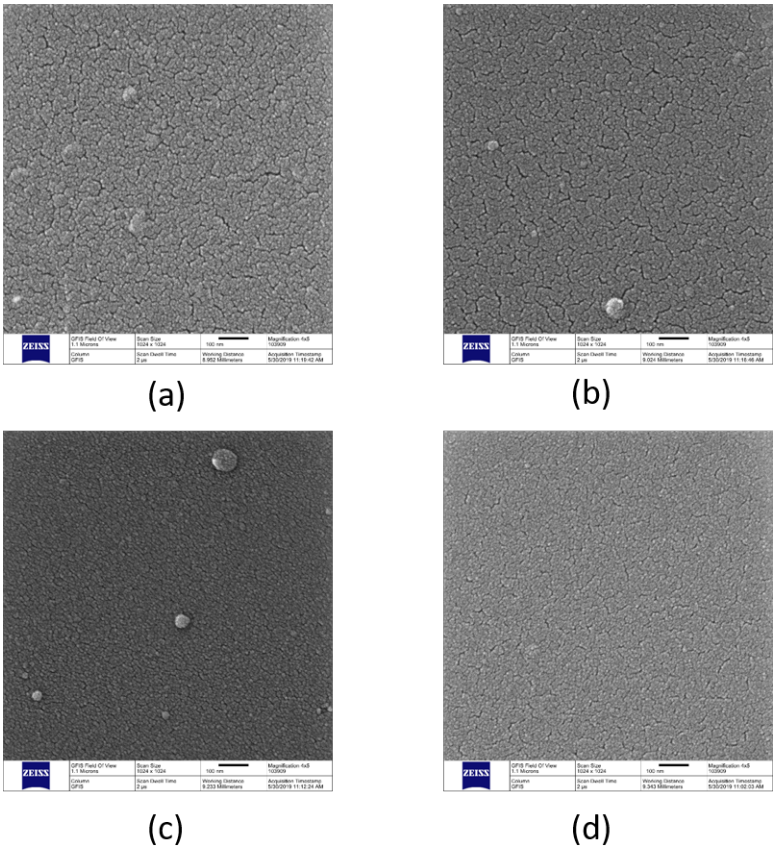

Figure 3.12: HiM images of thin films grown under optimized conditions with thicknesses of (a) 60 nm, (b) 19 nm, (c) 14 nm and (d) 3 nm

HiM imaging was performed on the samples presented in Figure 3.11 (a), (b), (c) and (e) (samples 92L800C-0.5-SiO_2/Si, 27L800C-0.5-SiO_2/Si, 20L800C-0.5-SiO_2/Si and 5L800C-0.5-SiO_2/Si) by the Zeiss Orion NanoFAB HiM tool with a magnification of 103909x and a scale bar at 100 nm as shown in Figure 3.12. A short dwell time of 2 μs was used to reduce the burning of the MoS_2 surface due to the focused He ion. The surface morphology of the thin films were able to be observed with a higher image resolution than those attempted by FESEM due to the scan being performed by helium ions, which can be focused on a smaller probe size with a smaller interaction volume along with enabling an increased rate of secondary electron generation. This improves the resolution of the image drastically at lower currents, therefore, enabling high resolution grain imaging of softer and thinner materials such as MoS_2.

On comparing the scan images of samples with different thicknesses, it can be

shown that the sample with around 60 nm thickness shows a larger number of particulate chunks over the surface, with prominent cracks and crevices noticed on the thin film structure. These cracks could be formed as a result of thin film strains developed with increased film thickness.

With increasing thickness of the samples from 3 nm to 60 nm, due to irregularities in the film, there were regions with varying thicknesses along with partially formed monolayers. As the thickness of the samples decreases, regions of stresses and cracks is observed to have reduced in area. The number of adatom clusters observed on the thin film surface also appear to be reducing with thickness, which also suggests an improved uniformity of the thin film with reduced film thickness. This observation suggests that for thin film applications where a uniform conductive MoS_2 thin film is required, a thickness of less than 20 nm would be suitable for improved performance due the lower RMS roughness, higher uniformity of grains and lower defects and film stresses as observed from the HiM and AFM experiments.

3.5 Transmission electron Microscopy studies

TEM was performed using JEOL JEM-ARM200CF S/TEM (Narwhal) to study the lattice structure of the MoS_2 thin film. A 5 nm thick SiN_x membrane was present at the center of a 3 mm sized Si substrate. MoS_2 was deposited on this substrate at a temperature of 800^0C and a gas ambient pressure of 0.5 mTorr of Ar with a fluence of 2.2 J/cm^2 and a post growth anneal of 30 minutes at the growth temperature. This allowed for a PLD grown MoS_2 thin film to be deposited by on the freely standing SiN_x membrane. The TEM image obtained for MoS_2 is shown in Figure 3.13 (a). At a scale bar of 5 nm, a hexagonal lattice structure with regulated bonds formed across the 2D plane can be clearly observed in the figure, demonstrating that a single crystalline epitaxial growth of MoS_2 has been achieved using PLD.

Figure 3.13 (b) presents the diffraction pattern of the area imaged in Figure 3.13 (a). At the center of the patterns, three distinctly connected hexagons can be

observed with varying intensities, indicating three distinct monolayers formed in the film. This diffraction pattern was converted to a dark field image to observe these 3 monolayers better. 3 monolayers of MoS_2 with consecutive layers rotated by around 60^0 when compared to each other can be observed from the Figure 3.13 (b) and (c). This suggests an ABA stacking formed in the PLD growths performed in this study.

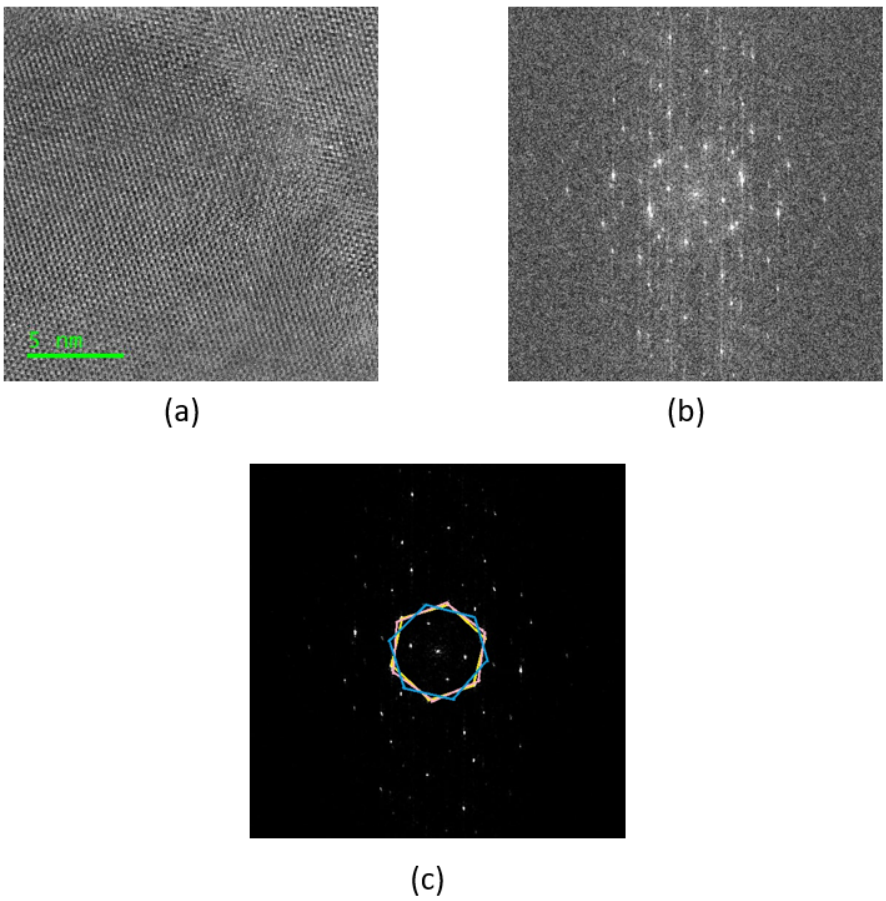

Figure 3.13: (a) TEM image of MoS_2 on SiN_x membrane, (b) diffractogram of MoS_2 and (c) estimation of the number of MoS_2 monolayers

From the thickness observed in the TEM diffraction patterns, the actual thicknesses of the other samples grown were estimated based on the growth time period, as all the other growth parameters were kept fairly constant during the growths. This was performed to obtain a more accurate measure of the thickness due to the possibility of inaccuracies due to the low resolution of the profilometry, which was

around 100 nm. The sample measured on the TEM was that of 3L800C-0.5-SiNx, on which 3 ML were estimated to have been formed as per diffraction patterns observed in Figure 3.13 (c). From this and from the number of pulses used for the growth, the growth rate was calculated to be around 0.0158 nm/pulse. This growth rate was used to estimate the thicknesses of the other samples in the table. The table with the estimated thicknesses of the thin films based on TEM results has been shown below in Table 3.7. These samples were used to for Hall measurements to estimate electronic properties such as electron mobility, resistivity and doping concentrations from Hall voltage and resistance measurements as explained in Chapter 4.

Sample	**Pulses**	**Estimated thickness from Profilometer**	**Number of MonoLayers estimated from TEM Diffraction**	**Thickness estimates based on TEM Diffraction patterns**
3L800C-0.5SiNx	120	3 nm	3 ML	1.9 nm
5L800C-0.5-SiO_2/Si	200	4 nm	5 ML	3.16 nm
8L800C-0.5-SiO_2/Si	360	7 nm	8 ML	5.68 nm
13L800C-0.5-SiO_2/Si	600	10 nm	13 ML	9.48 nm
20L800C-0.5-SiO_2/Si	900	15 nm	20 ML	14.22 nm
27L800C-0.5-SiO_2/Si	1200	20 nm	27 ML	18.96 nm
92L800C-0.5-SiO_2/Si	2400	60 nm	56 ML	37.92 nm

Table 3.7: Estimated thicknesses of the samples grown based on the thickness observed in the TEM diffraction patterns.

3.6 Optical characterization using Transmission studies and Raman

Raman spectroscopy was performed using Horiba XploRA ONE with an excitation wavelength of 532 nm and a grating of 1800 lines/mm to predict the approximate number of monolayers of the deposited films. Transmission and absorption studies have been performed using the Perkin Elmer UV Spectrophotometer over a range of 320 nm to 700 nm to observe the excitonic interactions in the thin films of different thicknesses.

Raman spectroscopy was performed on the thin films grown on quartz at 700^0 C with a post growth anneal period of 30 min at growth temperature (sample 3L700C-0.5-Quartz) and at 800^0 C with a post growth anneal period of 30 min at the growth temperature (samples5L800C-0.5-quartz and 13L800C-0.5-SiO_2/Si) at a substrate target distance of of 5 cm, a fluence of 2.2 J/cm^2 and a gas ambient of

0.5 mTorr of Ar during deposition with 120 shots, 200 shots and 600 shots of laser pulses for deposition.

MoS_2 has a unique property where the difference between the peak positions of the $E_{2G}{}^1$ and A_{1G} modes of vibrations vary with change in the number of monolayers, allowing us to estimate the number of layers in a particular sample by correlating this difference with the number of layers observed in literature. When the sample grown with 120 shots was measured, it was observed that a thickness of 2-3 monolayers of MoS_2 was expected according to a difference of 21.29/cm in the peak positions of the Raman spectra, which corresponds to literature [86; 87]. This matches closely with the number of monolayers obtained in the TEM diffraction patterns for a sample with 120 shots as seen in Figures 3.14 (b) and (c). 4-5 monolayers were observed for the sample grown with 200 shots with a difference in peak positions of 24.84/cm. Bulk MoS_2 thin films ($>$ 8 ML) was observed with 600 shots, as the difference between the peak positions was 26.62. The peak positions, and the differences in the peak positions for $E_{2G}{}^1$ and A_{1G} modes of vibrations for the three samples measured have been shown in Figure 3.15.

Transmission and absorption spectra of PLD grown thin films of different thicknesses were performed between the detector wavelength range of 300 nm to 700 nm on the U-Vis Hitachi Spectrophotometer. All of the thin films were grown on quartz at 800^0 C with a post growth anneal period of 30 min at the growth temperature at a substrate target distance of of 5 cm, a fluence of 2.2 J/cm^2 and a gas ambient of 0.5 mTorr of Ar during deposition. The samples studied include plain quartz, 3L800C-0.5-SiO_2/Si, 5L800C-0.5-SiO_2/Si, 8L800C-0.5-SiO_2/Si, 13L800C-0.5-SiO_2/Si, 27L800C-0.5-SiO_2/Si and 92L800C-0.5-SiO_2/Si.

In the transmission spectra over different thicknesses, it was observed that dips in intensity at wavelengths of around 620 nm and around 440 nm were present, which were also present in the absorption spectra as peak positions. The dip at 620 nm could correspond to the "B" excitonic transitions from the deep inner valence band to the conduction band. The dip at 440 nm could correspond to the "C" excitonic transition associated with van Hove singularities in multilayered MoS_2. These positions have also been observed in other PLD studies [86; 88; 89; 90].

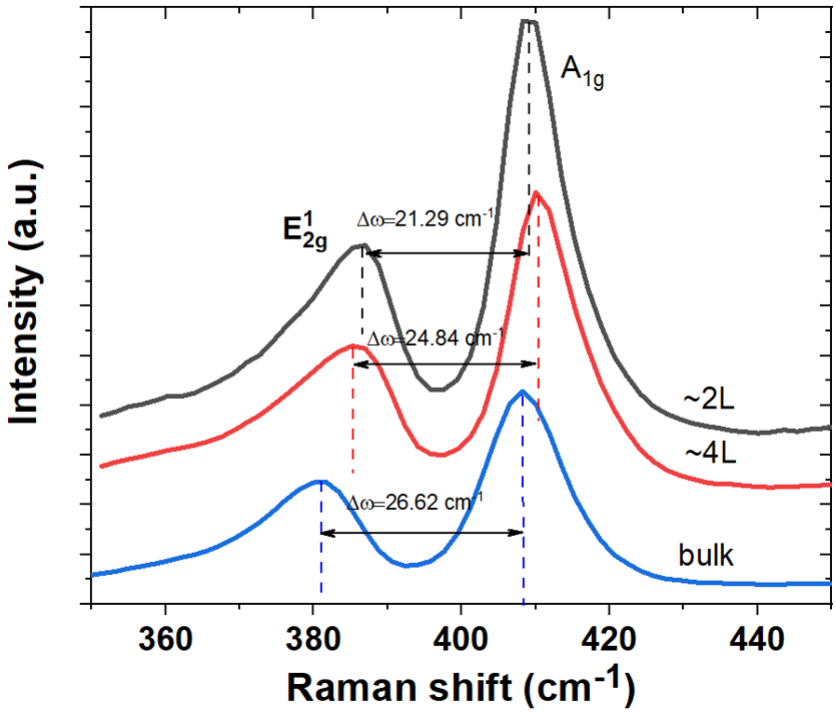

Figure 3.14: Raman peaks for $E_{2G}{}^1$ and A_{1G} modes of vibrations and peak differences for three different thicknesses of MoS_2 thin films, namely 2-3 ML (sample 3L700C-0.5-Quartz), 4-5 ML (sample 5L800C-0.5-quartz) and $>$ 8 ML (sample 13L800C-0.5-SiO_2/Si).

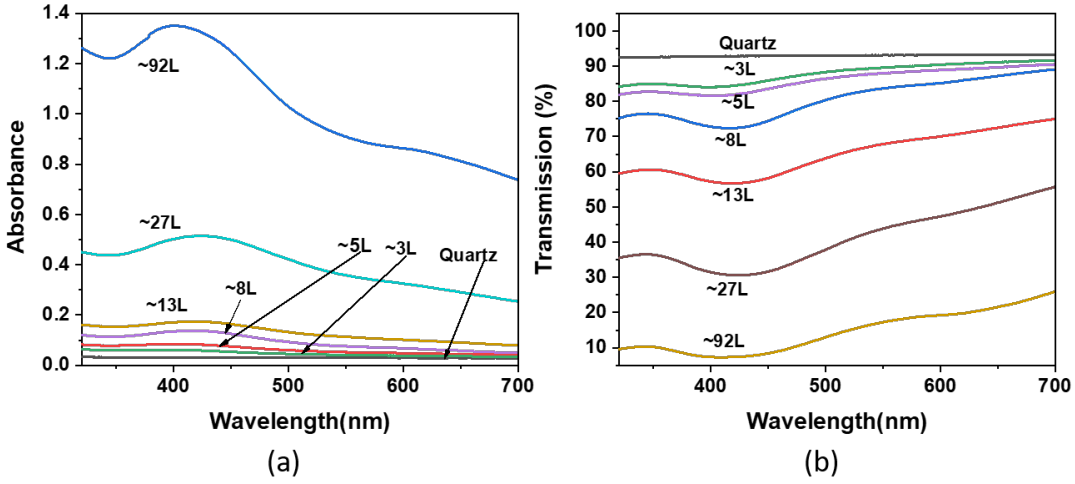

Figure 3.15: Transmission and absorption spectra of thin films with different thicknesses exhibiting characteristic B excitonic transitions at 620 nm and C excitonic transisitions at 440 nm.

3.7 Conclusions and Future Work

In this study, PLD of MoS_2 thin films was studied to understand the effects of different growth parameter conditions on the quality of the thin films. Films of a thickness of around 60 nm were initially grown and the crystallinity was examined by using XRD scanning and four point conductivity measurements to examine the film quality. XPS analysis was performed on the thin films grown on three different substrates (quartz, Si and sapphire) at two different temperatures (800^0C and 850^0C) to study the elemental states obtained at different conditions of growth.

Optimized growth conditions of 800^0C growth with a 30 min post growth anneal at the growth temperature at a fluence of 2.2 J/cm^2 with a substrate target distance of 5 cm under a 0.5 mTorr Ar ambient was fixed for growths of thinner films in an attempt to obtain a layer wise growth control. Film morphology, surface roughness and uniformity of the films varying with substrate temperature and film thickness were measured and studied using AFM and HiM imaging to observe that as the thickness reduced, the films were more uniform with lower surface roughness and fewer cracks imaged on the thin film. TEM imaging of the thin film grown on SiN_x membranes was performed to observe that the film was single crystalline with a hexagonal lattic and the diffraction patterns revealed that the sample had a 3 monolayer thickness. From the TEM, AFM and HiM imaging studies, Stranski-Krastanov (S-K) mode of thin film growth can be predicted for the growth of MoS_2. Raman spectroscopy was used to verify the number of monolayers in different MoS_2 thin film samples and optical transmission and absorption studies were used to observe the different excitonic peaks observed in thin films with different thicknesses.

Future work includes working towards obtaining monolayer thickness of film, and obtaining a more precise layer by layer control over the growth, which was not possible due to limited access to our PLD system owing to administrative issues. A study of variation of laser fluence would also be useful in obtaining a more precise control on the monolayer growth of MoS_2 by PLD. These films can also be grown in heterojunction designs with other 2D materials such as WS_2 and h-BN to study the properties of the junctions of PLD grown thin films and to explore the possibility of heterostructure devices. The PLD grown thin films can be used

to fabricate large area scalable MoS_2 based transistor devices and photodetectors. One of the major challenges with this is with etching of MoS_2 thin films. During HiM measurements, it was observed that With an increase in the time of exposure to He ions, monolayers of the film slowly etched in a layer by layer fashion as shown in Figure 3.16. This suggests the possibility of employing HiM for MoS_2 thin film etching applications for electronic device fabrication, by defining regions of the thin films to be exposed to He ions, and optimizing an etch rate depending on the time required to etch different thicknesses of the thin film.

Growth on flexible substrates can be performed to further study the dependence of substrate on film quality. Mechanical tests on these thin films grown on flexible substrates would help us understand the mechanical properties of the thin films grown by PLD, and these have a potential for integration in flexible and wearable sensors and devices.

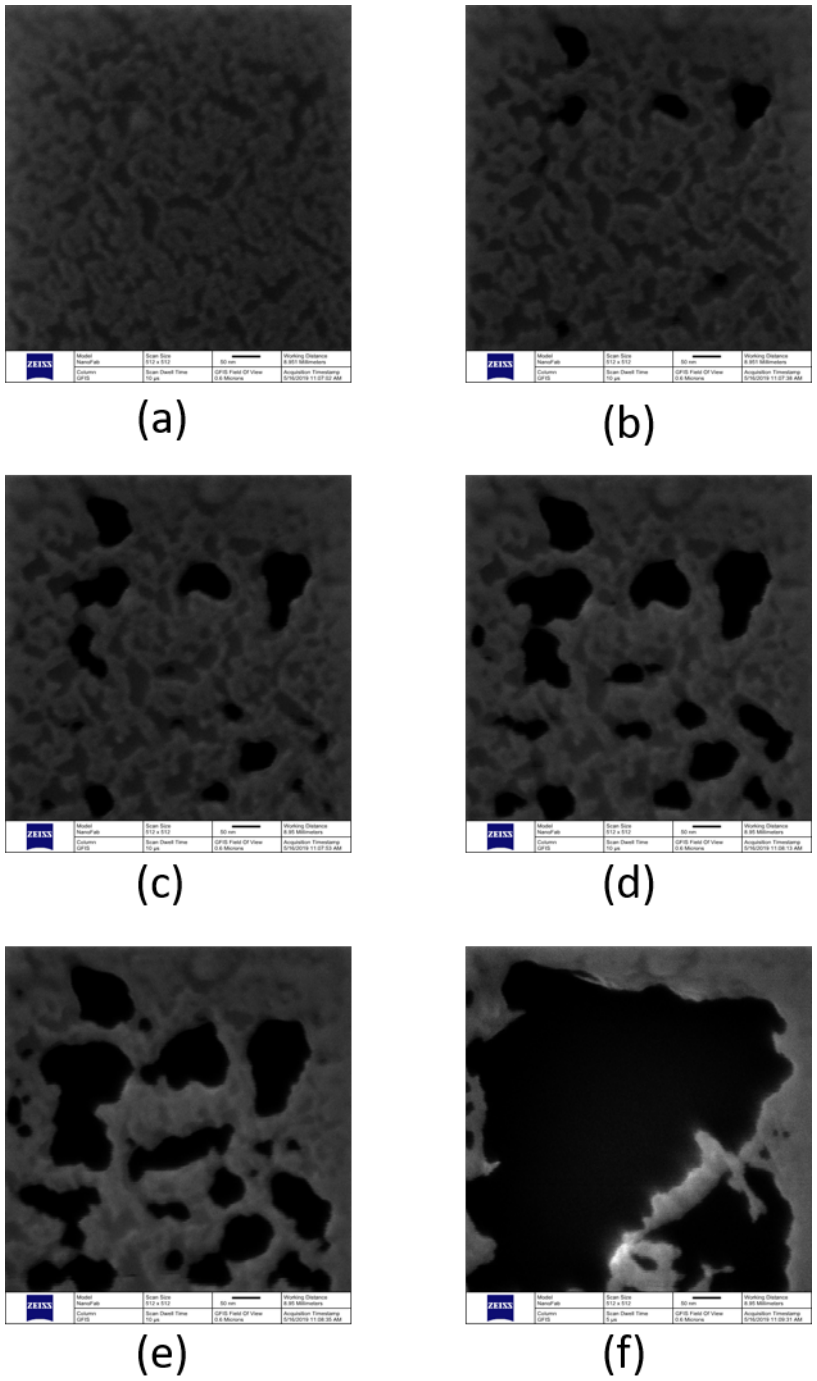

Figure 3.16: Flaking and etching of multilayer MoS_2 observed over time due to He ion exposure over figures (a) through (f)

Chapter 4

Hall Measurements and Mobility extraction of MoS_2 thin films

Mobility a very important electrical property which gives a measure of the extent to which free electrons or holes can move in a semiconductor thin film under the application of a potential bias, and therefore is a very important property to explore when thin films being considered for electronic device applications. It is also one property of MoS_2 specifically, that has not been explored much, due to novelty of the material and the limited understanding of transport phenomena and variation of electronic properties with the number of monolayers. Some of the mobility studies performed on MoS_2 and other 2D materials involve fabrication of 2D thin film transistors to measure mobility from the output and transfer characteristics of the transistors. These studies have recorded the n-type behavior of MoS_2, with electron mobilities of 1-200 cm^2/Vs for devices with 1-6 monolayers of MoS_2 [91; 59; 92; 93]. With an increase in the number of layers, an increase in mobility has been observed, which has been attributed to the screening of lattice phonon and coulombic scattering effects with increased thickness [94].

One established technique for obtaining the mobility of thin films has been the Van der Pauw technique, which is used to measure the hall voltage of an irregularly shaped thin film [95]. This has been a technique that has not been adopted for 2D materials so far, as mechanical exfoliation has been able to produce flakes of very small areas (typically $< 10\ \mu m^2$), which has been too small for these measurements.

In our study, we were able to deposit uniform MoS_2 thin films of around 100 mm^2, which makes it convenient for Van der Pauw experiments. This approach was an exciting study due to the fact that it had has not been explored for MoS_2 so far, and hence is a novel approach to the mobility extraction of 2D material thin films.

4.1 Measurement setup

Hall measurements for thin films are performed using a standard Van der Pauw method of Hall voltage measurements, which can be used for the measurement of Hall voltage of irregularly shaped thin films [79]. The ideal contacts for the thin films should be ohmic, and placed either in a clover leaf formation or a square formation as shown in the Figure 4.1.

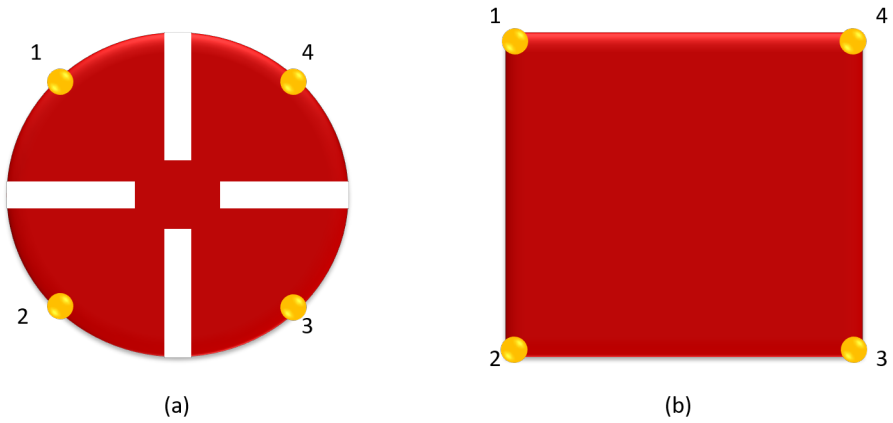

Figure 4.1: Schematic of contact placement for Van der Pauw measurement with (a) clover leaf structure and (b) square structure.

The Van der Pauw structure is used to measure the resistivity and the Hall voltage in a thin film with the contact placements as shown above. Here, the contacts are numbered in a counter clockwise manner as shown in the figure. For our measurements, the structure shown in Figure 4.1 (b) was adopted.
In order to measure resistivity, the individual contact resistances are measured by passing a current through two adjacent contacts (eg. contacts 1 and 2) and measuring the voltages across the other two contacts (contacts 3 and 4) and obtaining the resultant resistance as shown below.

$$R_{12,34} = \frac{V_{34}}{I_{12}} \tag{4.1}$$

Similarly, $R_{34,12}$, $R_{23,41}$ and $R_{41,23}$ are calculated to obtain the $R_{vertical}$ and $R_{horizontal}$ as shown below.

$$R_{horizontal} = \frac{R_{23,41} + R_{41,23}}{2} \tag{4.2}$$

$$R_{vertical} = \frac{R_{12,34} + R_{34,11}}{2} \tag{4.3}$$

The sheet resistance R_s is obtained from the equation below.

$$e^{\frac{-\pi R_{vertical}}{R_s}} + e^{\frac{-\pi R_{horizontal}}{R_s}} = 1 \tag{4.4}$$

This multiplied by the thickness 't' of the thin film gives the resistivity ρ of the thin film. This can be calculated as:

$$\rho = R_s * t \tag{4.5}$$

To calculate the Hall voltage, current is applied between two opposite contacts (1 and 3 or 2 and 4) in both directions (13, 31 and 24, 42) and the voltage is recorded between the other two opposite contacts for all of the cases. This is performed with both positive and negative magnetic fields.
The individual difference in voltages for both positive and negative magnetic fields are calculated for all 4 configurations of voltage measurements according to the equations below.

$$V_{13} = V_{13,P} - V_{13,N} \tag{4.6}$$

$$V_{31} = V_{31,P} - V_{31,N} \tag{4.7}$$

$$V_{24} = V_{24,P} - V_{24,N} \tag{4.8}$$

$$V_{42} = V_{42,P} - V_{42,N} \tag{4.9}$$

With the Hall voltage V_H being calculated according to the following equation.

$$V_H = \frac{V_{13} + V_{31} + V_{24} + V_{42}}{8} \tag{4.10}$$

From the Hall voltage and resistivity it is possible to calculate the hole or electron mobility (μ_{h} or μ_{e}) depending on the nature of the material (p or n type) and doping concentration (p or n) according to the following equations.

$$\mu_h = \frac{V_H t}{IB\rho} \tag{4.11}$$

$$\mu_e = \frac{V_H t}{IB\rho} \tag{4.12}$$

and

$$p = \frac{IB}{V_H te} \tag{4.13}$$

$$n = \frac{IB}{V_H te} \tag{4.14}$$

Where I is the value of current passed, B is value of magnetic field and e is the value of the charge of an electron or hole.

These calculations were used for the Hall measurement analysis of MoS_2 thin films discussed below.

In this study, MoS_2 thin films were grown by PLD on SiO_2/Si substrates. These were then cleaved to form around 5-7 mm x 5-7 mm squares, after which four symmetrical contacts were formed at the four corners of the sample by using either silver (Ag) or indium (In) paste or sputtered gold (Au). These four contacts were measured for Hall measurements to compute Hall voltage and resistances, and from them, resistivity, mobility and carrier concentrations were computed using the equations described above.

Lakeshore Model 642-electromagnet power supply and cryogenic chamber were used for the application of 0.1T of magnetic field normal to the thin film surface. The application of current and measurement of voltage at the contacts was performed by connecting Au wires stuck to the contacts with Ag paste. These were connected with the contacts (Ag or In paste, and Au) and lead to electrical clips that were then connected to a Keithley 2400 sourcemeter. The current was applied by the Keithley sourcemeter, and the voltage was measured by the Keithley and

a Picotest voltmeter.

The first set of measurements were performed, with Ag paste contacts attached to the thin films on the four corners, which were then pasted to the Au wires. This was dried and then affixed onto the substrate holder, and then placed inside the chamber for the application of a magnetic field normal to the thin film plane towards, and away from the thin film plane for the Hall measurements.

Due to the higher resistances observed with Ag paste contacts for samples with thickness lower than 14 nm, In paste contacts were attempted, which lead to non linear I-V currents as shown in Figure 4.2 (b). To enable a good ohmic contact with the MoS_2 films, 1-1.5 mm x 1-1.5 mm squares of Au was sputtered on the contact area using a shadow mask made from Kapton films using the planar magnetron sputtering system at NanoFAB. Ag paste was used to affix the Au wires for electrical connections to the Au contacts.

From Figure 4.2, the IV curves obtained when voltage was swept from -1 V to +1 V applied across contacts 1 and 3 (Figure 4.1), and the current was recorded between 2 and 4 and vice versa for three different types of contacts, namely, Ag paste, In paste, and sputtered gold affixed with Ag paste can be seen. In Figure 4.2 (a) it can be observed that a linear IV was obtained for Ag contacts used for sample 56L800C-0.5-SiO_2/Si. As the sample thickness went down to 9 nm, very low current values (<10 nA) were observed, indicating a high contact resistance. On using In contacts, non linear current was observed as shown in Figure 4.2 (b) for sample 20L800C-0.5-SiO_2/Si. To solve this problem, Au contacts were sputtered on the four corners of the sample with an area of approximately 1 mm^2 using a Kapton shadow mask. To these Au contacts, Ag paste was applied to connect it with the Au wires, which were then connected to the electrical measurement setup. The IV curves obtained for sample 13L800C-0.5-SiO_2/Si shows a linear symmetric behavior for the two sets of contacts as seen in Figure 4.2 (c).

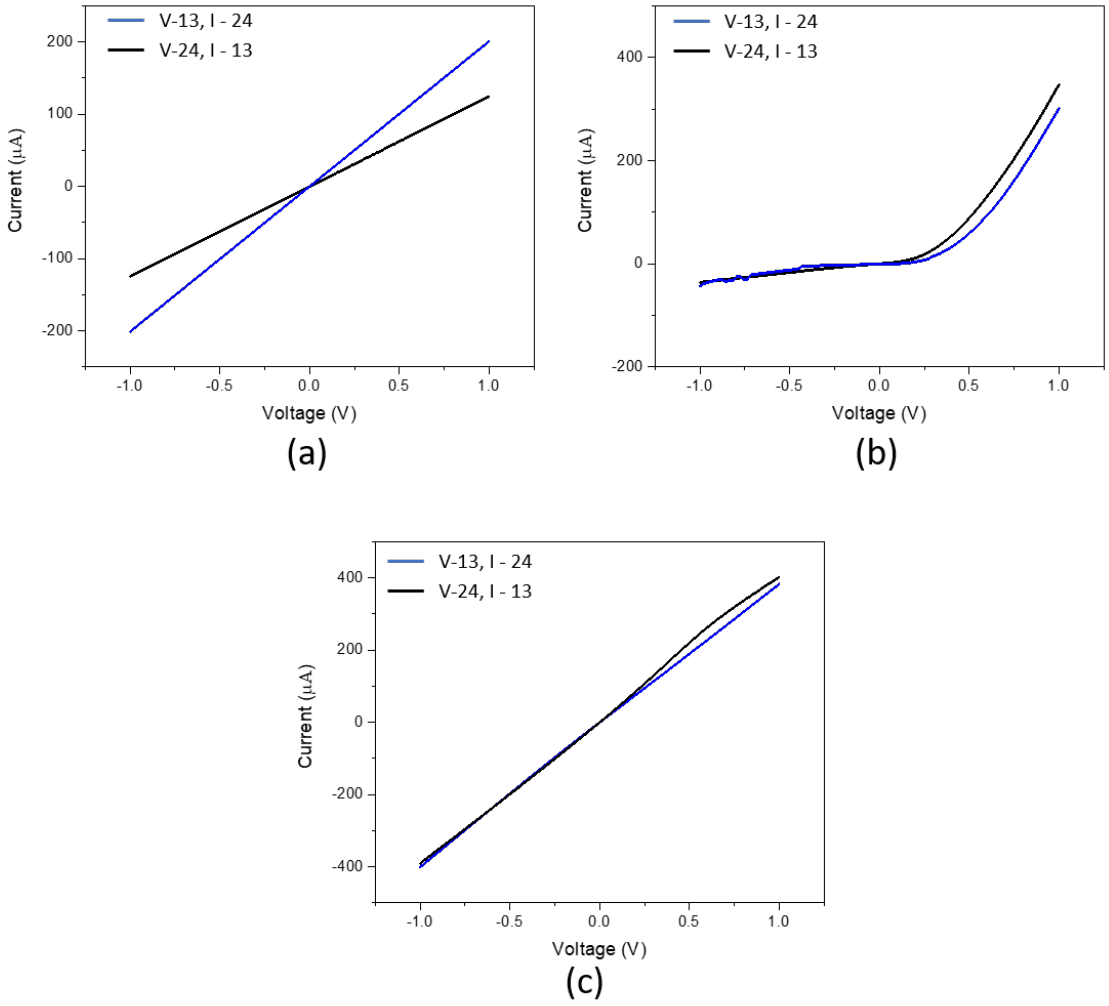

Figure 4.2: Examples of the IV plots obtained for measurements where the current was recorded between contacts 1 and 3 (Figure 4.1), and the voltage was swept between -1 V to +1 V across contacts 2 and 4, and vice versa with (a) Ag paste contacts for sample 56L800C-0.5-SiO_2/Si, (b) In paste contacts for sample 20L800C-0.5-SiO_2/Si and (c) sputtered Au contacts connected to Au wire with Ag paste for sample 13L800C-0.5-SiO_2/Si.

4.2 Hall Measurements with Ag and Au/Ag Contacts

Samples with Ag paste contacts were measured over three different samples with thicknesses of 38 nm, 19 nm and 14 nm were measured. All of the thin films were grown at 800^0 C with a post growth anneal period of 30 min at the growth temperature at a substrate target distance of of 5 cm, a fluence of 2.2 J/cm^2 and a gas ambient of 0.5 mT of Ar during deposition. These corresponded to the samples 56L800C-0.5-SiO_2/Si, 27L800C-0.5-SiO_2/Si and 20L800C-0.5-SiO_2/Si as seen in Table 4.1. A magnetic field of 0.1T was applied towards and away from the thin film surface, in a direction normal to the surface. This was performed over three measurements each with currents of 0.1 μA and 1 μA. Resistivity, electron mobility and doping concentration were calculated using the equations 4.1-4.12. These values have been listed in Table 4.1.

Samples thinner than 14 nm were not able to be measured using Ag contacts due to the higher contact resistances (with range of current changing from 10^{-4}A to 10^{-8}A) observed with thinner samples. Therefore, In and Au/Ag were tested. However, In contacts suffered with non linear I-V curves as seen in Figure 4.2 (b). This was due to the work function of In being 4.09 [96], which was much lower than that of MoS_2 which is in the range of 4.62 eV - 5.25 eV from literature [97; 98], thus forming a Schottky contact instead of an ohmic contact. Au/Ag contacts were explored since Au has a work function of 5.47 eV from literature [96]. These contacts were formed by using a shadow mask made by kapton films, and sputtering Au on the corner areas as described above in 1mm^2 areas. A magnetic field of 0.1 T was also applied here in directions towards and away, perpendicular to the plane of the thin film. This was performed over three measurements each with currents of 0.1 μA and 1 μA.

Au/Ag contacts worked better both in terms of being able to lower the contact resistance and enable ohmic contacts as seen fromn the linear I-V curves in Figure 4.2 (c). Some of the main advantages of using Au/Ag contacts was that the I-V curves remained linear even with sample thicknesses of <14 nm of MoS_2, implying an ohmic contact at different thicknesses measured. The samples measured were

56L800C-0.5-SiO_2/Si, 20L800C-0.5-SiO_2/Si, 13L800C-0.5-SiO_2/Si, 11L800C-0.5-SiO_2/Si, 8L800C-0.5-SiO_2/Si, 6L800C-0.5-SiO_2/Si and 5L800C-0.5-SiO_2/Si. These corresponded to thicknesses of around 38 nm, 14 nm, 9 nm, 7.5 nm, 5.6 nm, 4 nm and 3.5 nm respectively, as listed in Table 4.1. The resistivity, electron mobility and doping concentrations calculated from these measurements have also been listed in table 4.1.

Samples 13L800C-0.5-SiO_2/Si and 11L800C-0.5-SiO_2/Si were grown on 12 June, 2019 and samples 8L800C-0.5-SiO_2/Si and 6L800C-0.5-SiO_2/Si were grown on 13 June, 2019. Two samples each were taken from a 2.5 cm X 0.7 cm long SiO_2/Si substrate strip grown in each growth. This substrate was placed in such a way that the plume was centered at the spot shown in Figure 4.3. The first sample measured was assumed to be of the thickness estimated based on the number of shots. The second sample was taken at a point at around 1 cm away from the first sample, and therefore was assumed to have a thickness 25% lower than that of the first sample. This was estimated on the basis of the thickness variation observed during measurements with the profilometer, where a decrease of 25% was observed per cm. This was used for the estimation of the number of layers in sample 11L800C-0.5-SiO_2/Si grown on 12 June 2019 and sample 6L800C-0.5-SiO_2/Si grown on 12 June 2019. This was performed to obtain a few more samples to the dataset, as further samples were unable to be grown because of limited access to the PLD tool due to administrative issues.

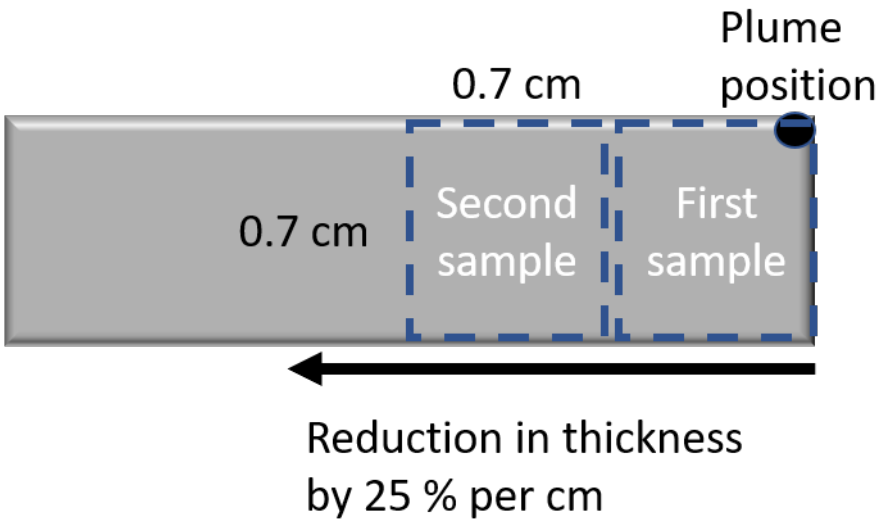

Figure 4.3: Schematic of plume location and thickness variation with distance from plume

4.3 Results and discussions

A summary of the results obtained through measurements and calculations is presented below in Table 4.1. Properties such as resistivity, Hall voltage, mobility and carrier concentration were calculated from the equations 4.1 - 4.12. These measurements were repeated three times each for two different current values. Table 4.1 consists of properties calculated for samples with 0.1 μA of current at different thicknesses as shown.

Sample	**No. of Layers**	**ρ (Ω-cm) (Ag contact)**	**ρ (Ω-cm) (Au/Ag contact)**	**n (cm^3) (Ag contact)**	**n (cm^3) (Au/Ag contact)**	**μ (cm^2/Vs) (Ag contact)**	**μ (cm^2/Vs) (Au/Ag contact)**
5L800C-0.5-SiO_2/Si	5 ML		1.8E-4		3.12E17(+/-14.8%)		10.78 (+/-14.8%)
6L800C-0.5-SiO_2/Si	6 ML		0.0035		6.44E18(+/-4.5%)		28.57 (+/-4.5%)
8L800C-0.5-SiO_2/Si	8 ML		0.0012		3.11E18(+/-1%)		49.12 (+/-1%)
11L800C-0.5-SiO_2/Si	11 ML		0.0017		5.61E19(+/-1%)		36.69 (+/-1%)
13L800C-0.5-SiO_2/Si	13 ML		0.0029		6.79E19(+/-1%)		76.92 (+/-1%)
20L800C-0.5-SiO_2/Si	20 ML	0.0032	0.0026	2.62E19(+/-2.5%)	1.35E17 (+/-25%)	18.73 (+/-2.5%)	1.62 (+/-25%)
27L800C-0.5-SiO_2/Si	27 ML	0.615		1.38E18 (+/-6%)		18.53 (+/-6%)	
56L800C-0.5-SiO_2/Si	56 ML	0.105	0.16	3.14E20 (+/-2%)	4.29E20 (+/-6%)	4.62 (+/-2%)	5.04 (+/-6%)

Table 4.1: Table of extracted properties including resistivity, doping concentration and electron mobility obtained from Hall measurement at different thicknesses of the thin films measured using Au/Ag and Ag contacts as specified at a current of 0.1 μA

All the samples listed in Table 4.1 were measured and their corresponding properties were plotted according to thickness of the thin film to observe the effect of thickness on the mobility, resistivity and doping concentration. They have been presented for two currents, namely 0.1 μA and 1 μA as shown in the Figures 4.4, 4.5 and 4.6. For each data point in these plots, an average has been taken over three measurements of Hall voltage and resistances, from which the corresponding mobility, resistivity and doping concentrations were computed. The error bar in the plots correspond to the error obtained during these measurements. For the voltage measurements from the Keithley and Picotest, there was a residual voltage observed before application of current, which was recorded and subtracted from the measurements for improved accuracy.

The Hall voltages obtained in the measurements as calculated from equation 4.10 was negative for all the measurements, implying that the majority carriers in the thin films were electrons. This matches the expectation of MoS_2 thin films being n-type in nature from literature.

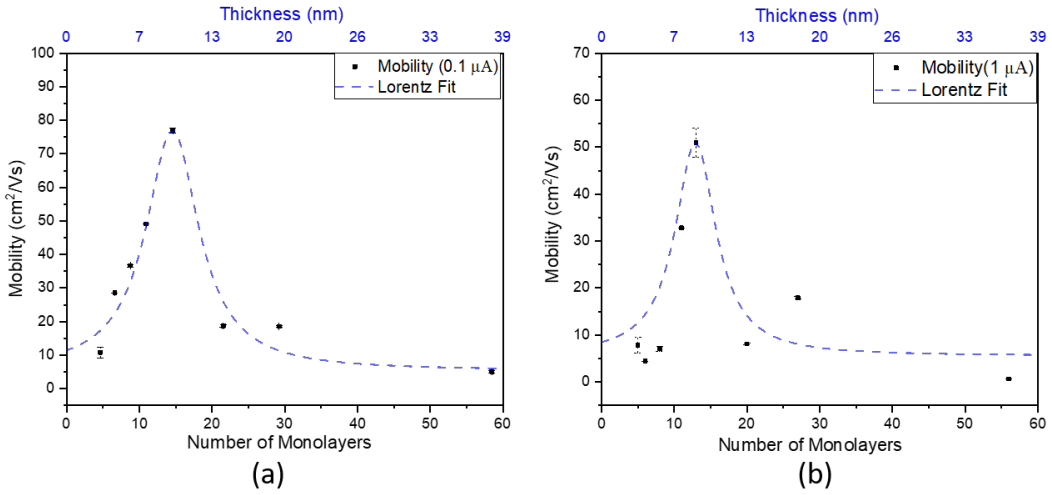

Figure 4.4: Hall mobility trend across thicknesses at (a) 0.1 μA and (b) 1 μA

Figure 4.4 shows the trend of electron mobility as calculated over different thicknesses shown in Table 4.1. Each measurement for each current value over the different samples was recorded thrice, and the error obtained in the V_H and R_s measurements were propagated to the mobility, resistivity and doping concentration calculated from the equations 4.12, 4.5 and 4.14 respectively. From the plots,

it can be observed that the mobility increases as the number of monolayers in the sample increases from 5 monolayers up to 13 monolayers, after which there is a decrease in the mobility observed for samples thicker than 13 monolayers. This trend can be observed for both the currents.

The trend can be correlated with other studies performed with mobility measurements in MoS_2 based transistor devices [94; 93]. In the study by Lin et. al., the change in mobility with change in number of layers was observed in a back gated MoS_2 based transistor which was fabricated with mechanically exfoliated MoS_2 flakes of different thicknesses. A comparison of the mobility values obtained in our study and approximate mobility values obtained in the study by Lin et. al. for different number of layers has been shown below in Table 4.2. [94].

No. of Layers	**μ (cm^2/Vs) (our study)**	**μ (cm^2/Vs) (study by Lin et. al.)**
1	-	0.001
5	10.78	35
6	28.57	105
8	49.12	85
11	36.69	60
13	76.92	20
20	18.73	-
27	18.53	5
56	4.62	-

Table 4.2: Table containing extracted electron mobility obtained from Hall measurement at different thicknesses of the thin films measured in our study at a current of 0.1 μA, as compared with the approximate electron mobility obtained for different thicknesses in the study by Lin et. al. [94]

On comparing these studies with ours, it can be seen that the electron mobility appears to follow a similar trend of an increase in mobility with thickness, with the maximum value obtained at around 8-14 monolayers, and then a subsequent decrease in mobility as the thickness increases further. One possible explanation for the increase in mobility from 1 to 13 layers observed in these studies and ours has been that as the number of layers decreases, there are properties unaccounted for in traditional semiconductors which affect the mobility in the case of 2D semiconductors.

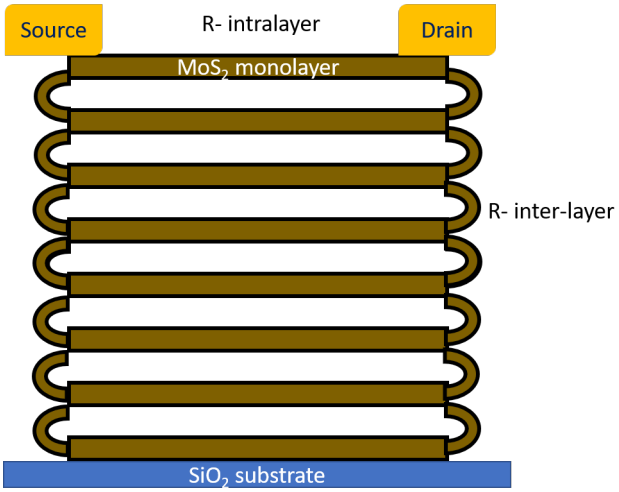

Figure 4.5: A schematic of the resistor network model (RNM) theory for MoS_2 thin films

In the study by Lin et. al., the increase in mobility from 1-5 monolayers has been explained due to the increase in the density of states and lower Schottky barrier as the number of layers increases, which increases the number of states available for electrons, thereby, improving the mobility. Some studies have also mentioned the effect of anomalous quantum hall effect and valley hall effect. With < 5 monolayers of MoS_2, due to the opposing Hall effect produced in electrons from different valleys, there could be reduced mobility, which increases as the density of states increases with increase in the number of monolayers [99].

It was also suggested that with increasing number of number of monolayers, there is an improved screening of substrate or charge scattering, which also helps improve the mobility. However, as the number of monolayers increases beyond 8-14 monolayers, there is a decrease in mobility observed, which can be attributed to the weakening of electron-phonon interactions due to Coulombic scattering caused by charge impurities. .

Another explanation was provided by Das et. al. where a multilayer MoS_2 thin film sample was modeled using a resistance network model with an interlayer resistance with interlayer coupling and intralayer resistances present in figure 4.5 [100]. The interlayer coupling resistance is thought to originate from the coupling occurring between two monolayers of MoS_2, which allows for charge hopping from one

layer to another, and then conducting channels within each layer. The intralayer resistance is attributed to the true channel resistances. Due to the Thomas- Fermi screening effect, it is predicted that due to the higher screening from the substrate and impurity charges as the number of layers increases, an increased mobility is observed. However, beyond a point (10-13 monolayer), the mobility reduces again, due to the presence of coulombic and defect associated charge scattering [94].

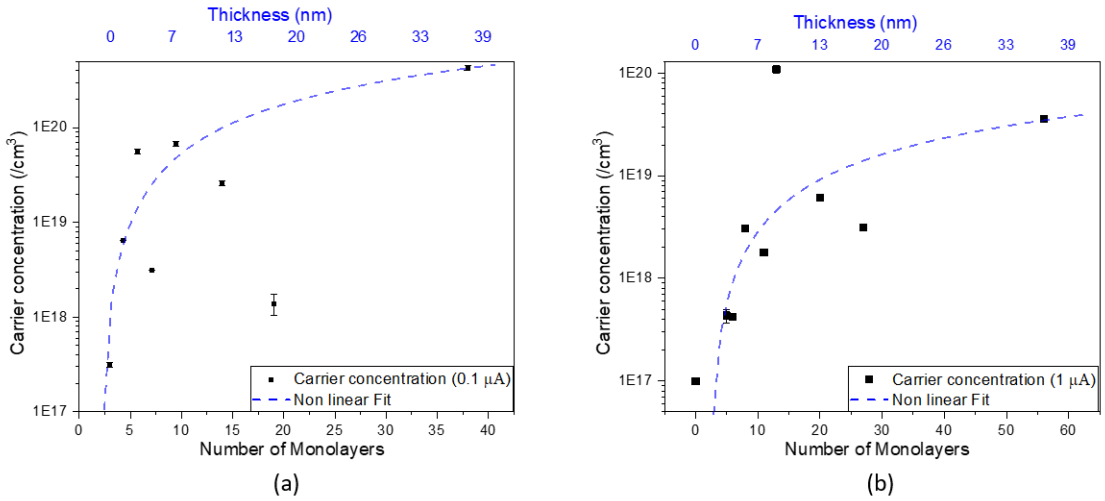

Figure 4.6: Doping concentration trend across different thicknesses of MoS_2 at (a) 0.1 μA and (b) 1 μA

Other properties such as doping concentration and resistivity were also plotted with thickness in our study. From Figure 4.6, it can be observed that the doping concentration appears to increase sharply from 5 monolayers to around 13 monolayers and then gradually increase upto around 60 monolayers as seen in the plots for both the values of currents. This trend can be attributed to an increase in the number of lateral strain related defects and impurity defects with increasing number of layers, causing charge trappings. These could be contributing to the higher doping concentration with increase in the number of layers.

From Figure 4.7, it can be seen that the resistivity also shows a similar trend with a gradual increase in in resistivity with increase in the number of monolayers from 5 monolayers to 20 monolayers, and a sharp increase upto 60 monolayers. There is one anomalous point at 27 monolayers which could be a measurement error. The

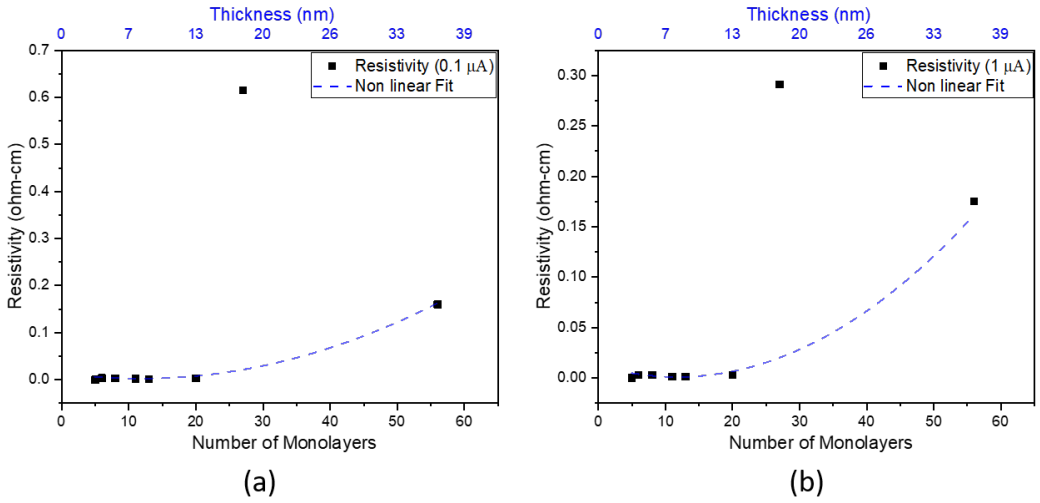

Figure 4.7: Resistivity trend across different thicknesses of MoS_2 at (a) 0.1 μA and (b) 1 μA

increasing resistivity could also be explained with the possibility of an increase in defects with thickness.

In all of these cases, repeated measurements with multiple samples would help improve the accuracy of the measurements, and help improve the confidence of measurements.

4.4 Challenges faced during Hall Measurements

There were many challenges faced during these measurements. One of the most important being repeatability. Due to the manual cleaving of the samples after the growth, it was hard to produce consistently accurate 7 mm x 7 mm samples for the measurements. The cleaving may also have resulted in stress and strain effects in the film. This could not be avoided as the substrate holder used has clips to hold the substrate. Due to the positioning of the clips and a quartz window used to shield the reflective mirrors from coating due to the plume particles, the positioning of these clips could not be varied much, and samples with areas larger than required were used for deposition, and then cleaved to remove the clip mark regions afterwards. Additional samples to improve the repeatability of measurements were also unable to be grown due to the limited availability of the PLD tool

because of administrative issues.

In addition, due to the nature of the growth (with some sample areas being at different positions with respect to the plume), there may have been slight variations in thickness across the sample surface, which was attempted to be accounted for as described in Figure 4.2. The sputtering of Au on the sample was performed with a Kapton shadow mask manually fabricated, which may have also contributed to some inconsistencies in the contact area of the Au with the MoS_2, which could be improved further with standardization of the mask and the sample area. This inconsistency coupled with measurement error would account for all the main sources of error.

Some of these challenges can be mitigated. Future growths performed on the new PLD system can be attempted to have a greater control of the plume region, thereby allowing for more uniformity in the thin film sample and the possibility of using pre-cut wafer pieces. Fabrication of thin film transistors using PLD deposited MoS_2 could enable smaller channel regions, and therefore, fewer defects over the surface of measurement, leading to more accurate measurements. Patterning and deposition of Au contacts would also help provide a better control over the contact area of the thin film with Au.

4.5 Conclusions and Future Work

In this study, Van der Pauw method of Hall measurements was conducted over different thicknesses of MoS_2 thin films to measure the Hall voltage and resistance to extract properties such as Electron mobility, resistivity and doping concentration. An increase in mobility was observed from 5 monolayers to 13 monolayers, after which a decrease was observed upto 56 monolayers. This trend is consistent with other studies, which can be explained by the presence of anomalous quantum hall effect and valley hall effect with lower number of monolayers, coupled with lesser substrate and impurity screening in lower number of monolayers. Over around 10-15 monolayers, mobility reduces, due to the coulombic scattering and structural defects. In both doping concentration and resistivity trends, an increase was ob-

served with increasing number of monolayers possibly due to increased structural defects and charge trapping.

Due to the limited understanding of the transport mechanism in 2D semiconductors and the quantum effects on the electron transport when the number of layers of MoS_2 decreases, there is a great scope for future work in this area. Once some of the challenges of of measurements have been mitigated, future understanding into the temperature dependence on mobility, doping concentration and resistivity can be studied and compared with some of the studies already performed. Theoretical modeling of the resistance network model and comparison with the layer dependent Hall measurements could help improve the understanding of these trends observed in this study. Repeated measurements of these samples would also help improve the reliability of these measurements and improve the confidence of measurements.

Chapter 5

Preliminary studies on a simulation study and device fabrication study of MoS2 based devices

Once the material and electrical properties of the PLD grown MoS_2 were extracted, preliminary investigations into the application of these thin films for electronic device application was explored through simulation and fabrication studies. Although these results were preliminary, they proved as a starting point for the study of future transistor devices based on PLD grown MoS_2 thin films.

Ohmic and Schotkky contact formation is one of the major challenges in making good 2D semiconductor devices. The interface contact type and its properties between metals and MoS_2 plays a big role in the transport phenomena of a MoS_2 based electronic device. Thus, in order to understand and optimize the device design, some preliminary device simulations have been conducted, along with preliminary fabrication studies of MoS_2 based devices.

The simulation studies consist of two parts. The first study was a 2D simulation of Schottky contacts formed by multilayer MoS_2 with different metals with low work

functions (such as scandium, molybdenum, tungsten) and high work functions (gold, nickel, platinum). The three metals chosen for this study were molybdenum (Mo), tungsten (W) and gold (Au) in order to study properties such as Schottky barrier height and turn on voltage for potential application in MoS_2 based devices. This was simulated based on the Schottky Mott theory using Synopsys TCAD as a first step, since it was the easiest to simulate, although it has been shown that this theory is not accurate for 2D material based contacts [101]. A second simulation study was a 1D simulation that was performed with monolayer MoS_2 based transistor devices with highly doped MoS_2 contacts using NanoTCAD ViDES, however, due to processing issues with dimensions larger than 100 nm, these results were discarded.

The experimental study involved fabrication of heterojunction diodes with p-silicon (p-Si) as a p-type semiconducting layer with MoS_2 as an n-type semiconducting layer. The n-type nature of MoS_2 has been established through the Hall measurements in chapter 4 as well as references in literature. Experimental extractions of current-voltage (IV) and capacitance-voltage (CV) trends were observed and electrical proeprties such as doping concentration, depletion width and built in voltage were calculated.

5.1 Simulation and study of Schottky contacts formed by MoS_2

Synopsys TCAD was employed for the simulations in this section. The modules can be broadly categorized into process simulation and device simulation. All of these modules can be accessed and arranged as per the flow required on the Sentaurus Workbench.

The first step of the simulation was the creation of the the tool flow for a new project. The tools used for the particular devices being simulated included Sentaurus Device Editor (SDE) to simulate the process of device design along with meshing the structure in the device to compute transport properties. This was

followed by Sentaurus Device (SDevice) to simulate the device physics, transport and electronic behavior. The plots obtained from the SDevice simulation were visualized using SVisual tool. A schematic of the tool flow used can be seen below in Figure 5.1.

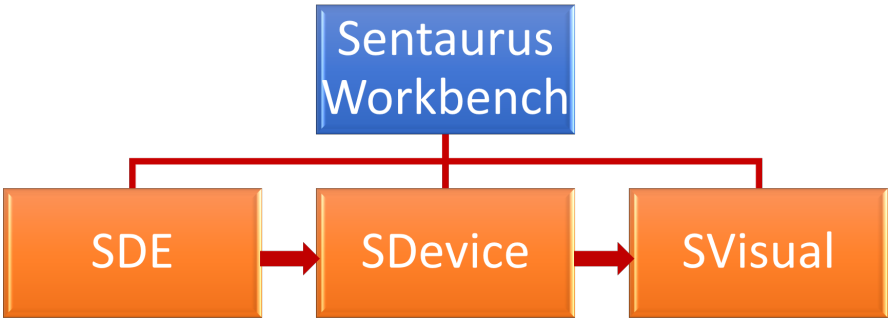

Figure 5.1: Schematic of the TCAD workflow

A 2 dimensional geometry of the device was created using the SDE. Here, a 5μm long MoS_2 thin film which had a thickness of 1μm. Although a thinner film was desired, due to convergence issues, a 1μm thin film was simulated. A bottom Ohmic contact was assigned, and a top Schottky contact with variable lengths from 1-5μm was specified. The top Schottky contact metal was varied by changing the Work Function values in the SDevice script corresponding to the value of the desired metal as 4.38 eV, 4.74 eV and 5.43 eV for Mo, W and Au respectively. The structure created has been shown below in Figure 5.2.

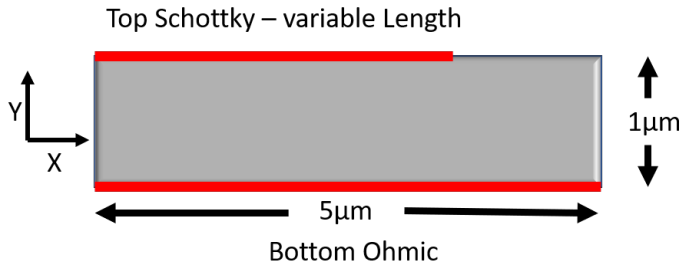

Figure 5.2: Schematic of Schottky contact simulated by TCAD Sentaurus

Once this structure was created, the semiconductor and contact regions were defined and labeled. Following this, a global uniform mesh of 0.5 μm was defined over

the entire region. Then, a multibox placement was performed to specify isotropic grading, of an area of 0.1μm width along the X direction and a graded mesh of ratio 1.4 with the smallest size of 0.005μm from the top Schottky contact to 0.5μm below the contact in the Y direction.

The meshed structure and the geometry were compiled and stored into a mesh file and a geometry file. These files along with the parameter file of the materials used in the device were given as an input to the SDevice module. N-type doping of n = 1E17/cm^3 was set by changing the value of the Fermi level of the material as per the equation below, where the intrinsic doping concentration of MoS_2 n_i was taken to be 2.7E14 /cm^3.

$$\Delta E_{\mathrm{FN}} = k_{\mathrm{B}} T ln \frac{n}{n_{\mathrm{i}}} \tag{5.1}$$

Where E_{FN} is the shifted Fermi level with n-type doping, k_B is the Boltzmann's constant T is the temperature in Kelvin, n is the doped concentration of the material and n_i is the intrinsic concentration of the material.

One of the primary issues with this tool was the lack of a material parameter file for MoS_2 in the software suite. This led to the creation of a completely new material parameter file (.par file) for MoS_2 based on the material properties known to us from literature and from the studies in our group. The properties of MoS_2 used for the parameter file are shown below in Table 5.1. In this parameter file, the electron mobility value was taken as an average of the three values found in literature, which ranged from 10 - 200 cm^2/Vs [102; 54; 103]. The parameter file had limitations, where it was only able to be applied in a device with drift-diffusion current transport model, and was not able to account for the 2D material transport phenomena and the layer dependent transport.

The SDevice code firstly involves the definition of workfunction of the Schottky metal contact being used. Based on the simulation of either Mo, W and Au, the respective work functions were input as 4.38 eV, 4.74 eV and 5.43 eV as obtained from a study in a group [101]. The process flow for the simulation involves multiple models, each module performs various functions by using tools to solve steps such as device design and the equations for transport models. As a first step,

Property	**Symbol**	**Value**
Relative permittivity	ϵ_{r}	3.7
Effective mass of electron	$\frac{m_{\mathrm{e}}}{m_{\mathrm{o}}}$	0.54
Effective mass of hole	$\frac{m_{\mathrm{h}}}{m_{\mathrm{o}}}$	0.40
Intrinsic doping value	$\mathrm{n_i}$	2.7E14 /cm^3
Doping concentration value	n	1E17 /cm^3
Thermal conductivity	K	1.05 W/mK
Bandgap	$\mathrm{E_G}$	1.20 eV
Electron mobility	μ_{e}	50 cm^2/Vs [102; 54; 103]
Electron Affinity	χ	3.9 eV

Table 5.1: Material properties and parameters of MoS_2 used in the TCAD material parameter file created for the TCAD simulations.

the hydrodynamic model (HD) which solves the carrier temperature and the heat flow equations along with the Poisson and the carrier continuity equations for the drift-diffusion transport mode was used to simulate the current transport in the simulation.

For the physics model section, parameters such as a uniform mobility, uniform doping concentration, tunneling models and doping profiles were specified from the properties obtained in Table 5.1, along with specification of an anisotropic profile for the model. Plotting of properties required, such as doping profiles, electron current and electric field were input. The math section of the code included specifications of the number of iterations as 1000 iterations for transport model calculations and a 7 digit accuracy for the measurements. In the Solve section, voltage range of measurements was set from 0 - 1.5 V, with a step size of 0.05 V specified.

The results generated from the script above were visualized in SVisual. The I-V plots for different lengths of Schottky contacts for the three different metals have been plotted in Figure 5.3.

The Schottky barrier ϕ_{B} was calculated from the equation 5.2.

$$\phi_{\mathrm{B}} = \phi_{\mathrm{M}} - \chi \tag{5.2}$$

where ϕ_{M} is the work function of the metal used and χ is the electron affinity of

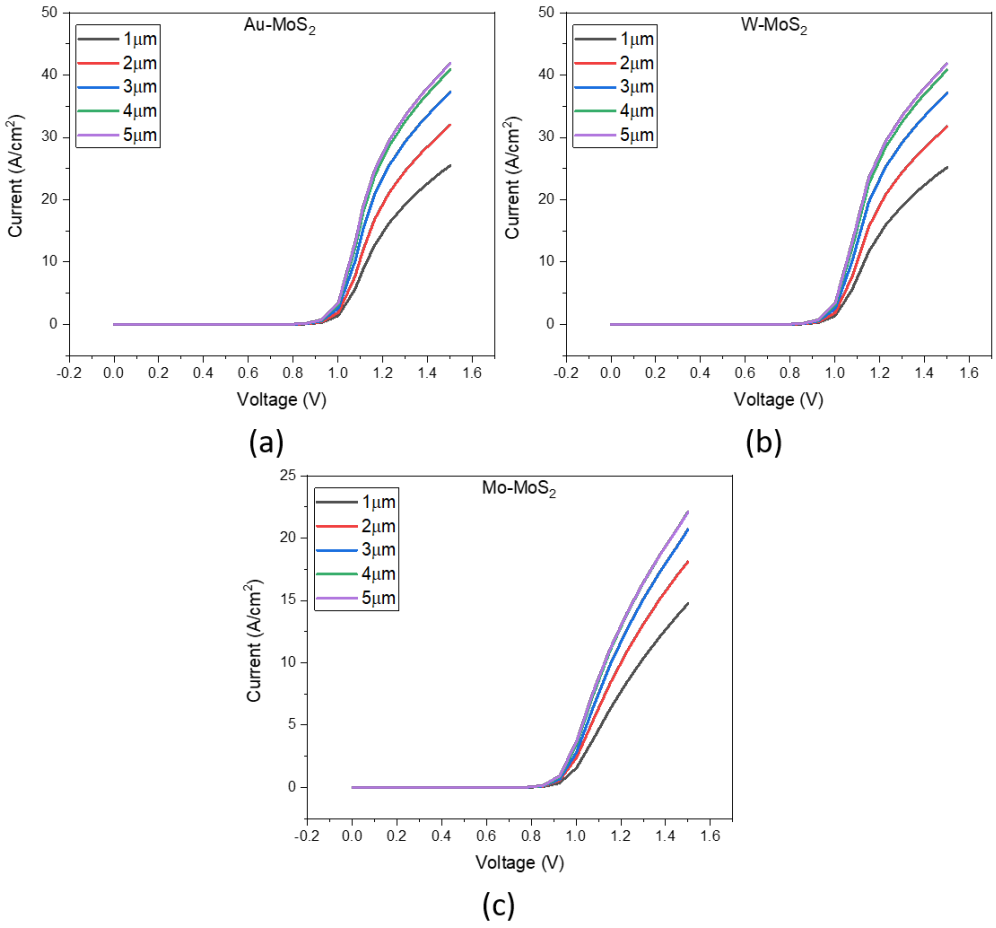

Figure 5.3: I-V plots of Schottky contact formed by MoS_2 thin films with contact metals (a) Au, (b) W and (c) Mo over varying contact lengths from 1 - 5 μm under a voltage sweep from 0-1.5V and a step size of 0.05 V

MoS_2.

The built in potential V_{bi} was calculated as:

$$V_{bi} = \frac{\phi_B}{2} - \frac{E_G}{2} \tag{5.3}$$

where E_G is the bandgap of MoS_2.

Using the above equations, the following properties were derived for the different metal Schottky junctions as shown in Table 5.2.

Metal	Work Function (ϕ_M) [101]	Schottky Barrier height (ϕ_B)	Built in potential (V_{bi})	Turn on Voltage (V_t)
Au	5.43 eV	1.73 eV	1.115 V	0.971 V
W	4.74 eV	1.04 eV	0.253 V	0.967 V
Mo	4.38 eV	0.68 eV	0.065V	0.897 V

Table 5.2: Calculated Schottky barrier properties from Mo, W and Au metal contacts with MoS_2 thin films as simulated by Synopsys TCAD

From the plots, it was seen that as the contact length of the metal increased, the current value also increased, which is expected as there is more region of the thin film in direct contact with the the metal. It was also observed that the built in potential for Au contact was the highest at 1.115 V, with lower values for W and Mo of 0.253 V and 0.065 V respectively, which is attributed to the lower work functions of W and Mo being 4.74eV and 4.39 eV respectively as compared to Au (5.43 eV). The turn on voltages extracted from the graph showed a decreasing trend with 0.971 V, 0.967 V and 0.897 V obtained for Au, W and Mo respectively as seen from the table. This matches well with the expected behavior according to Schottky-Mott theory due to the decreasing order of work functions as Au $>$ W $>$ Mo.

Based on this preliminary analysis, a better material parameter file can be created based on further understanding of the material transport and electronic properties. A more accurate transport model coupled with simulations for films with thicknesses between 10-50 nm can be created from the newer libraries added to the Synopsys TCAD software in the latest updates, which can help improve the accuracy of these simulations.

5.2 Experimental studies of heterojunction P-N diode

An experimental design and fabrication of MoS_2 based devices was conducted as a preliminary study of the behavior of the PLD grown thin films in devices. In order to start with the simplest fabrication, p-Si and MoS_2 based heterojunction P-N diodes were fabricated and tested.

5.2.1 Process flow of device fabrication

The process flow of device fabrication with Au electrodes has been shown in the figure below in Figure 5.4.

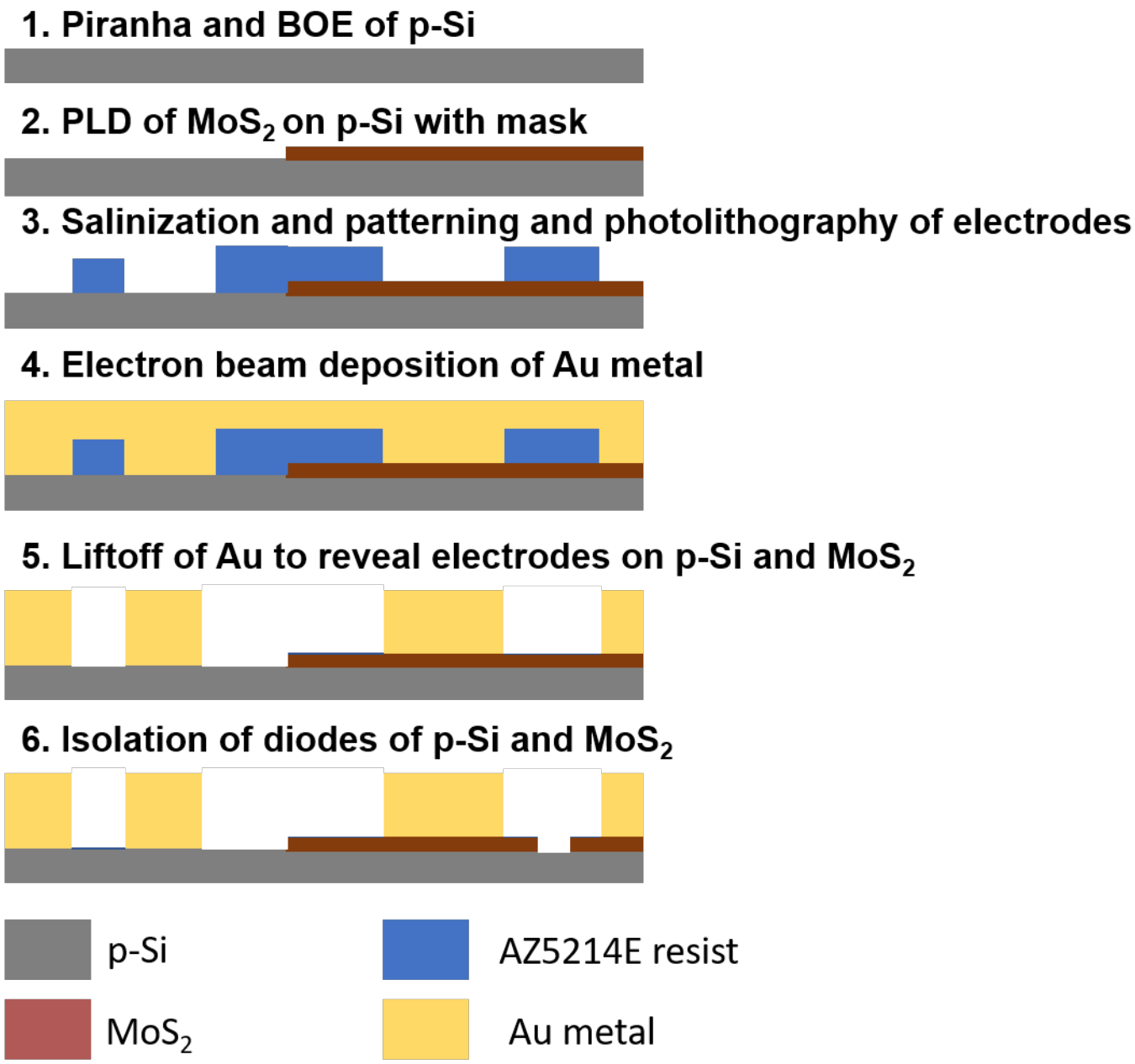

Figure 5.4: Process flow of diode fabrication of p-Si and MoS_2 based heterojunction diodes.

First, a prime p-Si wafer with a high doping concentration of 3E18/cm^3 was first cleaved into pieces of around 2.5 cm x 2.5 cm to fit the substrate holder. Then, the pieces were cleaned with Piranha solution to remove the organic contaminants. They were then etched with buffer oxide etching (BOE) solution with a 49% concentration HF in order to etch the native SiO_2 layer formed on a prime wafer. After this, 14 nm thick MoS_2 thin film was deposited on the wafer pieces with a shadow mask to Si regions using PLD. The growth was performed at 800^0 C with a post growth anneal period of 30 min at the growth temperature at a substrate target distance of of 5 cm, a fluence of 2.2 J/cm^2 and a gas ambient of 0.5 mT of Ar during deposition.

Following this deposition, the sample was primed with HMDS for salinization to make the surface hydrophobic, and metal contact electrodes over the p-Si and MoS_2 regions of size 100 μm x 100 μm were patterned using optical lithography with AZ5214E photoresist. 50 nm thick Au metal thin film was deposited on the patterned samples using electron beam lithography, following which liftoff was performed to remove the resist regions to form the contact electrodes on both the MoS_2 and the Si regions as shown in Figure 5.4. Individual devices were isolated by using a diamond scribe to scratch out the regions. This isolation was performed as a good etching procedure for large area MoS_2 thin films is still being explored actively, and as such, a suitable technique has not been found so far. The isolated device with electrodes on Si and MoS_2 formed a lateral design of the device. The vertical design of the device was formed by connecting a copper tape to the bottom of the Si wafer. These two designs have been shown in Figure 5.5.

To begin with, the higher doped p-Si was was used for the device fabrication with Au electrodes with the two configurations discussed above. Possibly due to the defects in the Mos_2 thin films, the vertical devices behaved poorly as the current just passing through the thin film without a diode behavior observed. This was the case with most of the lateral configuration devices as well, except for two devices that showed a diode like behavior with both IV and CV measurements performed as shown in the next section.

Following this experiment, lower doped p-Si (doping concentration of 5E14/cm^3) was used to make heterojunction diodes in lateral mode and vertical mode. The

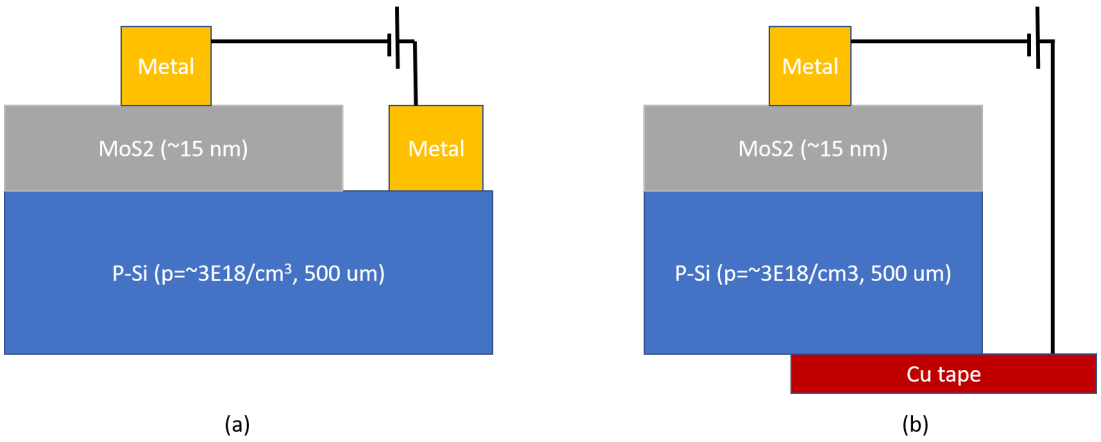

Figure 5.5: Configurations for diode measurements in (a) lateral and (b)vertical modes in the p-Si and MoS_2 based heterojunction diodes.

IV measurements have been presented in the next section.

5.2.2 Preliminary Electrical characterization of the devices and Carrier Concentration extraction

A majority of the devices measured on higher doped p-Si had very high currents and highly linear I-V curves as shown in Figure 5.6. The absence of a diode like curve could be due to the defects within the MoS_2 thin film allowing the current to pass right through it. In addition, due to the high doping of both MoS_2 (as estimated from the Hall measurements) and p-Si used, the depletion width of the junction could be very narrow, causing this behavior.

Several of the devices presented negative capacitances, further implying that there may be a very narrow depletion width, which when coupled with defects in the MoS_2 thin films could be causing current to pass right through the p-Si. Two of the devices measured exhibited a diode like IV and positive capacitance values. The IV and CV plots of these two devices have been shown below.

The IV measurements were performed over a voltage range of -0.5 V to 1.5 V. The CV measurements were performed over a voltage range of -0.05V to 0.1 V for sample 28May/19-800CpSi-B1 and -0.1 V to 0.25 V for sample sample 28May/19-

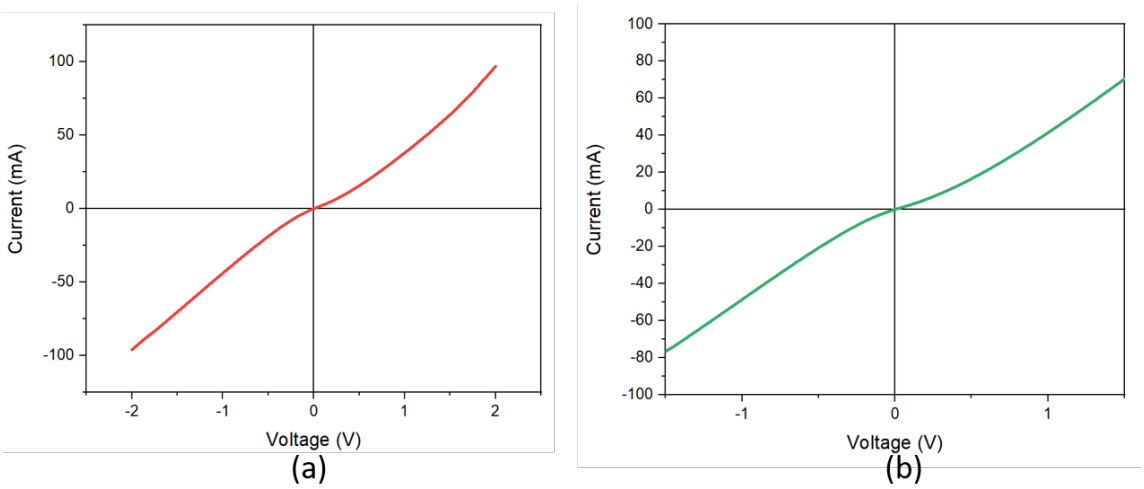

Figure 5.6: IV curves of devices (a) 28May/19-800CpSi-A1 and (b) 28May/19-800CpSi-A3

800CpSi-B1 as shown in Figure 5.7 and 5.8 as shown. The equation used for the calculations is presented below.

The capacitance of the depletion width obtained in the CV can be given by:

$$C_{\text{dep}} = \frac{A\epsilon_{\text{p}}\epsilon_{\text{n}}}{W_{\text{dep}}(\epsilon_{\text{p}} + \epsilon_{\text{n}})} \tag{5.4}$$

where A is the area of the device. The depletion width W_{dep} of the junction is given by:

$$W_{\text{dep}} = x_{\text{p}} + x_{\text{n}} \tag{5.5}$$

where x_{p} and x_{n} are the depletion width in the p and n type regions respectively. These can be calculated as:

$$x_{\text{p}} = (\frac{2}{q}\epsilon_{\text{p}}\epsilon_{\text{n}}\frac{N_{\text{D}}}{N_{\text{A}}}\frac{V_{\text{bi}}}{(\epsilon_{\text{p}}N_{\text{A}} + \epsilon_{\text{n}}N_{\text{D}})})_{0.5} \tag{5.6}$$

$$x_{\text{n}} = (\frac{2}{q}\epsilon_{\text{p}}\epsilon_{\text{n}}\frac{N_{\text{A}}}{N_{\text{D}}}\frac{V_{\text{bi}}}{(\epsilon_{\text{p}}N_{\text{A}} + \epsilon_{\text{n}}N_{\text{D}})})_{0.5} \tag{5.7}$$

where ϵ_{p} and ϵ_{n} are the dielectric constants of p and n region respectively, N_{A} and N_{D} are the acceptor and donor carrier concentrations respectively. From these

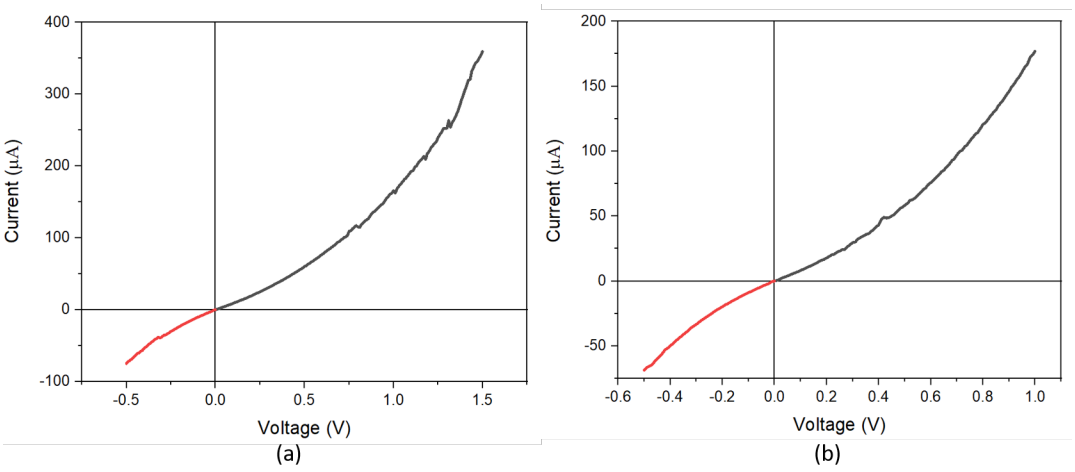

Figure 5.7: IV curves of devices (a) 28May/19-800CpSi-B1 and (b) 28May/19-800CpSi-B2 for a voltage sweep between -0.5 V to 1.5 V

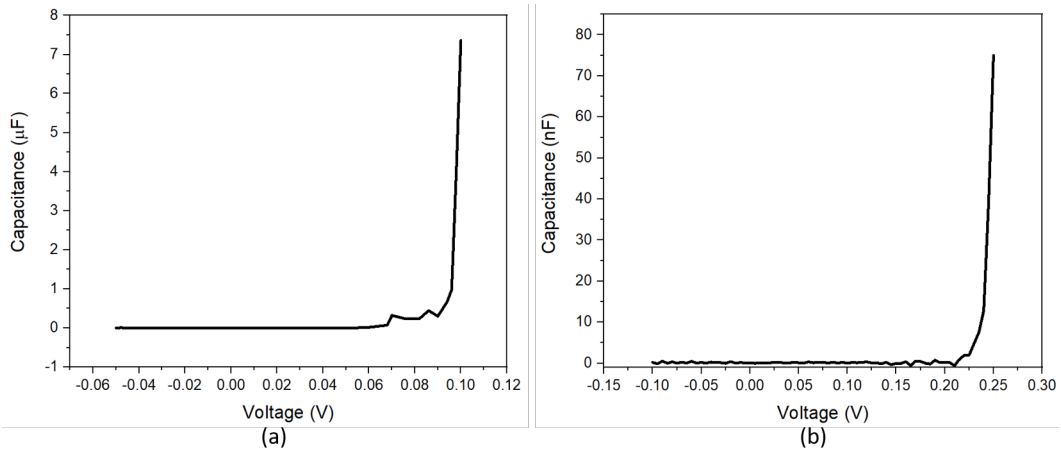

Figure 5.8: CV curves of devices (a) 28May/19-800CpSi-B1 for a voltage sweep of -0.05 V to 0.1 V and (b) 28May/19-800CpSi-B2 for a voltage sweep of -0.1 to 0.25 V

equations, carrier concentration of MoS_2 or the donor can be calculated, as N_A is known for p-Si.

From the $1/C^2$ vs V plot, the built in voltage V_{bi} was extracted from both the cases using the equations 5.4 - 5.7. The plots in Figure 5.9 depicts the graphical extraction of built in potential and the extraction of the doping concentration of MoS_2 given the doping concentration of p-Si.From the above measurements and calculations, the extracted properties have been listed in Table 5.3.

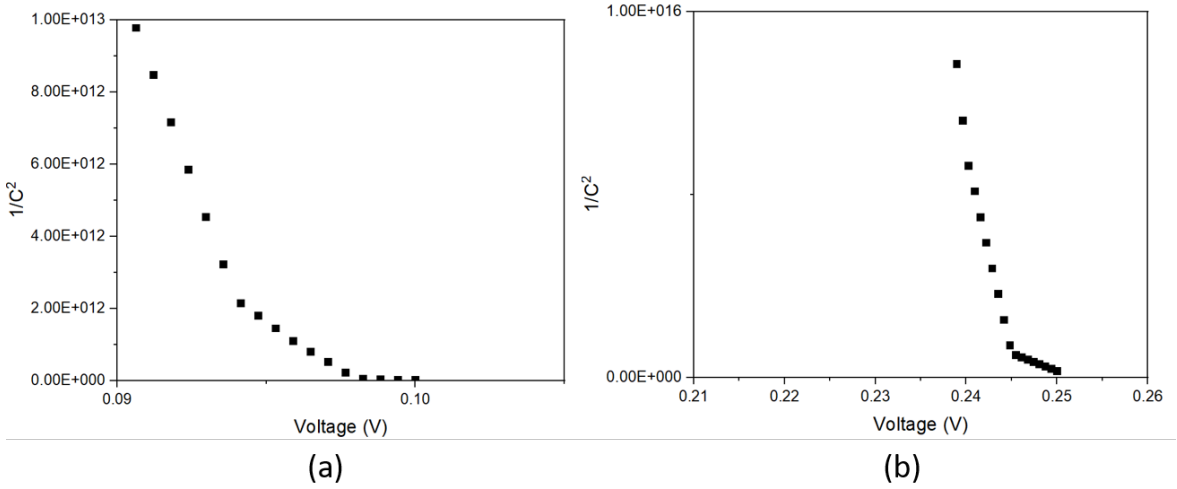

Figure 5.9: Built in potential extraction from the $1/C_2$ vs V curves of devices (a) 28May/19-800CpSi-B1 and (b) 28May/19-800CpSi-B2

Sample	**V_{bi} (V)**	**Area (cm^3)**	**Doping concentration N ($/cm^3$)**	**Depletion width (cm)**
28May/19-800CpSi-B1	0.098	5E-3	9.12E18	9.59E-6
28May/19-800CpSi-B2	0.248	5E-3	2.45E18	2.58E-6

Table 5.3: Calculated doping concentration of PLD deposited MoS_2 thin films and the depletion width of the heterojunction devices fabricated.

Following these studies, it was seen that the depletion width in both the devices was very small. The doping concentrations of 9.12E18 and 2.45E18 obtained in these results match closely with the doping concentration obtained for thin films of thickness of 14 nm (sample 20L800C-0.5-SiO_2/Si) from the Hall measurements (around 2.6E19/cm^3). The calculated built in potential of 0.098 V and 0.248 V was also very small, and so it was thought to try this experimental method on

lower doped p-Si substrates to increase the depletion width, and obtain a larger number of measurements with consistent results.

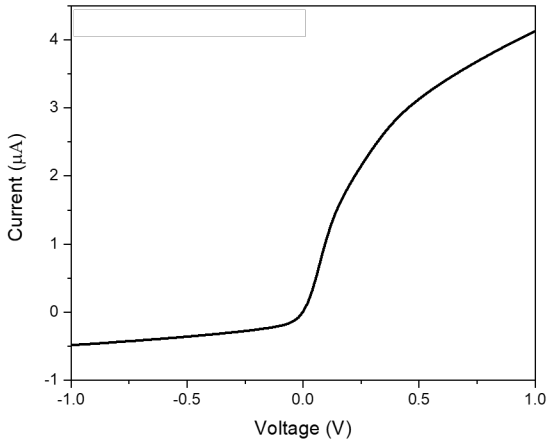

Figure 5.10: IV plot of a diode fabricated with lower doped p-Si substrates with a voltage sweep of -1 V to 1 V.

Heterojunction diodes were fabricated under the same conditions with a p-Si wafer of doping concentration of 5E14. The IV characteristics of a representative device has been presented in Figure 5.10. In this case, the IV curve showed a more diode like behavior in the lateral mode with a smaller leakage current in reverse bias when compared to the devices measured in Figure 5.7. The vertical mode of measurement in this case also showed linear behavior, which might be due to the presence of defects in the MoS_2 thin films deposited on the p-Si. The CV measurements yielded negative capacitance values for all ranges of voltages, indicating contact issues between p-Si and MoS_2 thin films. The poor performance of these devices could also be attributed to the higher amounts of MoO_3 found in the thin films (ratio of MoS_2 to MoO_3 being 1.8:1 from Table 3.6), which could imply poorer crystallinity and composition of the thin films.

5.3 Conclusion and future work

Preliminary simulation and fabrication work was performed on MoS_2 thin film based devices. From the simulation study, the challenges faced during these processes have been listed below.

5.3.1 Challenges faced by simulation processes used

One of the major challenges faced by both of the softwares was the lack of proper transport models available for multilayer MoS_2 thin films. In TCAD, a new parameter file was created, with approximated values as some of the parameters were not available in literature, which implies that experimental implementation of these devices would behave differently owing to these approximations.

Complexities in the device geometry also caused issues in compiling of the simulations. In both cases, there were restrictions placed on the device dimensions and geometry owing to several issues with converging and processing speed. Due to the models not accounting for things like imperfections and defects in the crystal structure, interactions between contacts formed between the thin film and contact metals, the results obtained by these simulations studies would be very different from experimentally fabricated devices with the same structures as those simulated.

5.3.2 Challenges faced during fabrication

There were several challenges faced during fabrication of these devices. One of the primary challenges was enabling a good contact between p-Si substrate and the MoS_2 thin film. While BOE was performed to strip the native oxide layer on p-Si, due to the high temperatures of deposition and the imperfect vacuum in the chamber, there is a possibility of an oxide layer forming on the substrate before MoS_2 deposition and before the metal deposition step as well. This could cause additional defects in the junction between the two materials.

Due to the differences in work functions of the two different materials in the het-

erojunction device, it was seen that using the same metal as a contact for both of the materials would not work as an ideal ohmic contact is desired on both sides. Therefore, a two stepped process with two different metals deposited would be a better approach for this process.

Etching of large area MoS_2 thin films has been a major challenge in the fabrication of large area MoS_2 based devices. A study into the different viable techniques of wet and dry etching forms would be useful to improve the device fabrication in the future. As the device isolation was performed manually using a sharp diamond scribe to scratch the device regions out, it might have been hard to truly separate the regions, and a cleaner process of etching would be desirable for device isolation in the future.

5.3.3 Future Work

Based on these preliminary investigations, there are several directions that can be pursued to study the behavior of MoS_2 based devices. On the simulation front, in TCAD, improvements to the MoS_2 material model can be made by further literature review and by using software such as ATK-DFT to model some of the more fundamental properties and transport models. Following this, a 3D simulation of the current structure can be attempted, and simulation of MoS_2 transistors can also be tried on the 2D and 3D levels to understand more about the transport properties. NanoTCAD ViDES can be attempted to be coded with an added dimension to study the behavior when modelled as a 2D or 3D model. In addition, increasing the number of monolayers to study the layer dependent electrical behavior can also be performed.

On the fabrication front, further research into effective etching techniques for MoS_2 can be performed to fabricate MoS_2 based transistors along with heterojunction diodes to compare the electrical properties measured by both the methods. In addition, improvements to the lithography process and the adoption of two metal contacts for the heterostructure diode could help improve the characteristics and extract more consistent properties.

Chapter 6

Optimization and PLD growth of LMFCr

Pulsed laser deposition as a growth technique was explored for stoichiometric growth of complex perovskite catalytic electrode (LCFCr and LSFCr) materials in order to allow for the deposition of smooth and uniform films. To overcome problems in the film quality such as inconsistencies in the elemental composition, high porosity and high surface roughness, aside from issues with reproducibility, PLD is explored as an alternative method to deposit uniform thin films with a higher control over the stoichiometry, with a higher degree of uniformity enabled by variation of the PLD parameters.

This chapter involves optimization of several PLD growth parameters such as, substrate temperature and post-growth anneal conditions. There is an emphasis on the material characterization of LCFCr thin films grown at three different substrate temperatures, 25^0C, 250^0C and 700^0C, with three different post-growth anneal conditions (without anneal, 30 min anneal in vacuum, and 2h anneal in vacuum) to obtain large-area smooth and uniform thin films for the solid oxide fuel cell (SOFC) applications on optimization of the PLD parameters. These catalytic electrode materials were grown on top of (001) yttrium stabilized zirconia (YSZ) solid electrolyte substrates for SOFC testing, and for lattice matching.

PLD grown LCFCr thin films were characterized by several material characteri-

zation techniques such as, X-Ray Diffraction (XRD) to study crystal orientation, atomic force microscopy (AFM) to measure film roughness and perform grain imaging along with X-ray photoelectron spectroscopy (XPS) for elemental, chemical and electronic state analysis of the thin films. Transmission electron microscopy (TEM) was performed to measure the thickness, lattice structure and phase of the the thin film with the substrate.

The optimized growth conditions obtained from the studies with LCFCr thin films were maintained for the growths of LSFCr with no post growth anneal and a 30 minute and 2 hour post growth anneal period. LSFCr thin films were characterized by material characterization techniques, namely, XRD,AFM and XPS.

6.1 Optimization and growth of LCFCr

The LCFCr and LSFCr targets used for the study was prepared by the Birss group at the University of Calgary .The target was prepared with LCFCr and LSFCr powders prepared by glycine combustion method. They were cold-pressed into pellets (1 inch in diameter) and sintered at 1300 – 1400 ^{0} C in air. The laser used for the ablation was a KrF excimer laser (248 nm, 15 ns, 5 Hz). A chamber base pressure of 1x10^{-5} to 7x10^{-6} T was obtained for all of the growths.

6.1.1 Pulsed laser deposition of LCFCr on YSZ

For the preliminary optimization of PLD parameters, the laser fluence was varied from 1.2 J/cm^2 to 3 J/cm^2 and 3 J/cm^2 was found to be over the ablation threshold of the LCFCr target, and used for all the growths. Keeping the fluence fixed, the substrate-target distance was varied between 3 and 5 cm and fixed at 3 cm in order to obtain a higher growth rate. LCFCr thin films of around 50 nm thickness were grown on (001) YSZ substrates for all the conditions. Oxygen gas was used as an ambient gas to help improve the stoichiometry of the complex oxides grown. The chamber ambient pressure ranging from a base pressure of 1x10^{-5} T to 100 mT of oxygen gas were tested. The chamber ambient pressure was set at 50-60 mT of oxygen to allow for the presence of an oxygen environment to maintain the stoichiometry of the complex oxides along with being able to have a high enough

growth rate of the thin film.
PLD growths at three different substrate temperatures (25^0C 250^0C and 700^0C) were performed to optimize the growth temperature. These growths were performed in a gas ambience of 40-50 mT of oxygen with a laser fluence of 3 J/cm^2 on the target and a substrate – target distance of 3 cm. As-grown thin film samples at each of the temperatures listed above were subjected to different post anneal conditions- no anneal, 30 min anneal at 700^0C and 2h anneal at 700^0C. A summary of these growths is listed in the table below.

Sample	**Growth Temperature (^{0}C)**	**Post growth anneal period at 700^0C (min)**	**2θ peak position (^{0})**	**FWHM of XRD peak (^{0})**	**RMS roughness (nm)**
25-U	25	-	-	-	-
25-30mA	25	30	42.03	0.38	-
25-2hA	25	120	42.01	0.35	1.54
250-U	250	-	-	-	-
250-30mA	250	30	42.03	0.35	-
250-2hA	250	120	42.01	0.34	0.52
700-U	700	-	-	-	1.22
700-30mA	700	30	42.03	0.33	0.20
700-2hA	700	120	42.03	0.33	0.20

Table 6.1: Samples of LCFCr grown at 25^0C, 250^0C and 700^0C with different post anneal conditions- no anneal, 30 min anneal at 700^0C and 2h anneal with XRD results obtained using Bruker Discover D8 and RMS roughness corresponding to the samples

6.1.2 Optical microscopy studies

An image of the visual change in thin film appearance with these conditions can be seen in the Figure 6.1. From the figure, visually, it can be seen that as the annealing time increases, the films grew darker in colour across all three temperatures of growth (25^0C, 250^0C and 700^0C). As the growth temperature increases from 25^0C to 700^0C, it can be seen that the film changes from a metallic appearance with larger particulates to a smoother brown colored film.

Optical microscopy was performed at 63x magnification to observe the film continuity and morphology. All of the samples listed in table 6.1 were initially observed under optical microscope. Optical microscopy was employed for preliminary imaging of the thin films that were grown, and to study their uniformity, roughness and morphology. Optical microscope images reveal that the films grown at 25^0C appeared metallic before post growth anneal. The longer it was annealed, the film

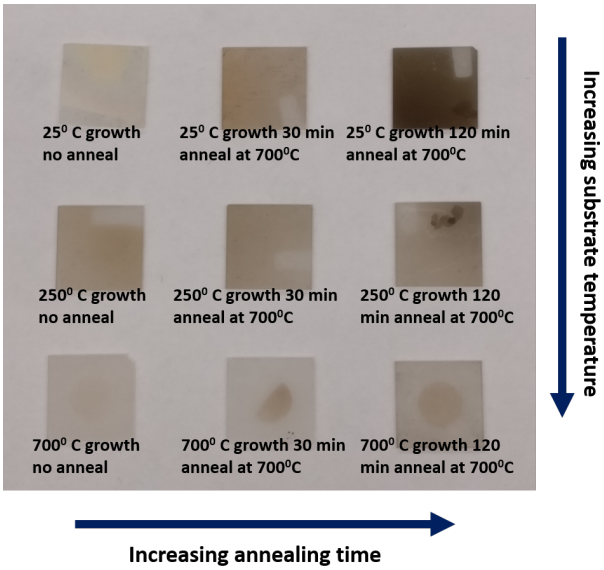

Figure 6.1: Visual images of the thin films deposited for the study grown at 25^0C, 250^0C and 700^0C with post growth anneal conditions of no anneal, 30 minute anneal at 700^0C and 120 minute anneal at 700^0C

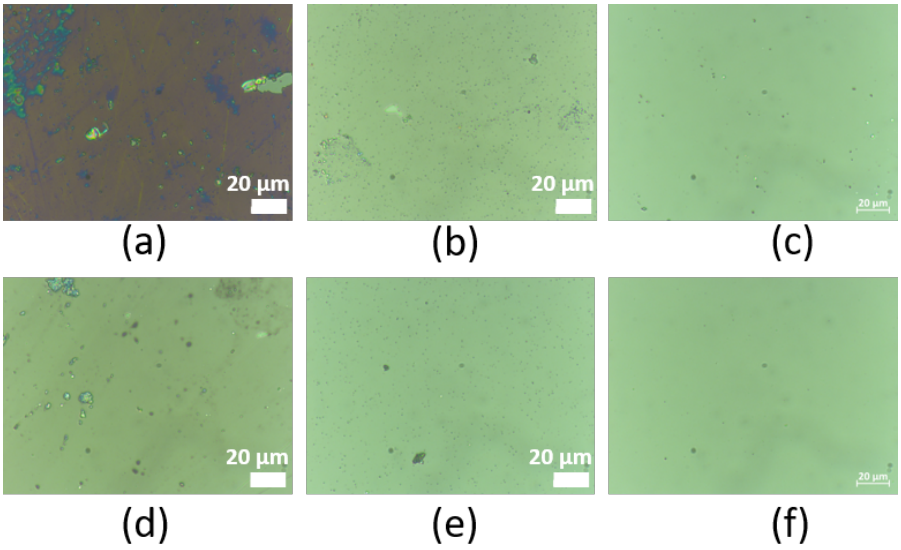

Figure 6.2: Optical microscope images of thin films deposited for the study with unannealed films (a), (b) and (c) deposited at 25^0C, 250^0C and 700^0C and 30 minute annealed films (d), (e) and (f) deposited at the same temperatures respectively

turned to a dull brown to a dull brownish-grey shade, with this colour intensifying

as the period of post growth anneal increased to 2h. The films also appeared visibly smoother visually, and when observed under the microscope. This trend was similar for films grown at 250^0C and 700^0C, where the films appeared smoother with lesser particulates on the film with a longer post growth anneal as compared to the samples before annealing. This could be explained by the conversion of metal particulates into oxide materials as the growth temperature increases, and the post growth anneal period increases. A comparison of these images can be found in the Figure 6.2.

6.1.3 X-Ray Diffraction studies

Figure 6.3 presents the thin film Glancing angle XRD (GIXRD) of the LCFCr target with a glancing angle of 5^0 and a 2θ scan from 25^0 to 65^0. Sharp peaks corresponding to crystal orientations of (121)/(002), (022), (040)/(202), (042)/(123) and (242)/(004) can be observed. From this study, XRD measurements of the LCFCr thin films were performed, with 2θ peaks expected from these peaks observed in the XRD scan of the LCFCr target.

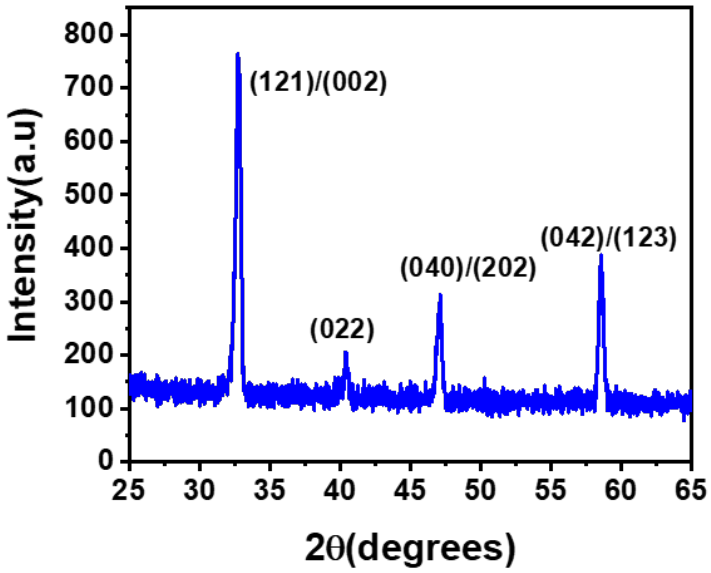

Figure 6.3: GIXRD and peaks of the LCFCr target corresponding to crystal orientations of (121)/(002), (022), (040)/(202), (042)/(123) and (242)/(004)

XRD studies were performed for all the thin film samples listed in the table with a glancing angle of 1^0 on three XRD tools, namely Bruker Discover D8 tool and Rigaku Ultima IV tools in Nanofab and NRC Discover D8 tool in NINT.

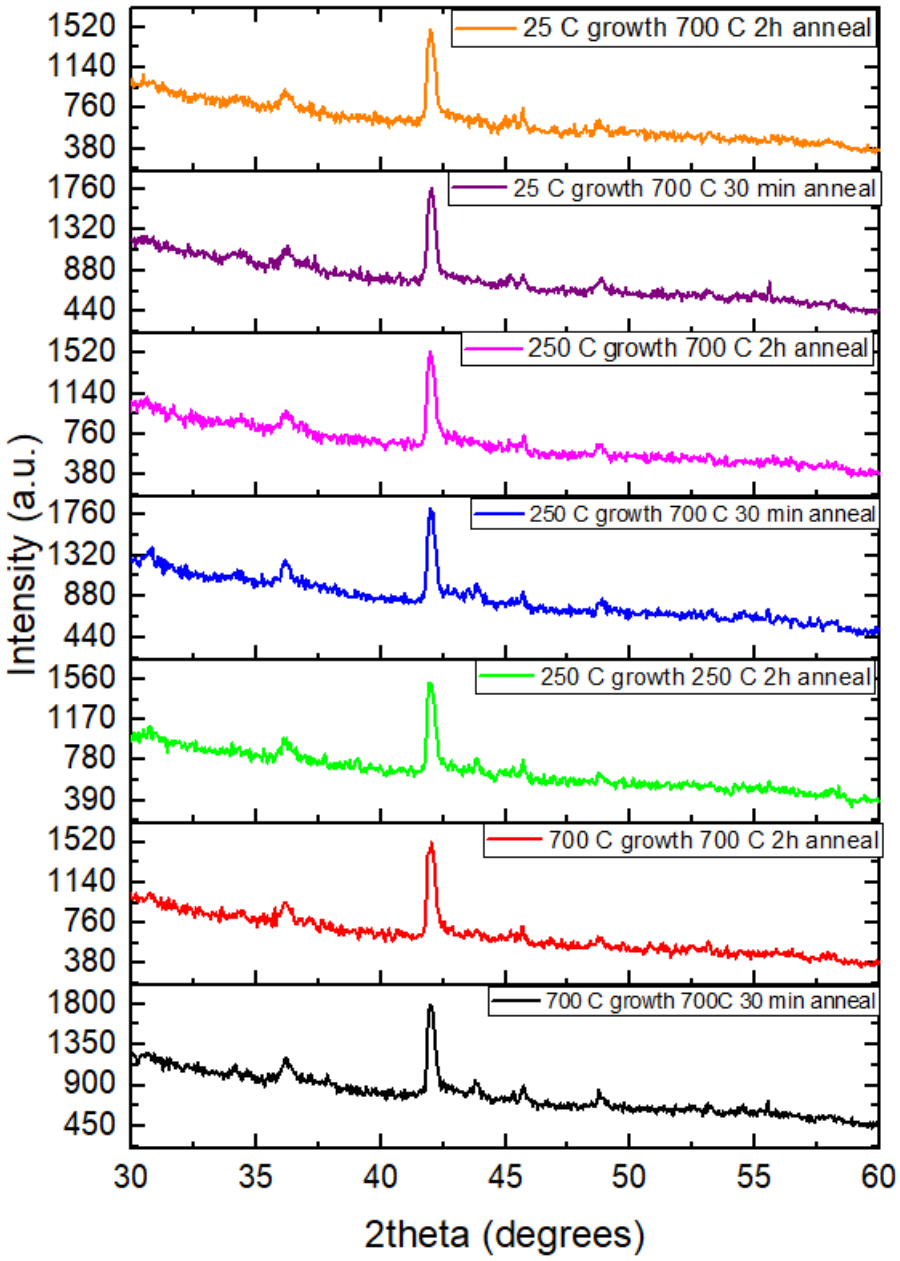

Figure 6.4: GIXRD plots of LCFCr thin films over a 2θ range of 30^0 to 60^0 for samples 25-30mA, 25-2hA, 250-30mA, 250-2hA, 700-30mA and 700-2hA,

On measuring the three unannealed samples, namely, 25-U, 250-U and 700-U, on both Rigaku Ultima IV and Bruker Discover D8 tool, it was observed that none of these samples exhibited any peaks between the 2θ ranges of 30^0 to 70^0. When measured on Bruker Discover D8 tool with a glancing angle of 1^0, from Figure 6.4, it can be seen that with a 30 min anneal, samples grown at all three temperatures, namely 25^0C, 250^0C and 700^0C (samples 25-30mA, 250-30mA and 700-30mA respectively) showed a sharp peak at 42.03^0 which may correspond to (022) configuration of LCFCr. With increase in growth temperature, a reduction in FWHM of the peak was observed from 0.38^0, 0.35^0 and 0.33^0 for samples 25-30mA, 250-30mA and 700-30mA respectively.

On annealing these samples further for upto 2 hours, a reduction in FWHM of the (022) peak of the thin films was observed to be 0.35^0, 0.34^0 and 0.34^0 for samples 25-2hA, 250-2hA and 700-2hA respectively, implying a higher crystallinity with a larger post growth anneal period. The 2θ positions remained the same at around 42.01^0 for samples 25-2hA and 250-2hA and 42.03^0 for sample 700-2hA. For samples grown at 250^0C and 700^0C, there is not a significant reduction in FWHM with higher post growth anneal periods, as observed from the Table 6.1. These peaks corresponded to the crystal orientation of (022) configuration of LCFCr as seen from Figure 6.3.

When these samples were measured on the Rigaku Ultima IV tool with a glancing angle of 0.5^0, the unannealed samples (25-U, 250-U and 700-U) did not show any peaks, while the annealed samples grown at 250^0C showed peaks at 44.6^0 and 44.4^0 with FWHM 0.65^0 and 0.60^0 for samples 250-30mA and 250-2hA respectively. Samples grown at 700^0C showed peaks at 44.6^0 and 44.4^0 with FWHM 0.68^0 and 0.56^0 for samples 700-30mA and 700-2hA respectively. These peaks correspond to the (040)/(202) peak of LCFCr as seen in Figure 6.3. The shifting of the peak position with instrument was anomalous and could not be explained. Therefore, a third instrument, NRC Discover D8 was employed to obtain a 2D scan of sample 700-30mA.

With an grazing incident angle of 1^0, no peaks were obtained between 2θ values ranging from 30^0 to 65^0. From Figures 6.6(b), it can be seen that the 2D scans at an incident angle of 20^0 showed a sharp single crystalline peak at 40.08^0 with a

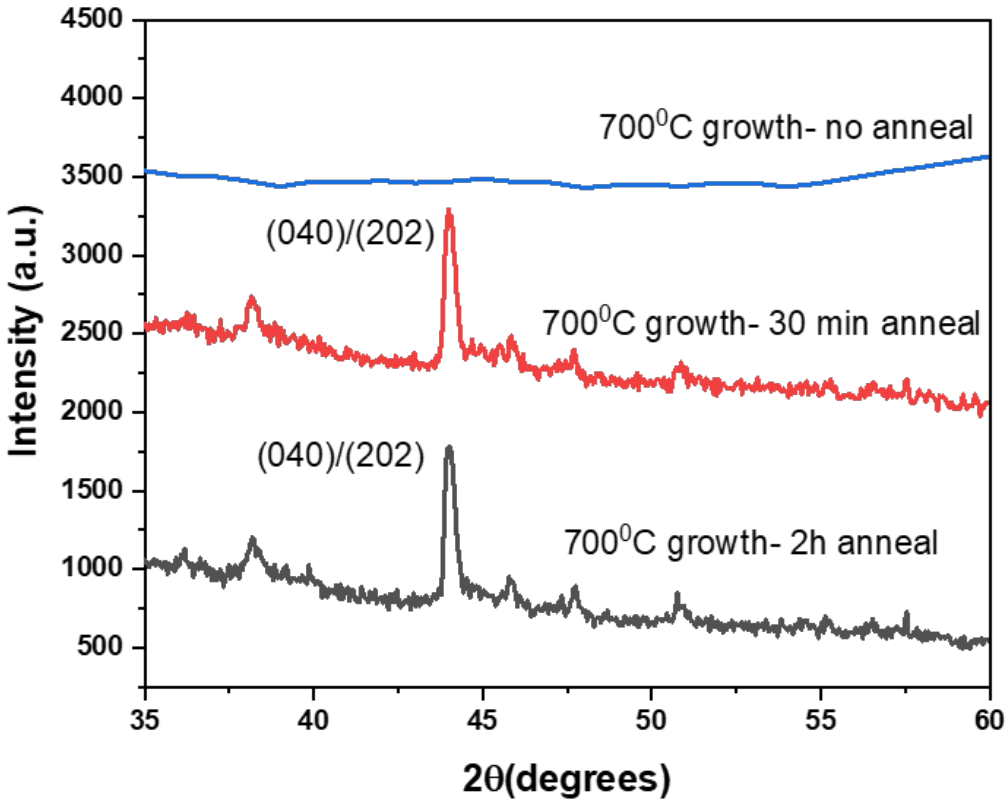

Figure 6.5: GIXRD and peaks of the LCFCr thin films corresponding to samples 700-U, 700-30mA and 700-2hA corresponding to crystal orientations of (040)/(202) measured on Rigaku Ultima IV.

FWHM of 0.13^0 corresponding to (022) orientation of LCFCr, with a diffused peak shown corresponding to the YSZ (001) peak at around 35^0. The 1D scan corresponding to a horizontal slice of the 2D scan as shown in Figure 6.6 (a) shows these peaks clearly. With an incident angle of 22.2^0,a sharp single crystalline peak at 44.46^0 with a FWHM of 0.13^0 corresponding to (040)/(202) orientation of LCFCr, with a diffused peak shown corresponding to the YSZ (001) peak at around 35^0 can be seen. The presence of both these peaks at different incident angles suggests the presence of both these orientations, however, due to the differences in peaks obtained across all these three tools, the crystal orientation of the thin film was sought to be measured from the TEM diffraction studies.

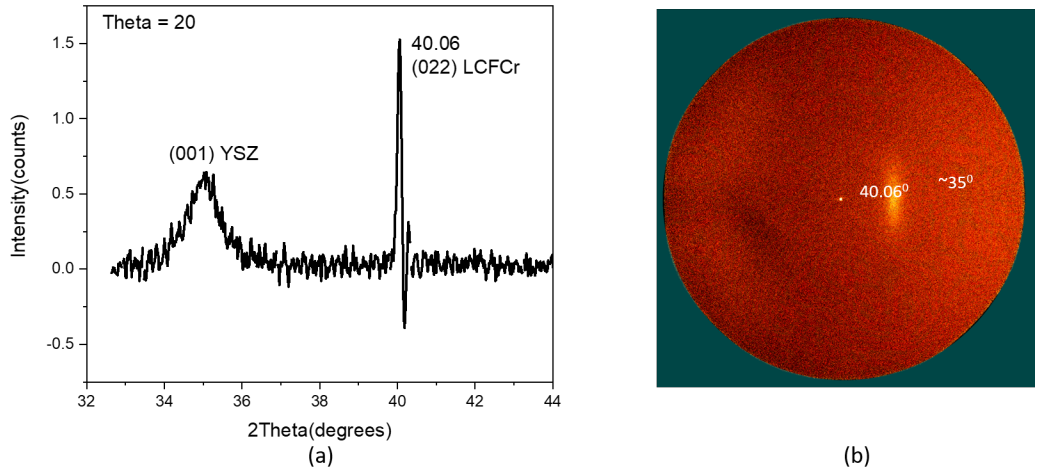

Figure 6.6: GIXRD 2D scan and peaks of the LCFCr thin films corresponding to sample 700-30mA as measured on NRC Discover D8 with incident angle 20^0 with (a) the 1D scan and (b) the corresponding 2D scan showing the YSZ peak at around 35^0.

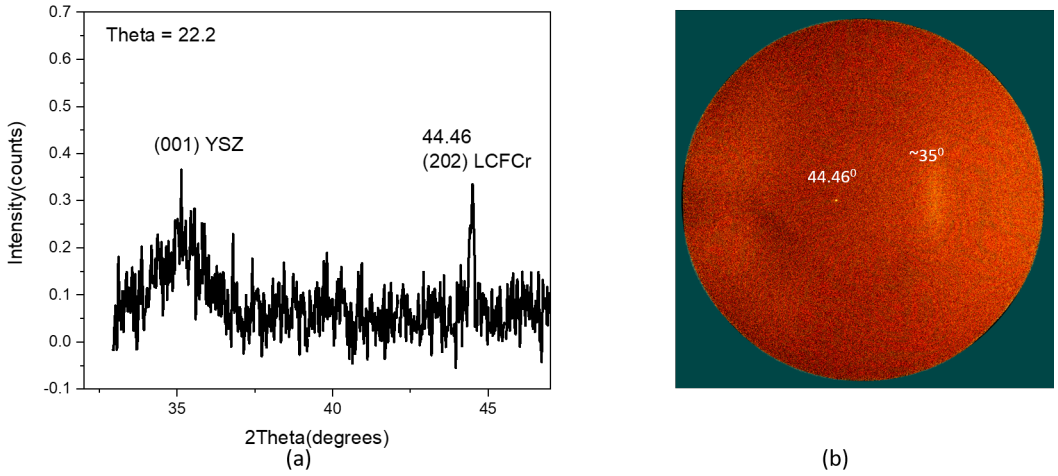

Figure 6.7: GIXRD 2D scan and peaks of the LCFCr thin films corresponding to sample 700-30mA as measured on NRC Discover D8 with incident angle 22.2^0 with (a) the 1D scan and (b) the corresponding 2D scan showing the YSZ peak at around 35^0.

Sample	2θ peak (^{0}) (Bruker D8)	FWHM of XRD peak (^{0}) (Bruker D8)	2θ peak (^{0}) (Rigaku)	FWHM of XRD peak (^{0}) (Rigaku)	2θ peak (^{0}) (NRC D8)	FWHM of XRD peak (^{0}) (NRC D8)
25-U	-	-	-	-	-	-
25-30mA	42.03	0.38	44.6	0.72	N/A	N/A
25-2hA	42.01	0.35	44.4	0.68	N/A	N/A
250-U	-	-	-	-	-	-
250-30mA	42.03	0.35	44.6	0.65	N/A	N/A-
250-2hA	42.01	0.34	44.4	0.60	N/A	N/A
700-U	-	-	-	-	-	-
700-30mA	42.03	0.33	44.6	0.68	40.08 and 44.46	0.13 and 0.13
700-2hA	42.03	0.33	44.4	0.56	N/A	N/A

Table 6.2: XRD results of LCFCr grown at 25^0C, 250^0C and 700^0C with different post anneal conditions- no anneal, 30 min anneal at 700^0C and 2h anneal with XRD results obtained using Bruker Discover D8, Rigaku Ultima IV and NRC Discover D8

6.1.4 Atomic force microscopy studies

Bruker Dimension Edge Atomic Force Microscope was used to image the morphology of as-grown LCFCr and LSFCr thin films. AFM imaging was performed to image the grains and to analyse film properties such as roughness, continuity and grain size. RMS roughness and particle size properties were extracted from NanoscopeAnalysis software. In Figure 6.8, an AFM scan of 25^0C grown sample annealed at 700^0C for 2 hours (sample 25-2hA)is presented. Samples 25-U and 25-30mA were unable to be imaged due to high variation in height because of the particulate clusters present on the thin film. These scans were not able to be performed to image the grain boundaries or particle sizes effectively.

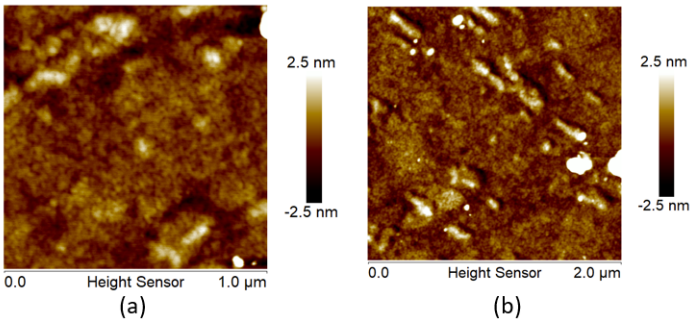

Figure 6.8: AFM scans over 1 μm^{2}and 2 μm^2 regions of room temperature grown LCFCr annealed for 30 min at 700^0C (sample 25-30mA)

Figure 6.9 shows the AFM scans for samples 250-U and 250-30mA over 1 μm^2 and 2 μm^2 areas. From Figure 6.9, it can be observed that with an increase in substrate

temperature and post growth anneal, the film appears to be a lot more continuous and uniform as seen in the figure below, where a 250^0C grown sample before and after a 30 minute 700^0C anneal period can be observed. For the sample 25-U, the scans in Figure 6.9 (a) and (b), the RMS roughness obtained were 1.33 and 1.43, indicating a high roughness of the surface. Visually, large particulate chunks can be observed on the thin film. The scan did not show clear particles, and therefore, particle analysis was unable to be performed.

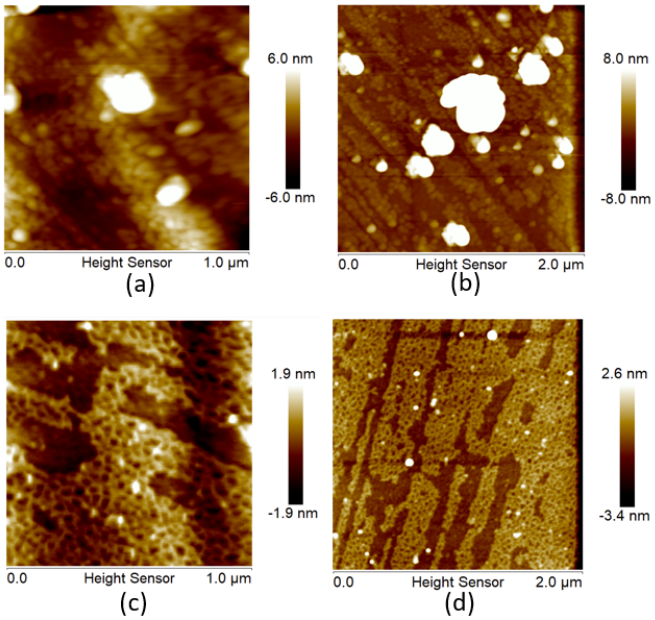

Figure 6.9: AFM scans over 1 μm^2 and 2 μm^2 regions respectively of (a) (RMS roughness 1.33 nm) and (b) (RMS roughness 1.43 nm) : 250-U and (c)(RMS roughness 0.61 nm) and (d) (RMS roughness 0.82 nm): 250-30mA

For samples 700-U and 700-30mA, clearer grains and particles were able to be imaged as seen in Figure 6.10. In order to compare the surface morphology of these films before and after post growth anneal, particle analysis was performed. From the figure, a film grown at 700^0C with a post growth anneal of 30 minutes (700-30mA), shows an RMS roughness of 0.15 nm. Compared to this, an unannealed sample grown at 700^0C (700-U) appeared more discontinuous with an RMS roughness measured to be 1.21 nm. It can be observed that with higher substrate growth temperatures, the RMS roughness of the film also reduces to give a smoother film, as evident from the comparison of the film sample 250-30mA in Figure 6.9 (c),

which has an RMS roughness of 0.61 nm.

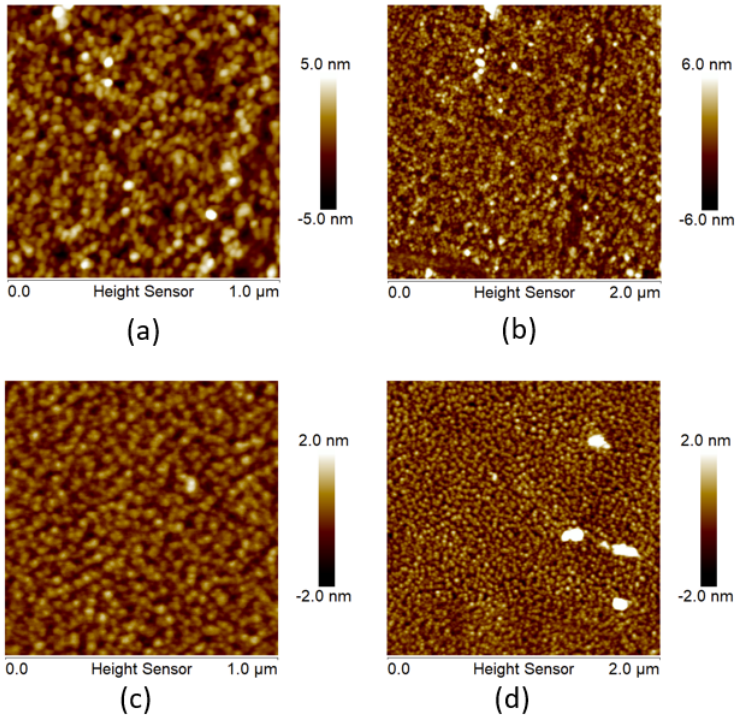

Figure 6.10: AFM scans over 1 μm^2 and 2 μm^2 regions respectively of (a) (RMS roughness 1.21 nm) and (b) (RMS roughness 1.26 nm) : 700-U and (c)(RMS roughness 0.15 nm) and (d) (RMS roughness 0.22 nm): 700-30mA

The grain particles from the samples 700-U and 700-30mA were analyzed, and it was observed that for the sample without anneal, the diameter of the grains varied from 11 nm to 78 nm, with an average particle diameter of 28 nm. The height variation of the grains ranged from 1.9 nm to 7.5 nm. For the sample after post growth anneal, it was observed that the particle diameter ranged from 11 nm to 96 nm, with an average particle diameter of 33 nm. The height variation of the grains ranged from 0.38 nm to 1.8 nm, which shows that after anneal, the film was a lot smoother and more uniform. On comparing the distribution of the particle diameters, a larger number of particles were found with diameters between 20 – 40 nm for the sample post anneal, whereas before anneal, the particle diameters of most of the particles varied between 11 – 25 nm, which demonstrates that the grain size increases after post growth anneal. This indicates an improved crystallinity, which is also matched by the reduction in FWHM observed after post growth

anneal in the XRD analysis discussed. A summary of the results obtained by the AFM studies has been presented in Table 6.3.

Sample	**RMS roughness (nm)**	**Average particle size (nm)**	**Height variation. of particles (nm)**	**Size of largest particulates (nm)**
250-U	1.33	-	-	387
250-30mA	0.61	-	-	98
700-U	1.21	28	1.9-7.5	78
700-30mA	0.15	33	0.38-1.8	96

Table 6.3: Table of extracted properties from AFM scans of LCFCr thin films grown at different substrate temperatures and post growth anneal conditions.

6.1.5 X-ray photoelectron spectroscopy studies

Room temperature elemental analysis of the LCFCr thin films was performed at nanoFAB using Kratos Axis spectrometer. The spectrometer was calibrated by the binding energy (84.0 eV) of Au4f7/2with reference to Fermi level. The pressure of measurement chamber during experiment was around 5×10^{-10} Torr. Charge effects were corrected by using the Carbon 1s peak at 284.8 eV and the peaks were analysed using CasaXPS software. XPS analysis was performed on all the samples described above to understand the elemental composition of the thin films in more detail. XPS analysis of LCFCr thin films grown at 25^0C, 250^0C, and 700^0C before anneal and the after a post growth anneal at 700^0C were subjected to elemental XPS analysis.

In all the samples (25-U, 25-30mA, 250-U, 250-30mA, 700-U and 700-30mA), the peaks corresponding to La 3d, Ca 2p, Fe 2p and Cr 2p were found to be present. In the samples grown at 25^0C and 250^0C (25-U, 25-30mA, 250-U and 250-30mA), the presence of the metals was suggested to be much lower than that for 700^0C grown samples (700-U and 700-30mA) based on the intensity of the peaks as all of the measurements were performed on the same tool at the same time. The 25^0C grown samples (25-U and 25-30mA) showed only a oxygen 1s peak, which indicates that very little oxide formation was observed. This can be observed in Figure 6.11.

In Figure 6.11, It can be observed that the dual peaks dual peaks corresponding to La-$3d^{3/2}$ at 851.71 eV and 855.57 eV and La-$3d^{5/2}$ at 834.82 eV and 838.64

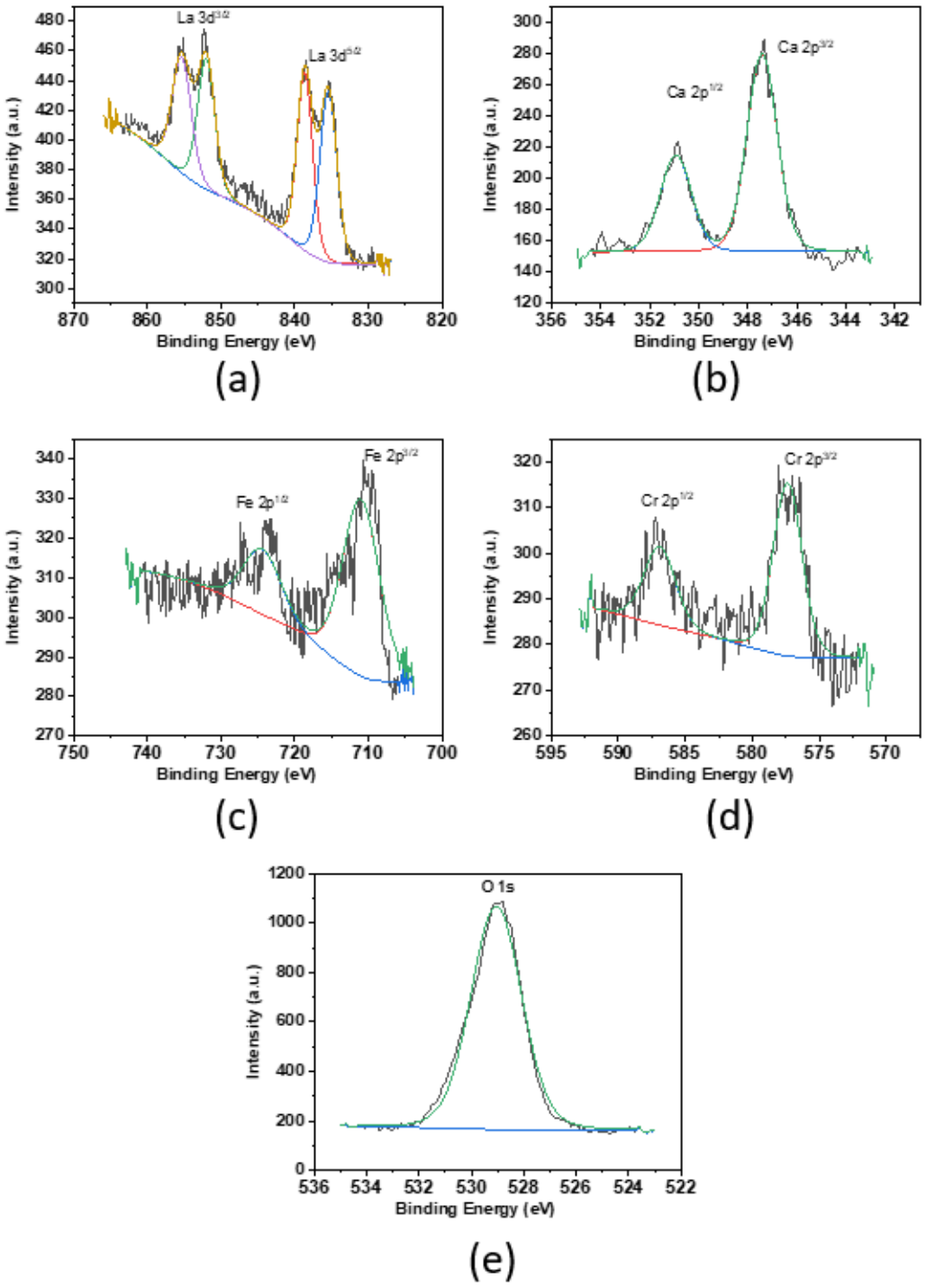

Figure 6.11: XPS scans showing the elemental states of (a) La, (b) Ca, (c) Fe, (d) Cr and (e) O in LCFCr grown at 25^0C without anneal

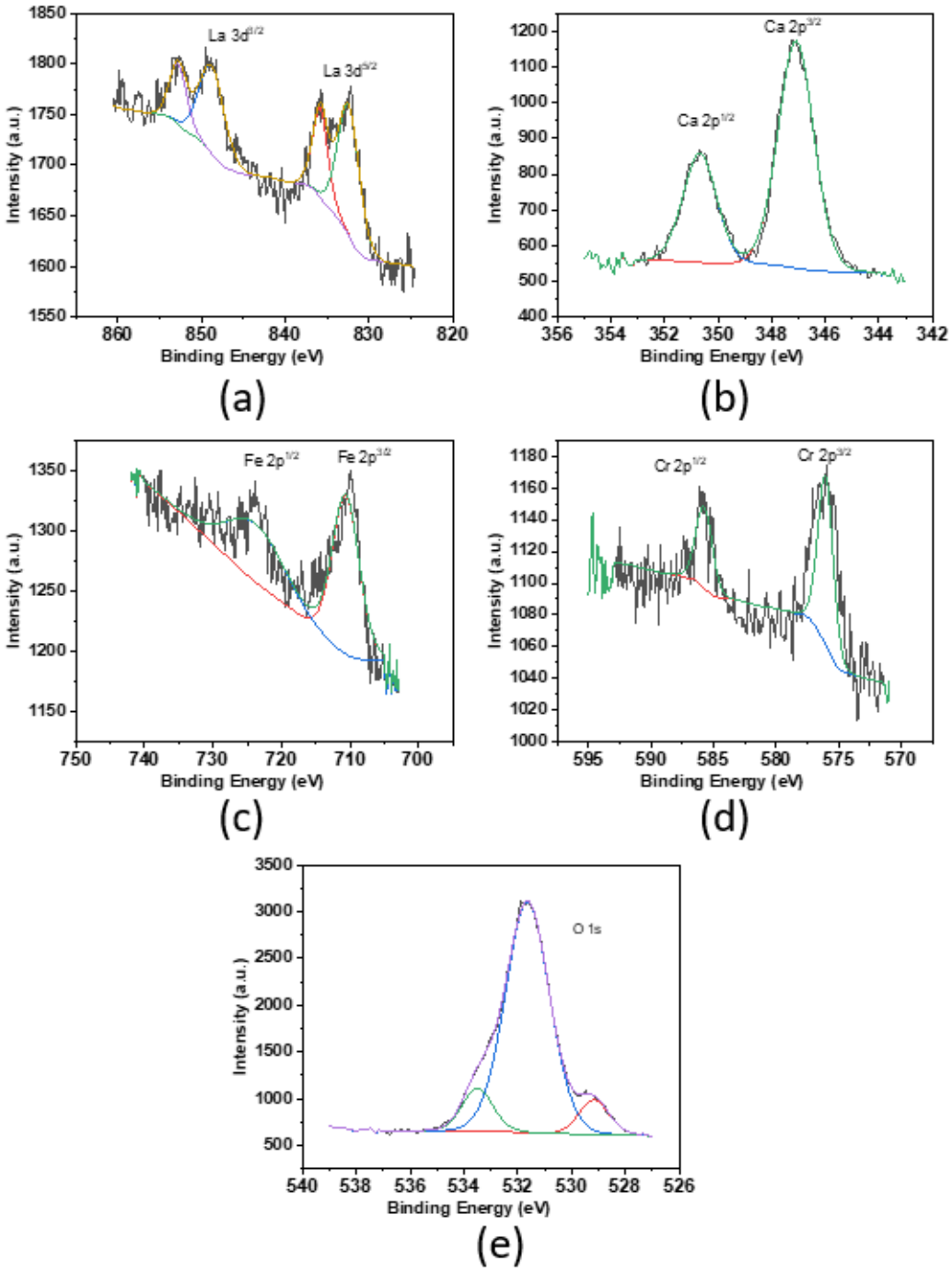

Figure 6.12: XPS scans showing the elemental states of (a) La, (b) Ca, (c) Fe, (d) Cr and (e) O in LCFCr grown at 700^0C without anneal (sample 700-U)

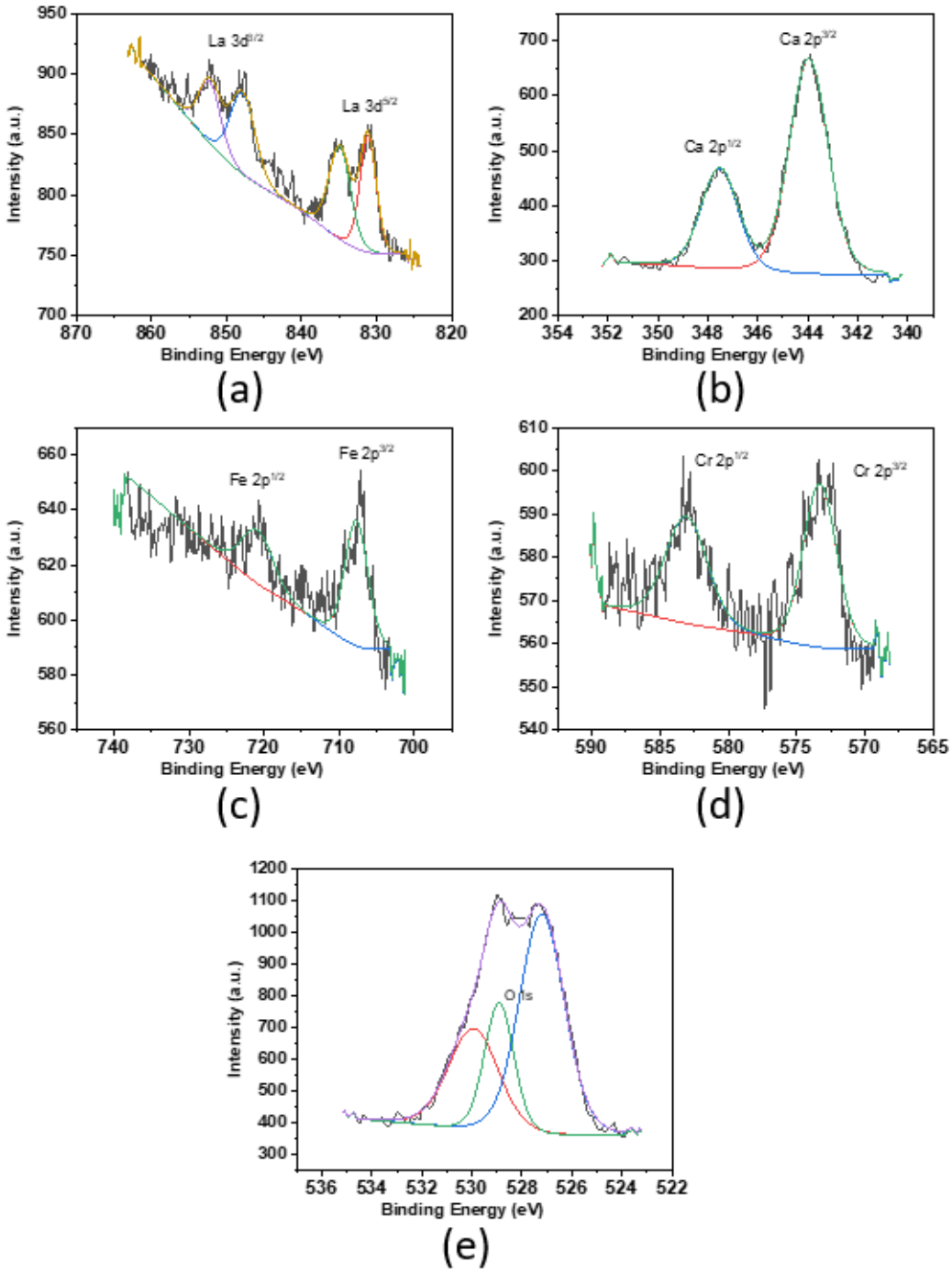

Figure 6.13: XPS scans showing the elemental states of (a) La, (b) Ca, (c) Fe, (d) Cr and (e) O in LCFCr grown at 700^0C with a 30 minute anneal (sample 700-30mA)

eV were observed for La, while Ca-$2p^{1/2}$and Ca-$2p^{3/2}$ were observed at 351.21 eV and 347.45 eV respectively. Fe-$2p^{1/2}$ and Fe-$2p^{3/2}$ were obtained at 724.82 eV and 711.81 eV respectively and Cr-$2p^{1/2}$ and Cr-$2p^{3/2}$ peaks were obtained at 586.81 eV and 577.12 eV, as confirmed from literature [104; 105; 106; 107]. However, the single oxygen 1s peak at 529.9 eV suggests the absence of oxide formation.

As seen in Figure 6.12, in the 700^0C grown sample without anneal (700-U), dual peaks corresponding to La-$3d^{3/2}$ at 851.53 eV and 854.32 eV and La-$3d^{5/2}$ at 833.12 eV and 837.91 eV were observed for La, while Ca-$2p^{1/2}$and Ca-$2p^{3/2}$ were observed at 350.91 eV and 347.75 eV respectively. Fe-$2p^{1/2}$ and Fe-$2p^{3/2}$ were obtained at 725.11 eV and 711.52 eV respectively and Cr-$2p^{1/2}$ and Cr-$2p^{3/2}$ peaks were obtained at 586.75 eV and 576.45 eV, as confirmed from literature [104; 105; 106; 107]. The oxygen 1s peak is observed at 529.08 eV, along with indications of presence of chromium and iron oxides as predicted from literature at 531.42 eV and 533.07 eV [108; 109].

The 700^0C grown sample following a post growth anneal at 700^0C (700-30mA) shows all the peaks for the metals listed above. dual peaks corresponding to La-$3d^{3/2}$ at 851.31 eV and 854.64 eV and La-$3d^{5/2}$ at 833.23 eV and 837.13 eV were observed for La, while Ca-$2p^{1/2}$and Ca-$2p^{3/2}$ were observed at 350.11 eV and 347.59 eV respectively. Fe-$2p^{1/2}$ and Fe-$2p^{3/2}$ were obtained at 725.19 eV and 711.76 eV respectively and Cr-$2p^{1/2}$ and Cr-$2p^{3/2}$ peaks were obtained at 586.71 eV and 576.15 eV, as confirmed from literature [104; 105; 106; 107]. The oxygen peaks in this sample also show the presence of nucleophilic oxygen (528.08 eV), along with the presence of 1s peak (529.9 eV) and oxides of Chromium (531.48 eV) as seen in Figure 6.13.

From the plots, the ratio of the amount of oxygen 1s present compared to the oxide peaks was obtained by taking the ratio of the peak areas as fitted to the curve using CasaXPS software. A summary of these peaks and positions have been shown below in Table 6.4. It can be seen that while the elemental states of the metals are present as expected, there are different types of oxides present in the films, which are present in different ratios when compared to 1s oxygen. Multiple XPS measurements of these samples would help in improving our understanding of the oxides present in these samples.

Sample	Elemental states present	Peak position (eV)	Ratio of O-1s to other oxides
25-U	La $3d^{3/2}$	851.71 and 855.57	1:0
	La $3d^{5/2}$	834.82 and 838.64	
	Ca $2p^{1/2}$ and Ca $2p^{3/2}$	351.21 and 347.45	
	Fe $2p^{1/2}$ and Fe $2p^{3/2}$	724.82 and 711.81	
	Cr $2p^{1/2}$ and Cr $2p^{3/2}$	586.81 and 577.12	
	O 1s and O-oxides	529.9 and 0	
700-U	La $3d^{3/2}$	851.53 and 854.32	1:2.07
	La $3d^{5/2}$	833.12 and 837.91	
	Ca $2p^{1/2}$ and Ca $2p^{3/2}$	350.91 and 347.75	
	Fe $2p^{1/2}$ and Fe $2p^{3/2}$	725.11 and 711.52	
	Cr $2p^{1/2}$ and Cr $2p^{3/2}$	586.75 and 576.45	
	O 1s and O-oxides	529.08 and (531.42, 533.07)	
700-30mA	La $3d^{3/2}$	851.31 and 854.64	1:1.11
	La $3d^{5/2}$	833.23 and 837.13	
	Ca $2p^{1/2}$ and Ca $2p^{3/2}$	350.11 and 347.59	
	Fe $2p^{1/2}$ and Fe $2p^{3/2}$	725.19 and 711.76	
	Cr $2p^{1/2}$ and Cr $2p^{3/2}$	586.71 and 576.15	
	O 1s and O-oxides	529.9 and (531.48, 528.08)	

Table 6.4: Table of extracted elemental states of La, Ca, Fe and Cr present in the samples measured by XPS with peak positions corresponding to the elemental states and ratio of areas of oxygen 1s peak to the other oxides

6.1.6 Transmission electron Microscopy studies

TEM imaging was performed by Dr. Hui Yuan, CCEM at the McMaster University. The sample imaged was 700-30mA, which was grown at 700^0C and annealed for 30 minutes at 700^0C. A 25 μm sized thin slice of as deposited film on YSZ crystal was selected, and the interface of the LCFCr thin film and YSZ substrate was imaged as shown in Figure 6.14.

From the TEM studies, it was observed that the thickness of the LCFCr thin films was around 50 nm. From Figure 6.14 (a), it can be seen that the YSZ substrate has a very clear crystal orientation parallel to the horizontal surface, and the thin film has grown on top of it in an an epitaxial manner. Based on the highly epitaxial nature of the TEM image shown in Figure 6.14, it can be concluded that PLD was successful in being able to achieve smooth, uniform and highly crystalline epitaxially grown thin films for SOEC electrochemical tests, which would constitute the next stage of experiments. From the diffraction patterns, it was seen that the YSZ possessed a (001) crystal orientation, as was expected. Further, the thin film was shown to have two possible phases, one being (002) and (100.25), the latter being

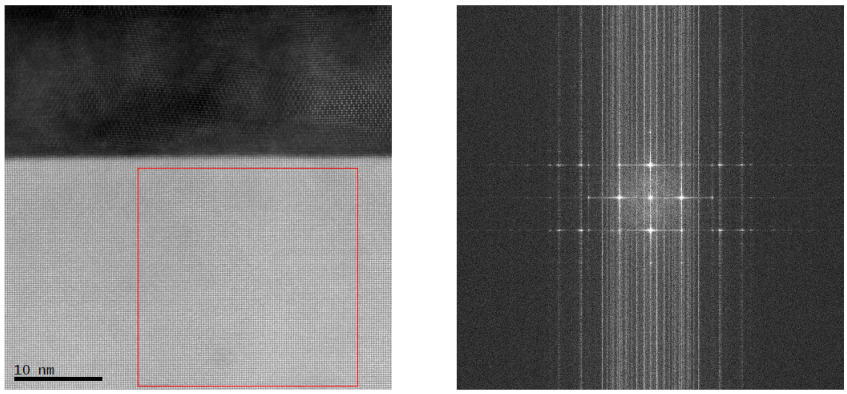

Figure 6.14: (a) TEM image of the interface of LCFCr and YSZ substrate along with (b) the diffraction pattern of the substrate to show a 001 orientation

a forbidden phase.

Based on the three different peaks obtained by XRD studies on three different instruments, and the crystal phase obtained by the TEM studies, further investigation into the crystal orientation(s) present in the thin film is sought to be performed to understand the origin of this disparity in measurements.

6.2 Optimization and growth of LSFCr

Preliminary studies of the pulsed laser depositions of LSFCr was performed using the LSFCr target prepared by the Birss group at the University of Calgary .The target was prepared with LSFCr powders prepared by glycine combustion method. They were cold-pressed into pellets (1 inch in diameter) and sintered at 1300 – 1400 ^{0} C in air. The laser used for the ablation was a KrF excimer laser (248 nm, 15 ns, 5 Hz). A chamber base pressure of $1x10^{-5}$ to $7x10^{-6}$ T was obtained for all of the growths. Samples were grown at 700^0C in a gas ambience of 40-50 mT of oxygen with a laser fluence of 3 J/cm^2 on the target and a substrate – target distance of 3 cm under two post growth anneal conditions, without anneal, and with 30 min anneal at 700^0C. A summary of these growths is listed in Table 6.5.

Sample	Growth Temp. (^{0}C)	Post growth anneal period at 700^{0}C (min)	XRD peak $2\theta(^0)$	FWHM of XRD peak (^{0})	RMS roughness (nm)
S-700-U	700	0	42.01	0.38	0.17
S-700-30mA	700	30	42.03	0.36	0.12

Table 6.5: Samples of LSFCr grown at 700^{0}C with different post anneal conditions- no anneal and 30 min anneal with XRD results obtained using Bruker Discover D8 and RMS roughness corresponding to the samples

6.2.1 X-Ray Diffraction studies

Figure 6.15 shows GIXRD performed for the LSFCr target with a glancing angle of 1^0 on Bruker Discover D8 tool. From the figure we can observe that the peaks corresponding to crystal orientations of (121)/(002), (022), (040)/(202), (042)/(123) and (242)/(004) can be observed on the target.

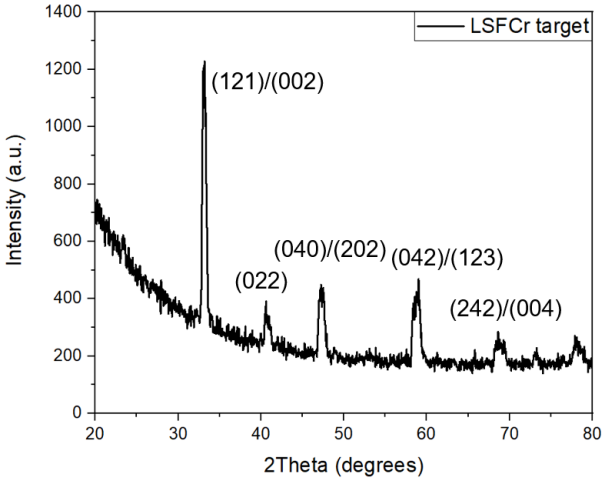

Figure 6.15: XRD peaks of LSFCr target

Thin film Glancing angle XRD (GIXRD) studies were performed for the samples listed in the table with a glancing angle of 1 degree on Bruker Discover D8 tool as shown in Figure 6.16. Measurements of thin films grown at 700^{0}C, with and without a post growth anneal of 30 min (samples S-700-U and S-700-30mA respectively) were performed. Both the samples showed a sharp peak at around 42.01^0 and 42.03^0 respectively with FWHM reducing from 0.38^0 to 0.36^0 respectively, which may correspond to (022) configuration of LSFCr. The improved crystallinity can also be correlated with the higher uniformity of grain size as observed from the AFM studies presented in the next section.

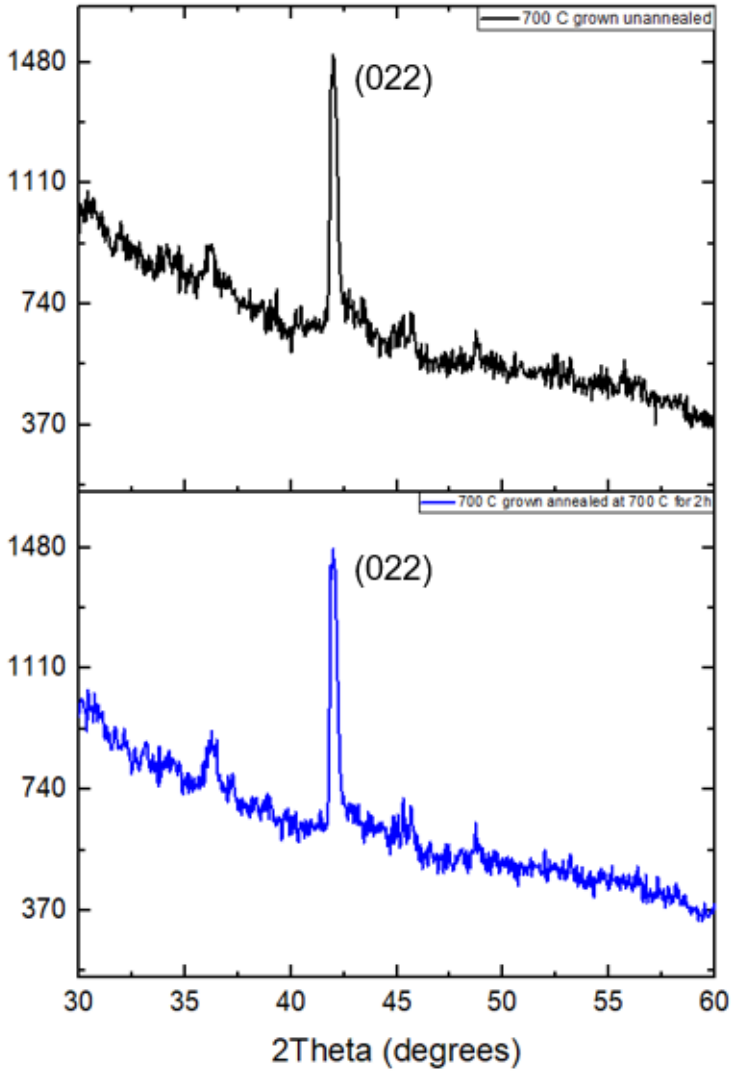

Figure 6.16: XRD peaks of LSFCr thin films measured over the sample grown at 700^0C (a) without post growth anneal (sample S-700-U) and (b) annealed at 700^0C (sample S-700-30mA)

6.2.2 Atomic force microscopy studies

AFM imaging was performed to image the grains and to analyse film properties such as roughness, continuity and grain size. In Figure 6.17, an AFM scan of 700^0C grown sample with and without 30 min post growth anneal at 700^0C is presented (samples S-700-U and S-700-30mA respectively).

From Figure 6.17, it can be observed that the unannealed sample has smooth surface with an RMS roughness of 0.17 nm, which is much lower than that of

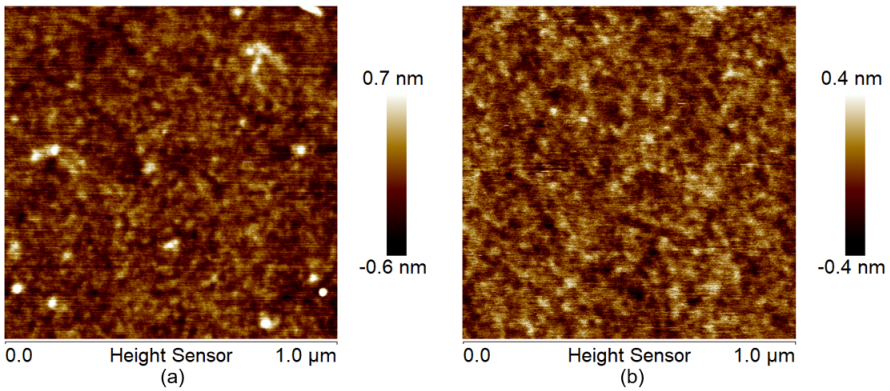

Figure 6.17: AFM scans over a 1 μm^2 area of a sample grown at 700^0C (a) without post growth anneal as sample S-700-U (RMS roughness 0.17 nm) and (b) annealed at 700^0C as sample S-700-30mA (RMS roughness 0.12 nm)

LCFCr under the same conditions (1.21 nm). This could explain the presence of an XRD peak for the unannealed sample, implying that a lower growth temperature with anneal would also work to form crystalline thin films of LSFCr on YSZ. The annealed LSFCr sample showed a lower RMS roughness of 0.12 nm, suggesting an improved surface uniformity and smoothness along with a better crystallinity with the annealing. This calls for future studies with lower temperature growths with longer post growth anneals to enable the same smoothness, uniformity and crystallinity, which can be optimized in the future.

6.2.3 X-ray photoelectron spectroscopy studies

The 700^0C grown sample without a post growth anneal (sample S-700-U) shows all the metallic peaks expected. Dual peaks dual peaks corresponding to La-$3d^{3/2}$ at 851.22 eV and 854.12 eV and La-$3d^{5/2}$ at 833.41 eV and 837.82 eV were observed for La, while Sr-$3d^{3/2}$and Sr-$3d^{5/2}$ were observed at 135.47 eV and 133.23 eV respectively. Fe-$2p^{1/2}$ and Fe-$2p^{3/2}$ were obtained at 725.17 eV and 711.82 eV respectively and Cr-$2p^{1/2}$ and Cr-$2p^{3/2}$ peaks were obtained at 586.34 eV and 576.51 eV,, as confirmed from literature [109; 104; 105; 106; 107; 110]. Only one oxygen peak was observed, which could not correspond to 1s oxygen (530 eV). Based on the single oxygen 1s peak position at 530 eV, the peak here was obtained at 531.89 eV, which could correspond to oxides of Chromium. The same trend can be observed for the annealed sample.

The 700^0C grown sample with 30 min post growth anneal (sample S-700-30mA) also showed all the metallic peaks expected. Dual peaks dual peaks corresponding to La-$3d^{3/2}$ at 851.34 eV and 854.11 eV and La-$3d^{5/2}$ at 833.31 eV and 837.22 eV were observed for La, while Sr-$3d^{3/2}$and Sr-$3d^{5/2}$ were observed at 135.41 eV and 133.28 eV respectively. Fe-$2p^{1/2}$ and Fe-$2p^{3/2}$ were obtained at 725.11 eV and 711.80 eV respectively and Cr-$2p^{1/2}$ and Cr-$2p^{3/2}$ peaks were obtained at 586.24 eV and 576.21 eV,, as confirmed from literature [109; 104; 105; 106; 107; 110]. Only one oxygen peak was observed at 531.89 eV, which could correspond to oxides of Chromium.

Future tests such as PLD parameter optimization to produce smooth thin films at lower growth temperatures along with TEM could be performed to understand the nature of the material and compounds formed during this thin film deposition.

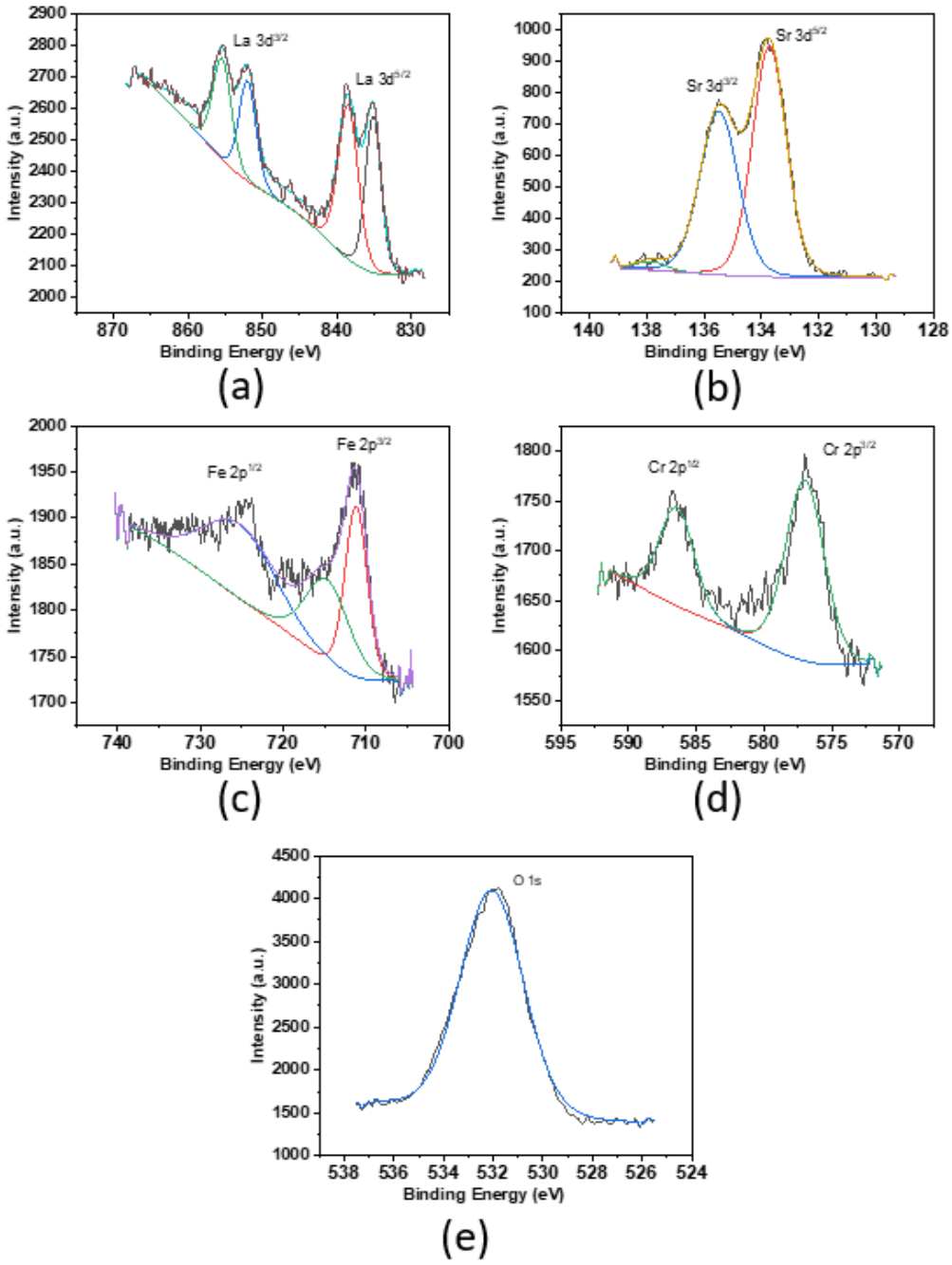

Figure 6.18: XPS scans showing the elemental states of (a) La, (b) Sr, (c) Fe, (d) Cr and (e) O in LSFCr grown at 700^0C without anneal (sample S-700-U)

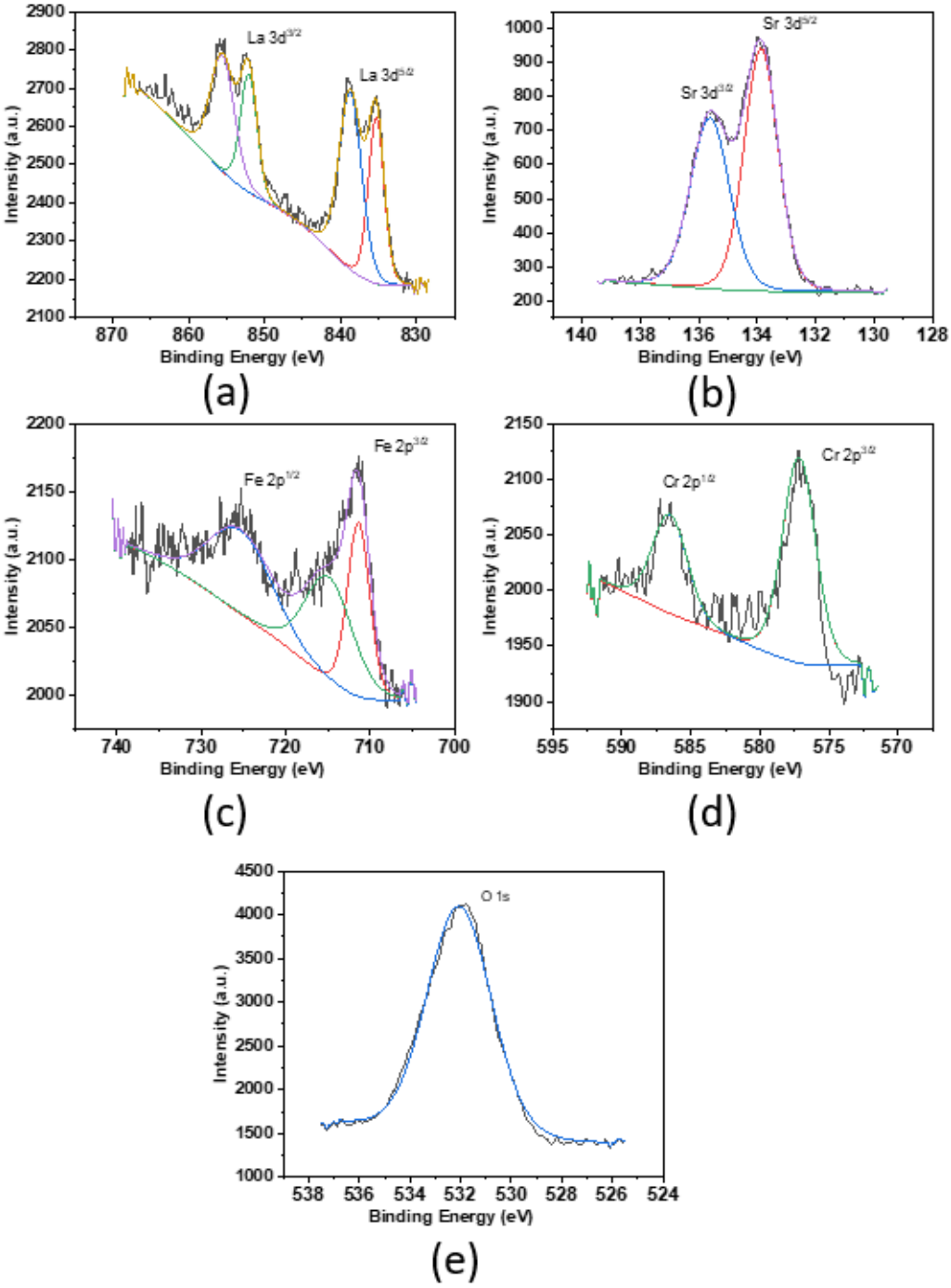

Figure 6.19: XPS scans showing the elemental states of (a) La, (b) Sr, (c) Fe, (d) Cr and (e) O in LSFCr grown at 700^0C with a 30 minute anneal (sample S-700-U)

6.3 Conclusions

In this study, pulsed laser deposition parameters such as laser fluence, ambient deposition pressure, substrate temperature and post growth anneal periods were varied, and optimized to obtain uniform and smooth thin films for SOEC applications. In particular, the study of variation of substrate temperature and post growth anneal periods have been focused on, and the film properties have been analysed using material characterization techniques such as AFM, XPS and XRD. The growth of LCFCr thin film has been optimized at a 700^0C growth with a post growth anneal of 30 min, as a significant increase in crystallinity and film roughness was not observed in the film a 2 hour post growth anneal. A laser fluence of 3.0 J/cm^2 was found to be above the ablation threshold of LCFCr, while a gas ambient pressure of 50-60 mT was found optimum for oxygen incorporation in the film without affecting growth rate. An optimum substrate – target distance of 3 cm was employed for all the growths to maximize growth rate. The optimized film showed an XRD peak corresponding to (022) configuration of LCFCr at 42.03 degrees with a peak FWHM of 0.33 degrees. RMS roughness of the grains was found to be 0.2 nm with an average particle diameter of 33 nm. XPS results showed the presence of all the metals in the film, with oxygen peaks corresponding to native oxygen 1s, chromium oxide and nucleophilic oxygen. LSFCr thin films grown at these optimized conditions at 700^0C with and without post growth anneal at 700^0C were studied. XRD peaks corresponding to (022) configuration was also observed for both the unannealed and annealed samples at 42.01 and 42.03 respectively. The RMS roughness of the thin films before and after anneal changed from 0.17 nm to 0.12 nm. The XPS results showed the presence of all the elemental states expected, however, no oxide formation was observed from the states of oxygen, which needs to be studied further. Future work would involve growth at lower temperatures with post growth anneal to obtain crystalline smooth films with a lower energy input.

Chapter 7

Conclusions and Summary

In this study, pulsed laser deposition of novel materials was performed and studied. This technique in particular, was studied for two very different kinds of materials, MoS_2, a 2D material for electronic device applications and LMFCr, a complex perovskite material for fuel cell applications. PLD provided unique advantages in both these cases, with an exploration into the benefits and challenges observed for these materials.

7.1 MoS_2

For the growth of MoS_2 thin films, conventional techniques posed certain disadvantages such as uncontrolled size and thickness of the film in the case of exfoliation and challenges associated with precursor gases, their disposal and limitations over substrates in the case of CVD. These issues were mitigated using PLD to obtain high quality epitaxial single crystal thin films with controlled film size over different substrates.

However, PLD came with its own set of challenges such as particulate formation and strains in the film with increased thickness of film. Optimized growth conditions of 800^0C growth with a 30 min post growth anneal at the growth temperature at a fluence of 2.2 J/cm^2 with a substrate target distance of 5 cm under a 0.5 mTorr Ar ambient were obtained from the PLD optimization study. Single crystal epitaxial growth was obtained with a crystal phase corresponding to (002) orientation

of MoS_2. A high uniformity with a film RMS roughness of around 0.17 nm was obtained for 5 monolayers of MoS_2. XPS analysis was used to observe a presence of small amounts of MoO_3 and semimetallic 1T-MoS_2 in the semiconducting 2H-MoS_2 thin films. Transmission and absorption studies over different thicknesses of the deposited films showed the presence of B and C excitonic transitions that was consistent with literature. TEM imaging of the thin film grown on a SiN_x membrane was performed to observe that the film was single crystalline despite the substrate not being lattice matched. This indicated high quality epitaxial growth of MoS_2 thin films made possible using PLD.

Hall measurements of the PLD grown MoS_2 thin films over various thicknesses indicated an n-type semiconductor behavior for MoS_2. An increasing trend in electron mobility was observed from 5 to 13 monolayers, and a decreasing trend was observed from 13 to 56 monolayers, with the highest mobility of 76.92 cm^2/Vs observed for 13 monolayers of MoS_2. This trend matched with that obtained by FET measurements over varying thicknesses observed in literature [92]. This was despite the size of our samples being around 25 mm^2, which allowed for a higher number of defects and vacancies in the film over this larger area. Multiple iterations of these measurements would help improve the accuracy of our measurements. Due to the high mobility achieved in these measurements despite the size of our samples, there is promise for higher mobilities in FET devices fabricated using PLD grown MoS_2 thin films in the future.

7.2 Future work in material growth and characterization

Future work includes working towards obtaining a precise layer by layer control over the growth of MoS_2 thin films. These films can also be grown to form heterostructures with other 2D materials such as WS_2 and h-BN. With h-BN behaving as insulators, semimetallic 2D materials such as TiS_2 behaving as semimetals, these heterostructures can potentially be used to fabricate 2D material based transistors. The PLD grown thin films can be used to fabricate MoS_2 based transistor devices and photodetectors integrated with traditional silicon electronics due to the stabil-

ity of MoS_2. Growth on flexible substrates can be attempted for device fabrication and integration in flexible and wearable sensors.

7.3 Future work in device simulation and fabrication

Preliminary simulation and fabrication work was performed on MoS_2 thin film based devices. There were several challenges faced by both the simulation and the fabrication studies.
As a new material parameter file for MoS_2 had to be created from scratch, future work in simulation studies would include processing of MoS_2 material models using additional literature review and by using software such as ATK-DFT to model fundamental properties and transport models. Improvements in the model by accounting for defects and contact issues within the simulation models may also help match the theoretic and experimental results. Expanding the simulation to transistor device modeling, along with being able to model the behavior of these devices with the change in number of monolayers in the thin film would be useful in enabling a better understanding of devices made using these novel materials.

On the fabrication front, There were several challenges faced during fabrication of these devices. One of the primary challenges was enabling a good contact between p-Si substrate and the MoS_2 thin film arising from the possibility of an oxide layer forming on the p-Si substrate before MoS_2 deposition. This could cause contact issues in the junction between the two materials. This challenge could be mitigated to some extent by using our new vacuum chamber with load lock to reduce the contamination, and hence, the oxidation of p-Si before the growth of MoS_2.

Usage of two different metals for the contacts of p-Si and MoS_2 could be worked upon by engaging in a two step lithography process, with Al used for p-Si and Au used for MoS_2 which could help improve the characteristics of the diode significantly.

There is a large scope for etching studies of large area multilayer MoS_2 thin films.

Etchants such as CCl_4 and $SF_6 + F_2$ may be useful in obtaining better results with MoS_2 etching, thereby allowing for a cleaner device isolation during the fabrication process. In addition, improvements to the lithography process and the adoption of two metal contacts for the heterostructure diode could help improve the device characteristics.

7.4 LMFCr

Pulsed laser deposition of LMFCr provided consistent and dense uniform smooth single crystal epitaxial thin films for application as electrode materials in electrochemical cells. PLD proved several advantages over traditional methods of deposition such as spin coating/dip coating + sintering which lead to highly porous, non uniform and inconsistent thin films.

PLD parameters such as laser fluence, ambient deposition pressure, substrate temperature and post growth anneal periods were varied, and optimized to obtain uniform and smooth thin films for SOEC applications at 700^0C growth at 3 J/cm^2 at 50-60 mT oxygen pressure, annealed for 30 minutes at 700^0C after growth. Under optimized growth conditions, epitaxial single crystal thin films of LCFCr with a (002) crystal phase was observed. A high film uniformity with the lowest RMS roughness of 0.15 nm obtained for LCFCr and 0.12 nm obtained for LSFCr was observed. XPS analysis helped study and confirm the elemental states present in the thin films.

There is a large scope for future work in the growth of LMFCr thin films using PLD. Some of the directions include usage of higher fluences for the growth and attempting lower temperature growths with longer post growth anneal periods to test the effect on the thin films. Further, different materials doped with the LMFCr such as Ni doped LMFCr can be used to study the behavior of the PLD on these materials. Using PLD to grow a buffer layer of GDC on the electrolyte material before the growth of LMFCr material for a better lattice matching can also be explored to see if that would improve the quality of the thin film. The performance of the thin films in electrochemical tests will be intensively studied.

Bibliography

[1] Hung-Chun Lin, Ming-Syuan Chen, and Yi-Hsin Lin. A Review of Electrically Tunable Focusing Liquid Crystal Lenses. *Transactions on Electrical and Electronic Materials*, 12(6):234–240, 2011.

[2] Gerard Cummins and Marc P.Y. Desmulliez. Inkjet printing of conductive materials: A review. *Circuit World*, 38(4):193–213, 2012.

[3] Jin Seong Park, Heeyeop Chae, Ho Kyoon Chung, and Sang In Lee. Thin film encapsulation for flexible AM-OLED: A review. *Semiconductor Science and Technology*, 26(3), Mar 2011.

[4] T. DebRoy, H. L. Wei, J. S. Zuback, T. Mukherjee, J. W. Elmer, J. O. Milewski, A. M. Beese, A. Wilson-Heid, A. De, and W. Zhang. Additive manufacturing of metallic components – Process, structure and properties. *Progress in Materials Science*, 92:112–224, Mar 2018.

[5] Anthony R. McAndrew, Paul A. Colegrove, Clement Bühr, Bertrand C.D. Flipo, and Achilleas Vairis. A literature review of Ti-6Al-4V linear friction welding. *Progress in Materials Science*, 92:225–257, Mar 2018.

[6] Kai Hua Liu, Hai Xia Zhong, Si Jia Li, Yan Xin Duan, Miao Miao Shi, Xin Bo Zhang, Jun Min Yan, and Qing Jiang. Advanced catalysts for sustainable hydrogen generation and storage via hydrogen evolution and carbon dioxide/nitrogen reduction reactions. *Progress in Materials Science*, 92:64–111, Mar 2018.

[7] T. Mukherjee, H. L. Wei, A. De, and T. DebRoy. Heat and fluid flow in additive manufacturing – Part II: Powder bed fusion of stainless steel, and

titanium, nickel and aluminum base alloys. *Computational Materials Science*, 150:369–380, Jul 2018.

[8] William D. Callister. *Material Science and Engineering, 7th ed*, volume 344. 2007.

[9] Matthew D. Eddy. *The Language of Mineralogy*. Routledge, Dec 2016.

[10] Joseph D. Martin. What's in a Name Change?: Solid State Physics, Condensed Matter Physics, and Materials Science. *Physics in Perspective*, 17(1):3–32, 2015.

[11] Donald L. (Donald Leonard) Smith. *Thin-film deposition : principles and practice*. New York : McGraw-Hill, international ed edition, 1995.

[12] R. Bunshah and C. Weissmantel. *Handbook of hard coatings, Deposition Technolgies, Properties and Applications*. Elsevier.

[13] Aaron D. Franklin. Nanomaterials in transistors: From high-performance to thin-film applications. *American Association for the Advancement of Science*, 349(6249), 2015.

[14] Krishna Seshan. *Handbook of Thin Film Deposition*. Elsevier, Jun 2012.

[15] K. Robbie and M. J. Brett. Sculptured thin films and glancing angle deposition: Growth mechanics and applications. *Journal of Vacuum Science & Technology A: Vacuum, Surfaces, and Films*, 15(3):1460–1465, May 1997.

[16] K. Matsubara, P. Fons, K. Iwata, A. Yamada, K. Sakurai, H. Tampo, and S. Niki. Zno transparent conducting films deposited by pulsed laser deposition for solar cell applications. *Proceedings of Symposium B, Thin Film Chalcogenide Photovoltaic Materials, E-MRS Spring Meeting*, 431-432:369 – 372, 2003.

[17] Spyridon Kassavetis, Christoforos Gravalidis, and Stergios Logothetidis. *Thin Film Deposition and Nanoscale Characterisation Techniques*. 2016.

[18] I. Johansen, R. Arntzen, S. Bergmann, S. Husa, K. A. Ingebrigtsen, J. S. Johannessen, and J. S. Sandved. Examples of thin film applications in electronic devices. *Thin Solid Films*, 50(C):171–185, May 1978.

[19] Pulickel Ajayan, Philip Kim, and Kaustav Banerjee. van der waals materials. *Physics today*, 69:9–38, 2016.

[20] Myung Gil Kim, Mercouri G. Kanatzidis, Antonio Facchetti, and Tobin J. Marks. Low-temperature fabrication of high-performance metal oxide thin-film electronics via combustion processing. *Nature Materials*, 10(5):382–388, 2011.

[21] L. Reindl, G. Scholl, T. Ostertag, C. C. W. Ruppel, W. . Bulst, and F. Seifert. Saw devices as wireless passive sensors. *1996 IEEE Ultrasonics Symposium. Proceedings*, 1:363–367 vol.1, Nov 1996.

[22] Abhishek Dhand, Srinidhi Suresh, Aman Jain, O Nilesh Varadan, M A K Kerawalla, and Prerna Goswami. Advances in Materials for Fuel Cell Technologies-A Review. Technical report, 2017.

[23] Douglas H. Lowndes, D. B. Geohegan, A. A. Puretzky, D. P. Norton, and C. M. Rouleau. Synthesis of novel thin-film materials by pulsed laser deposition. *American Association for the Advancement of Science*, 273(5277):898–903, 1996.

[24] Arun Suresh, Praveen Gollakota, Patrick Wellenius, Anuj Dhawan, and John F. Muth. Transparent, high mobility ingazno thin films deposited by pld. *Proceedings of Symposium R on Advances in Transparent Electronics:from materials to devices EMRS 2006 Conference, Nice, France*, 516(7):1326 – 1329, 2008.

[25] David Geohegan and Graham k. Hubler. *Pulsed Laser Deposition of Thin Films*. New York : J. Wiley, 1994.

[26] G. K Hubler and Douglas B Chrisey. *Pulsed laser deposition of thin films*. New York : J. Wiley, 1994.

[27] Y. Y. Tsui, H. Minami, D. Vick, and R. Fedosejevs. Debris reduction for copper and diamond-like carbon thin films produced by magnetically guided pulsed laser deposition. *Journal of Vacuum Science & Technology A*, 20(3):744–747, 2002.

[28] Hai Li, Jumiati Wu, Zongyou Yin, and Hua Zhang. Preparation and applications of mechanically exfoliated single-layer and multilayer mos2 and wse2 nanosheets. *Accounts of Chemical Research*, 47(4):1067–1075, 2014. PMID: 24697842.

[29] Stanley S. Chou, Bryan Kaehr, Jaemyung Kim, Brian M. Foley, Mrinmoy De, Patrick E. Hopkins, Jiaxing Huang, C. Jeffrey Brinker, and Vinayak P. Dravid. Chemically exfoliated mos2 as near-infrared photothermal agents. *Angewandte Chemie International Edition*, 52(15):4160–4164, 2013.

[30] Sefaattin Tongay, Wen Fan, Jun Kang, Joonsuk Park, Unsal Koldemir, Joonki Suh, Deepa S. Narang, Kai Liu, Jie Ji, Jingbo Li, Robert Sinclair, and Junqiao Wu. Tuning interlayer coupling in large-area heterostructures with cvd-grown mos2 and ws2 monolayers. *Nano Letters*, 14(6):3185–3190, 2014. PMID: 24845201.

[31] Talivaldis Spalvins. Morphological and frictional behavior of sputtered mos2 films. *Thin Solid Films*, 96(1):17 – 24, 1982.

[32] Joshua V. Pondick, John M. Woods, Jie Xing, Yu Zhou, and Judy J. Cha. Stepwise sulfurization from moo3 to mos2 via chemical vapor deposition. *ACS Applied Nano Materials*, 1(10):5655–5661, 2018.

[33] S.D. Walck, J.S. Zabinski, M.S. Donley, and J.E. Bultman. Evolution of surface topography in pulsed-laser-deposited thin films of mos2. *Surface and Coatings Technology*, 62(1):412 – 416, 1993.

[34] Luigi G. Coocia, Glenn C. Tyrrell, John A. Kilner, David Waller, Richard J. Chater, and Ian W. Boyd. Pulsed laser deposition of novel materials for thin film solid oxide fuel cell applications: Ce0.9gd0.1o1.95, la0.7sr0.3cooy and la0.7sr0.3co0.2fe0.8oy. *Applied Surface Science*, 96-98:795 – 801, 1996.

[35] Changrong Xia, Fanglin Chen, and Meilin Liu. Reduced-temperature solid oxide fuel cells fabricated by screen printing. *Electrochemical and Solid-State Letters*, 4(5), may 2001.

[36] Zigui Lu, John Hardy, Jared Templeton, Jeffry Stevenson, Daniel Fisher, Naijuan Wu, and Alex Ignatiev. Performance of anode-supported solid oxide

fuel cell with thin bi-layer electrolyte by pulsed laser deposition. *Journal of Power Sources*, 210:292 – 296, 2012.

[37] Randal Informatiker. Bryant, David Richard 1955 O'Hallaron, and Manasa S. *Computer systems : a programmer's perspective*. Pearson, 2016.

[38] R. R. Schaller. Moore's law: past, present and future. *IEEE Spectrum*, 34(6):52–59, June 1997.

[39] Gordon E. Moore. Lithography and the future of Moore's law. In Marylyn Hoy Bennett, editor, *Integrated Circuit Metrology, Inspection, and Process Control IX*, volume 2439, pages 2 – 17. International Society for Optics and Photonics, SPIE, 1995.

[40] Sujay B. Desai, Surabhi R. Madhvapathy, Angada B. Sachid, Juan Pablo Llinas, Qingxiao Wang, Geun Ho Ahn, Gregory Pitner, Moon J. Kim, Jeffrey Bokor, Chenming Hu, H.-S. Philip Wong, and Ali Javey. Mos2 transistors with 1-nanometer gate lengths. *Science*, 354(6308):99–102, 2016.

[41] Amirhasan Nourbakhsh, Ahmad Zubair, Redwan N. Sajjad, Amir Tavakkoli K. G., Wei Chen, Shiang Fang, Xi Ling, Jing Kong, Mildred S. Dresselhaus, Efthimios Kaxiras, Karl K. Berggren, Dimitri Antoniadis, and Tomás Palacios. Mos2 field-effect transistor with sub-10 nm channel length. *Nano Letters*, 16(12):7798–7806, 2016.

[42] Ming-Yang Li, Sheng-Kai Su, H-S Philip Wong, and Lain-Jong Li. How 2d semiconductors could extend moore's law. *Nature*, 2019.

[43] Sheneve Z. Butler, Shawna M. Hollen, Linyou Cao, Yi Cui, Jay A. Gupta, Humberto R. Gutiérrez, Tony F. Heinz, Seung Sae Hong, Jiaxing Huang, Ariel F. Ismach, Ezekiel Johnston-Halperin, Masaru Kuno, Vladimir V. Plashnitsa, Richard D. Robinson, Rodney S. Ruoff, Sayeef Salahuddin, Jie Shan, Li Shi, Michael G. Spencer, Mauricio Terrones, Wolfgang Windl, and Joshua E. Goldberger. Progress, challenges, and opportunities in two-dimensional materials beyond graphene. *ACS Nano*, 7(4):2898–2926, 2013. PMID: 23464873.

[44] Y.-M. Lin, C. Dimitrakopoulos, K. A. Jenkins, D. B. Farmer, H.-Y. Chiu, A. Grill, and Ph. Avouris. 100-ghz transistors from wafer-scale epitaxial graphene. *Science*, 327(5966):662–662, 2010.

[45] K.I. Bolotin, K.J. Sikes, Z. Jiang, M. Klima, G. Fudenberg, J. Hone, P. Kim, and H.L. Stormer. Ultrahigh electron mobility in suspended graphene. *Solid State Communications*, 146(9):351 – 355, 2008.

[46] Goki Eda and Manish Chhowalla. Chemically derived graphene oxide: Towards large-area thin-film electronics and optoelectronics. *Advanced Materials*, 22(22):2392–2415, 2010.

[47] Zhihao Yu, Zhun-Yong Ong, Songlin Li, Jian-Bin Xu, Gang Zhang, Yong-Wei Zhang, Yi Shi, and Xinran Wang. Analyzing the carrier mobility in transition-metal dichalcogenide mos2 field-effect transistors. *Advanced Functional Materials*, 27(19):1604093, 2017.

[48] Han Liu, Adam T. Neal, and Peide D. Ye. Channel length scaling of mos2 mosfets. *ACS Nano*, 6(10):8563–8569, 2012. PMID: 22957650.

[49] H Yang, J K Zhang, C Li, D Zhao, and D P Wu. Visibility of single layer MoS2 for different dielectric layers on si substrate. *IOP Conference Series: Materials Science and Engineering*, 479:012037, Mar 2019.

[50] Nengjie Huo, Jun Kang, Zhongming Wei, Shu-Shen Li, Jingbo Li, and Su-Huai Wei. Novel and enhanced optoelectronic performances of multilayer mos2–ws2 heterostructure transistors. *Advanced Functional Materials*, 24(44):7025–7031, 2014.

[51] Andres Castellanos-Gomez, Ronald van Leeuwen, Michele Buscema, Herre S. J. van der Zant, Gary A. Steele, and Warner J. Venstra. Single-layer mos2 mechanical resonators. *Advanced Materials*, 25(46):6719–6723, 2013.

[52] W. Cao, J. Kang, D. Sarkar, W. Liu, and K. Banerjee. Performance evaluation and design considerations of 2d semiconductor based fets for sub-10 nm vlsi. In *2014 IEEE International Electron Devices Meeting*, pages 30.5.1–30.5.4, Dec 2014.

[53] Lianfu Jiang, Shengli Zhang, Sergei A. Kulinich, Xiufeng Song, Junwu Zhu, Xin Wang, and Haibo Zeng. Optimizing hybridization of 1t and 2h phases in mos2 monolayers to improve capacitances of supercapacitors. *Materials Research Letters*, 3(4):177–183, 2015.

[54] Kin Fai Mak, Changgu Lee, James Hone, Jie Shan, and Tony F. Heinz. Atomically thin MoS2: A new direct-gap semiconductor. *Physical Review Letters*, 105(13), Sep 2010.

[55] Gwan-Hyoung Lee, Young-Jun Yu, Xu Cui, Nicholas Petrone, Chul-Ho Lee, Min Sup Choi, Dae-Yeong Lee, Changgu Lee, Won Jong Yoo, Kenji Watanabe, Takashi Taniguchi, Colin Nuckolls, Philip Kim, and James Hone. Flexible and transparent mos2 field-effect transistors on hexagonal boron nitride-graphene heterostructures. *ACS Nano*, 7(9):7931–7936, 2013. PMID: 23924287.

[56] M. Donarelli, S. Prezioso, F. Perrozzi, F. Bisti, M. Nardone, L. Giancaterini, C. Cantalini, and L. Ottaviano. Response to no2 and other gases of resistive chemically exfoliated mos2-based gas sensors. *Sensors and Actuators B: Chemical*, 207:602 – 613, 2015.

[57] Woong Choi, Mi Yeon Cho, Aniruddha Konar, Jong Hak Lee, Gi-Beom Cha, Soon Cheol Hong, Sangsig Kim, Jeongyong Kim, Debdeep Jena, Jinsoo Joo, and Sunkook Kim. High-detectivity multilayer mos2 phototransistors with spectral response from ultraviolet to infrared. *Advanced Materials*, 24(43):5832–5836, 2012.

[58] Chuanqi Feng, Jun Ma, Hua Li, Rong Zeng, Zaiping Guo, and Huakun Liu. Synthesis of molybdenum disulfide (mos2) for lithium ion battery applications. *Materials Research Bulletin*, 44(9):1811 – 1815, 2009.

[59] K. S. Novoselov, D. Jiang, F. Schedin, T. J. Booth, V. V. Khotkevich, S. V. Morozov, and A. K. Geim. Two-dimensional atomic crystals. *Proceedings of the National Academy of Sciences of the United States of America*, 102(30):10451–10453, Jul 2005.

[60] Liping Ji, Juan Shi, Z. Y. Zhang, Jun Wang, Jiachi Zhang, Chunlan Tao, and Haining Cao. Theoretical prediction of high electron mobility in multilayer

MoS 2 heterostructured with MoSe 2. *Journal of Chemical Physics*, 148(1), Jan 2018.

[61] Xingqiang Liu, Renrong Liang, Guoyun Gao, Caofeng Pan, Chunsheng Jiang, Qian Xu, Jun Luo, Xuming Zou, Zhenyu Yang, Lei Liao, and Zhong Lin Wang. Mos2 negative-capacitance field-effect transistors with subthreshold swing below the physics limit. *Advanced Materials*, 30(28):1800932, 2018.

[62] Z. Dong and J. Guo. Assessment of 2-d transition metal dichalcogenide fets at sub-5-nm gate length scale. *IEEE Transactions on Electron Devices*, 64(2):622–628, Feb 2017.

[63] Keliang He, Charles Poole, Kin Fai Mak, and Jie Shan. Experimental demonstration of continuous electronic structure tuning via strain in atomically thin mos2. *Nano Letters*, 13(6):2931–2936, May 2013.

[64] S Gamble. Fabrication–microstructure–performance relationships of reversible solid oxide fuel cell electrodes–review. *Materials Science and Technology*, 27(10):1485–1497, 2011.

[65] M. Asif and T. Muneer. Energy supply, its demand and security issues for developed and emerging economies. *Renewable and Sustainable Energy Reviews*, 11(7):1388 – 1413, 2007.

[66] Nguyen Q. Minh. *Reversible Solid Oxide Fuel Cell Technology for Hydrogen/Syngas and Power Production*, chapter 16, pages 359–390. John Wiley Sons, Ltd, 2016.

[67] Tapas Kuila, Ananta Kumar Mishra, Partha Khanra, Nam Hoon Kim, and Joong Hee Lee. Recent advances in the efficient reduction of graphene oxide and its application as energy storage electrode materials. *Nanoscale Phenomena*, 5(1):52–71, Jan 2013.

[68] Cha Suk-Won Colella Whitney G. Prinz Fritz B. O'hayre, Ryan. John Wiley Sons, 2016.

[69] Jimmi Nielsen and Johan Hjelm. Impedance of sofc electrodes: A review and a comprehensive case study on the impedance of lsm:ysz cathodes. *Electrochimica Acta*, 115:31 – 45, 2014.

[70] P.-M. Geffroy, J. Fouletier, N. Richet, and T. Chartier. Rational selection of miec materials in energy production processes. *Chemical Engineering Science*, 87:408 – 433, 2013.

[71] Suman Kumar Burnwal, S. Bharadwaj, and P. Kistaiah. Review on miec cathode materials for solid oxide fuel cells. *Journal of Molecular and Engineering Materials*, 04(02):1630001, 2016.

[72] P. K. Addo, B. Molero-Sanchez, M. Chen, S. Paulson, and V. Birss. Co/co2 study of high performance la0.3sr0.7fe0.7cr0.3o3– reversible sofc electrodes. *Fuel Cells*, 15(5):689–696, 2015.

[73] André Guinier. *X-ray diffraction in crystals, imperfect crystals, and amorphous bodies*. Courier Corporation, 1994.

[74] Seizo Morita, Franz J Giessibl, Ernst Meyer, and Roland Wiesendanger. *Noncontact atomic force microscopy*, volume 3. Springer, 2015.

[75] Weilie Zhou and Zhong Lin Wang. *Scanning microscopy for nanotechnology: techniques and applications*. Springer science & business media, 2007.

[76] David Briggs. *Handbook of X-ray and ultraviolet photoelectron spectroscopy*. Heyden London, 1977.

[77] Halina Baranska, Anna Labudzinska, and Jacek Terpinski. *Laser Raman spectrometry: analytical applications*. John Wiley and Sons, New York, NY, 1987.

[78] Jon W Erickson and Steve Semancik. An economical ultrahigh vacuum four-point resistivity probe. *Journal of Vacuum Science & Technology A: Vacuum, Surfaces, and Films*, 5(1):115–117, 1987.

[79] Ronald Chwang, BJ Smith, and CR Crowell. Contact size effects on the van der pauw method for resistivity and hall coefficient measurement. *Solid-State Electronics*, 17(12):1217–1227, 1974.

[80] Gianluca Fiori and Giuseppe Iannaccone. Nanotcad vides. 2008.

[81] Yung-Chun Wu and Yi-Ruei Jhan. *3D TCAD Simulation for CMOS Nanoeletronic Devices*. Springer, 2018.

[82] Haijiao Lu, Jingkang Wang, Hongxun Hao, and Ting Wang. Magnetically separable mos2/fe3o4/nzvi nanocomposites for the treatment of wastewater containing cr (vi) and 4-chlorophenol. *Nanomaterials*, 7(10):303, 2017.

[83] Lei Jiao, Yuehui Wang, Yusong Zhi, Wei Cui, Zhengwei Chen, Xiao Zhang, Wenjing Jie, and Zhenping Wu. Fabrication and characterization of two-dimensional layered mos2 thin films by pulsed laser deposition. *Advances in Condensed Matter Physics*, 2018, 2018.

[84] Arun Barvat, Nisha Prakash, Gaurav Kumar, Dilip K Singh, Anjana Dogra, Suraj P Khanna, and Prabir Pal. Electronic structure of the pld grown mixed phase mos2/gan interface and its thermal annealing effect. *Current Applied Physics*, 18(2):170–177, 2018.

[85] Arun Barvat, Nisha Prakash, Dilip K Singh, Anjana Dogra, Suraj P Khanna, Sandeep Singh, and Prabir Pal. Mixed phase compositions of mos2 ultra thin film grown by pulsed laser deposition. *Materials Today: Proceedings*, 5(1):2241–2245, 2018.

[86] Gene Siegel, Y. P. Venkata Subbaiah, Megan C. Prestgard, and Ashutosh Tiwari. Growth of centimeter-scale atomically thin mos2 films by pulsed laser deposition. *APL Materials*, 3(5):056103, 2015.

[87] Hong Li, Qing Zhang, Chin Chong Ray Yap, Beng Kang Tay, Teo Hang Tong Edwin, Aurelien Olivier, and Dominique Baillargeat. From bulk to monolayer mos2: Evolution of raman scattering. *Advanced Functional Materials*, 22(7):1385–1390, 2012.

[88] Kin Fai Mak, Changgu Lee, James Hone, Jie Shan, and Tony F. Heinz. Atomically thinmos2: A new direct-gap semiconductor. *Physical Review Letters*, 105(13), Sep 2010.

[89] Dumitru Dumcenco, Dmitry Ovchinnikov, Kolyo Marinov, Predrag Lazić, Marco Gibertini, Nicola Marzari, Oriol Lopez Sanchez, Yen-Cheng Kung, Daria Krasnozhon, Ming-Wei Chen, Simone Bertolazzi, Philippe Gillet, Anna Fontcuberta i Morral, Aleksandra Radenovic, and Andras Kis. Large-area epitaxial monolayer mos2. *ACS Nano*, 9(4):4611–4620, 2015. PMID: 25843548.

[90] L. Britnell, R. M. Ribeiro, A. Eckmann, R. Jalil, B. D. Belle, A. Mishchenko, Y.-J. Kim, R. V. Gorbachev, T. Georgiou, S. V. Morozov, A. N. Grigorenko, A. K. Geim, C. Casiraghi, A. H. Castro Neto, and K. S. Novoselov. Strong light-matter interactions in heterostructures of atomically thin films. *Science*, 340(6138):1311–1314, 2013.

[91] B. Radisavljevic, A. Radenovic, J. Brivio, V. Giacometti, and A. Kis. Single-layer MoS2 transistors. *Nature Nanotechnology*, 6(3):147–150, 2011.

[92] Ming-Wei Lin, Ivan I Kravchenko, Jason Fowlkes, Xufan Li, Alexander A Puretzky, Christopher M Rouleau, David B Geohegan, and Kai Xiao. Thickness-dependent charge transport in few-layer mos2 field-effect transistors. *Nanotechnology*, 27(16):165203, 2016.

[93] Song-Lin Li, Katsunori Wakabayashi, Yong Xu, Shu Nakaharai, Katsuyoshi Komatsu, Wen-Wu Li, Yen-Fu Lin, Alex Aparecido-Ferreira, and Kazuhito Tsukagoshi. Thickness-dependent interfacial coulomb scattering in atomically thin field-effect transistors. *Nano Letters*, 13(8):3546–3552, 2013. PMID: 23862641.

[94] Ming-Wei Lin, Ivan I Kravchenko, Jason Fowlkes, Xufan Li, Alexander A Puretzky, Christopher M Rouleau, David B Geohegan, and Kai Xiao. Thickness-dependent charge transport in few-layer MoS2field-effect transistors. *Nanotechnology*, 27(16):165203, mar 2016.

[95] Florian Werner. Hall measurements on low-mobility thin films. *Journal of Applied Physics*, 122(13):135306, 2017.

[96] Josef Hölzl and Franz K Schulte. Work function of metals. In *Solid surface physics*, pages 1–150. Springer, 1979.

[97] Thang Phan Nguyen, Quyet Van Le, Kyoung Soon Choi, Jeong Hyeon Oh, Yu Geun Kim, Sung Min Lee, Suk Tai Chang, Yoon-Ho Cho, Seongcheol Choi, Tae-Yoon Kim, et al. Mos2 nanosheets exfoliated by sonication and their application in organic photovoltaic cells. *Science of Advanced Materials*, 7(4):700–705, 2015.

[98] Jong Hun Kim, Jinhwan Lee, Jae Hyeon Kim, CC Hwang, Changgu Lee, and Jeong Young Park. Work function variation of mos2 atomic layers grown

with chemical vapor deposition: The effects of thickness and the adsorption of water/oxygen molecules. *Applied Physics Letters*, 106(25):251606, 2015.

[99] Zefei Wu, Benjamin T Zhou, Xiangbin Cai, Patrick Cheung, Gui-Bin Liu, Meizhen Huang, Jiangxiazi Lin, Tianyi Han, Liheng An, Yuanwei Wang, et al. Intrinsic valley hall transport in atomically thin mos 2. *Nature communications*, 10(1):611, 2019.

[100] Saptarshi Das and Joerg Appenzeller. Screening and interlayer coupling in multilayer mos2. *physica status solidi (RRL) – Rapid Research Letters*, 7(4):268–273, 2013.

[101] Junsen Gao, Dipanjan Nandi, and Manisha Gupta. Density functional theory—projected local density of states—based estimation of schottky barrier for monolayer mos2. *Journal of Applied Physics*, 124(1):014502, 2018.

[102] Ji Heon Kim, Tae Ho Kim, Hyunjea Lee, Young Ran Park, Woong Choi, and Cheol Jin Lee. Thickness-dependent electron mobility of single and few-layer MoS2 thin-film transistors. *AIP Advances*, 6(6), Jun 2016.

[103] Andrea Splendiani, Liang Sun, Yuanbo Zhang, Tianshu Li, Jonghwan Kim, Chi Yung Chim, Giulia Galli, and Feng Wang. Emerging photoluminescence in monolayer MoS2. *Nano Letters*, 10(4):1271–1275, Apr 2010.

[104] Loïc Marchetti, Frédéric Miserque, Stéphane Perrin, and Michèle Pijolat. Xps study of ni-base alloys oxide films formed in primary conditions of pressurized water reactor. *Surface and Interface Analysis*, 47(5):632–642, 2015.

[105] Michael D Roach, John T Wolan, Doug E Parsell, and Joel D Bumgardner. Use of x-ray photoelectron spectroscopy and cyclic polarization to evaluate the corrosion behavior of six nickel-chromium alloys before and after porcelain-fused-to-metal firing. *The Journal of prosthetic dentistry*, 84(6):623–634, 2000.

[106] Federica M Piras, Antonella Rossi, and Nicholas D Spencer. Combined in situ (atr ft-ir) and ex situ (xps) study of the zndtp-iron surface interaction. *Tribology Letters*, 15(3):181–191, 2003.

[107] NS McIntyre and DG Zetaruk. X-ray photoelectron spectroscopic studies of iron oxides. *Analytical Chemistry*, 49(11):1521–1529, 1977.

[108] AP Grosvenor, BA Kobe, and NS McIntyre. Examination of the oxidation of iron by oxygen using x-ray photoelectron spectroscopy and quasestm. *Surface science*, 565(2-3):151–162, 2004.

[109] VV Kaichev, VI Bukhtiyarov, M Hävecker, A Knop-Gercke, RW Mayer, and R Schlögl. The nature of electrophilic and nucleophilic oxygen adsorbed on silver. *Kinetics and catalysis*, 44(3):432–440, 2003.

[110] WooChul Jung and Harry L Tuller. Investigation of surface sr segregation in model thin film solid oxide fuel cell perovskite electrodes. *Energy & Environmental Science*, 5(1):5370–5378, 2012.

Appendix A

A.1 Naming scheme of MoS_2 samples grown

The naming scheme for the samples of MoS_2 followed the convention: "No.of Layers-Temperature of growth-Growth ambience - Substrate". An example of this would be 5L800C-0.5-SiO_2/Si. Here, The number of layers is 5 monolayers, and therefore designated as 5L, with the number of monolayers of MoS_2 in the thin film set by the number followed by "L". The growth temperature is 800^0C, therefore, designated as 800C, with the temperature denoted by the temperature in Celcius followed by "C". The growth ambience is 0.5 mT of Argon, which has been designated as 0.5, with the number denoting the gas pressure in mT of Ar. If the number is replaced by "V", it indicates growth in vacuum ambience. The substrate is SiO_2/Si, and based on whether SiO_2/Si, Si, Al_2O_3 or Quartz, the sample name has been suitably denoted.

A.2 Naming scheme of LMFCr samples grown

For LCFCr, the naming scheme involved the convention: Growth temperature-anneal period. For example, sample 700-U indicated growth temperature of 700^0C with no post growth anneal. The different temperatures were 25, 250 and 700 for growths at 25^0C. 250^0C and 700^0C respectively. Post growth anneal conditions were U, 30mA and 2hA depending on no anneal, 30 min post growth anneal at 700^0C and 2h post growth anneal at 700^0C .